Enhancement of the Response of Concrete at High Strain Rates

Ph.D. Thesis

By

Anshul Kaushik

DEPARTMENT OF CIVIL ENGINEERING

INDIAN INSTITUTE OF TECHNOLOGY INDORE

JUNE 2023

Enhancement of the Response of Concrete at High Strain Rates

A THESIS

Submitted in partial fulfillment of the requirements for the award of the degree of

DOCTOR OF PHILOSOPHY

by

Anshul Kaushik

DEPARTMENT OF CIVIL ENGINEERING

INDIAN INSTITUTE OF TECHNOLOGY INDORE

JUNE 2023

INDIAN INSTITUTE OF TECHNOLOGY INDORE

CANDIDATE'S DECLARATION

I hereby certify that the work which is being presented in the thesis entitled **ENHANCEMENT OF THE RESPONSE OF CONCRETE AT HIGH STRAIN RATES** in the partial fulfillment of the requirements for the award of the degree of **DOCTOR OF PHILOSOPHY** and submitted in the **DEPARTMENT OF CIVIL ENGINEERING, Indian Institute of Technology Indore**, is an authentic record of my own work carried out during the time period from July, 2019 to June, 2023 under the supervision of Dr. Abhishek Rajput, Assistant Professor, Department of Civil Engineering, Indian Institute of Technology Indore and Dr. Guru Prakash, Assistant Professor, Department of Civil Engineering, Indian Institute of Technology Indore.

The matter presented in this thesis has not been submitted by me for the award of any other degree of this or any other institute.

23/06/23

Signature of the student with date
(Anshul Kaushik)

This is to certify that the above statement made by the candidate is correct to the best of my knowledge.

Guru Prakash

22.06.2023
Signature of Thesis Supervisor (1)
Dr. Abhishek Rajput

21 June 2023
Signature of Thesis Supervisor (2)
Dr. Guru Prakash

Anshul Kaushik has successfully given his Ph.D. Oral Examination held on

Signature of Chairperson (OEB)
Date:

Signature of External Examiner
Date:

Signature(s) of Thesis Supervisor(s)
Date:

Signature of PSPC Member #1
Date:

Signature of PSPC Member #2
Date:

Signature of Convener, DPGC
Date:

Signature of Head of Discipline

Date:

ACKNOWLEDGEMENTS

Firstly, I would like to bow down to '**Lord Shiva**' for blessing me with this opportunity and strength to carryout this endeavour.

I would like to express my sincere gratitude to my thesis supervisors **Dr. Abhishek Rajput**, Assistant Professor, Department of Civil Engineering, Indian Institute of Technology Indore, and **Dr. Guru Prakash**, Assistant Professor, Department of Civil Engineering, Indian Institute of Technology Indore, for their constant motivation, dynamic support, and valuable guidance throughout the research tenure. Their enthusiastic nature, elaborate discussions, and research directions helped me perform my research efficiently.

I am very thankful to **Prof. Manish Kumar Goyal**, and **Dr. Saikat Sarkar** for their valuable inputs during Comprehensive Evaluation Research Progress (CERP) seminars as PSPC members. Their comments helped me to improve and excel in my research work.

I am thankful to my seniors **Dr. Akshay Thakare,** and **Dr. Saket Dubey** for providing their valuable suggestions on technical issues. I would also like to thank my colleagues **Gyanesh Patnaik, Revanth Dugalam, Venkatesh Varma,** and **Mukul Saxena** for their cooperation and constant support.

I am thankful to the entire technical and management staff of the Department of Civil Engineering, including **Mr. Ajay Malviya, Mr. Amit Jadhav,** and **Mrs. Rinki Kukreja** for their assistance during my research work.

Also, I would like to thank my mother, **Smt. Ranjana Kaushik** and father **Dr. Ajay Kumar Kaushik** for their unconditional love and support. I am thankful to my brother **Mr. Ankur Kaushik** for his constant support. Finally, I am thankful to my teachers and friends who motivated, and supported me at various stages.

ABSTRACT

Concrete is one of the most widely used materials in the construction of civil and protective structures. In the present era, these structures might be exposed to extreme loading events during their lifespan. Distinctive examples in various areas range from: aircraft landing on runways, rockfall protection structures subjected to impact of falling rocks in mountainous regions, vehicular collision with transportation structures. Other examples include: industrial buildings subjected to accidental drop of heavy loads, offshore structures subjected to ship or ice impact, civil structures subjected to projectile impact or blasting events. Although, concrete is capable of withstanding quasi-static loading conditions, its performance under extreme loading is debatable due to its heterogeneous and brittle nature, as well as low tensile strength. Therefore, it has become important to explore for new techniques in order to improve the safety and response of concrete under such loading events. The focus of this research is to thoroughly investigate and analyze new methods and material configurations in order to advance towards impact resistant concrete structures.

In this study, the response of concrete under low velocity impact is examined by conducting a comprehensive parametric investigation. The influence of several parameters is determined, and the obtained results have been used to recommend a desirable set of values of each parameter which could be useful for enhancing the response of concrete under low velocity impact. The numerical investigation results show that the recommended set of parameters have a potential to marginally improve the low velocity impact response and energy absorption capacity of concrete. Further, with the aim of attaining an enhanced impact resistance, the influence of crumb rubber as partial sand replacement on the low velocity impact response of concrete is studied by conducting detailed experimental, numerical, and analytical investigations. It is observed that the use of crumb rubber enhances the ductility and energy absorption capacity of concrete. Also, the obtained results have been used to propose simple design guidelines which could be utilized for selecting optimum rubber content in concrete.

In addition, the recent major catastrophes associated with terrorist attacks include bombing of civil structures. Among the different type of structures, the subsurface reinforced concrete (RC) tunnels have become the most preferred targets for terrorist attacks. Considering the strategic importance and susceptibility of tunnels in case of internal explosion, their blast mitigating design has become very critical. Hence, in the present study, the effectiveness of glass fiber reinforced polymer (GFRP) as a protective layer over typical subsurface RC tunnels has been investigated under internal explosion. The analysis is done using explicit 3D-Finite Element (FE) method. It is observed that the application of GFRP layer reduces the displacement and stress values at key points (crown of tunnel and top soil surface).

Further, while analyzing the blast response, it was found that the use of numerical techniques is a complicated task with high computational expenses. Also, it is not feasible to conduct sensitivity analysis, and parametric studies using numerical techniques. Thus, there is a need for a predictive methodology for analyzing the blast response of subsurface RC tunnels. In this study, artificial intelligence (AI) models have been explored by utilizing several input parameters. The performance of these models is evaluated using several assessment metrics. Results show that the prediction models are stable and have high R^2 values and low root mean square error (RMSE) and mean absolute error (MAE) values. Thus, the prediction models could be utilized for quick damage assessment as well as blast resistant design of subsurface RC tunnels, and prove to be a good competitor to the existing numerical methods.

Keywords: Low velocity impact, Cement concrete, Impact energy absorption, Crumb rubber, Finite element analysis, Impact ductility, Blast loading, Subsurface tunnel, Protective layer, Damage prediction, Artificial intelligence.

LIST OF PUBLICATIONS

Journal publications from Ph.D. work (Published)

- **Kaushik, A.**, Patnaik, G., Rajput, A., & Prakash, G. (2022). Nonlinear behaviour of concrete under low-velocity impact by using a damaged plasticity model. ***Iranian Journal of Science and Technology, Transactions of Civil Engineering***, ***Springer,*** 46(5), 3655-3677. 10.1007/s40996-021-00808-3. **(Impact Factor - 1.461)**
- **Kaushik, A.**, Prakash, G., & Rajput, A. (2022). Influence of crumb rubber on the response of concrete beams against low velocity impact. ***Construction and Building Materials, Elsevier,*** 347, 128614. 10.1016/j.conbuildmat.2022.128614. **(Impact Factor – 7.693)**
- Rajput, A., **Kaushik, A.**, Iqbal, M. A., & Gupta, N. K. (2023). Non-linear FE investigation of subsurface tunnel with gfrp protection against internal blast. ***International Journal of Impact Engineering, Elsevier,*** 172, 104423. 10.1016/j.ijimpeng.2022.104423. **(*Impact Factor* – 4.592)**

Journal papers in communication

- **Kaushik, A.**, Patnaik, G., Singh, M. J., Rajput, A., Prakash, G., & Borana L. (2023). Prediction of Peak Displacement of Underground RC Tunnels subjected to Internal Explosion using Artificial Intelligence. ***Structural Engineering and Mechanics, Techno-press.*** **(ImpactFactor – 2.998)**

Journal papers under preparation

- Influence of different GFRP thicknesses as a protective covering over subsurface RC tunnels.

Conferences

- **Kaushik, A.**, Patnaik, G., Rajput, A., & Prakash, G. (2021). A parametric numerical investigation for enhancing the impact resistance of concrete. Fib Symposium, 2021-June 2195-2206

- **Kaushik, A.**, Patnaik, G., Rajput, A., Prakash, G. (2022). 3D-FE Analysis of RC Tunnel with GFRP Shielding Under Internal Blast Loading. In: Marano, G.C., Ray Chaudhuri, S., Unni Kartha, G., Kavitha, P.E., Prasad, R., Achison, R.J. (eds) Proceedings of SECON'21. SECON 2021. Lecture Notes in Civil Engineering, vol 171. Springer, Cham. https://doi.org/10.1007/978-3-030-80312-4_14

- **Kaushik, A.**, Patnaik, G., Rajput, A., & Prakash, G., Borana, L. (2021). Quantification of Construction & Demolition Waste & its Future Application in Indian Scenario. International Conference on Ecosystem Restoration for Resilience and Sustainability: Living with nature.

- **Kaushik, A.**, Patnaik, G., Rajput, A., & Prakash, G., Numerical Analysis of Underground Tunnel System with GFRP Shield against Internal Explosion (2022). IMPLAST 2022**.** Springer Proceedings in Materials (SPM, volume 34).

TABLE OF CONTENTS

LIST OF FIGURES

LIST OF TABLES

NOMENCLATURE

σ_{c0}	Initial yield stress
σ_{cu}	Ultimate stress
σ_{t0}	Failure stress in uniaxial tension
$\tilde{\varepsilon}_c^{pl}$	Compressive equivalent plastic strains
$\tilde{\varepsilon}_t^{pl}$	Tensile equivalent plastic strains
$\tilde{\varepsilon}_c^{in}$	Compressive inelastic plastic strain
$\tilde{\varepsilon}_t^{in}$	Tensile inelastic plastic strain
ε_c	Total compressive strain
σ_t	Total tensile strain
d	Damage variable
$\bar{p}$	Effective hydrostatic pressure
$\bar{q}$	Effective Mises stress
$\hat{\bar{\sigma}}_{max}$	Maximal effective principal stress
σ_{bo}	Initial biaxial yield stresses in compression
σ_{co}	Uniaxial yield stresses in compression
K_c	Shape parameter
$\dot{\varepsilon}_{pl}$	Plastic strain rate
G	Potential function
ψ	Dilation angle
ε	Eccentricity parameter
f_{cd}	Compressive strength at strain rate $\dot{\varepsilon_c}$
E_{cd}	Compressive modulus of elasticity at strain rate $\dot{\varepsilon_c}$
f_c	Compressive strength at reference strain rate
E_c	Compressive modulus of elasticity at reference strain rate
f_{td}	Tensile strength at strain rate $\dot{\varepsilon_t}$
E_{td}	Tensile modulus of elasticity at strain rate $\dot{\varepsilon_t}$
f_t	Tensile strength at reference strain rate
E_t	Tensile modulus of elasticity at reference strain rate
$\bar{P}(t)$	Total pressure due to explosion

$P_{incident}(t)$	Pressure due to incident wave
$P_{reflect}(t)$	Pressure due to reflected wave
θ	Angle of the line normal to the loading surface with respect to the line connecting it to the point of explosion
G_f	Fracture energy
ρ	Density
f_c'	Unconfined compressive strength
ν	Poisson’s ratio
μ	Viscosity parameter
w/c	Water cement ratio
v_o	Initial velocity
v_t	Final velocity
h	Drop height
g	Acceleration due to gravity
α	Ratio of actual impact velocity to the free fall velocity
S	Impulse
M_h	Mass of drop weight
E_{abs}	Energy absorbed/dissipated by the concrete beam
KE_{beam}	Kinetic energy of beam
P_{static}	Equivalent static load value
u	Displacement
$Par.$	Parabolic
$Sin.$	Sinusoidal
T	Explosive charge
f_{ck}	Characteristic compressive strength
t_t	Thickness of RC tunnel
f_y	Yield tensile strength of steel

ACRONYMS

RC	Reinforced Concrete
GFRP	Glass fiber reinforced polymer
FE	Finite Element
AI	Artificial Intelligence
RMSE	Root Mean Square Error
MAE	Mean Absolute Error
ANN	Artificial Neural Networks
SVM	Support Vector Machines
RF	Random Forest
CDP	Concrete Damaged Plasticity
TNT	Trinitrotoluene
PEEQT	Equivalent Plastic Strain in Tension
FRP	Fiber Reinforced Polymer
CFRP	Carbon Fiber Reinforced Polymer
HJC	Holmquist-Johnson-Cook
JH-2	Johnson-Holmquist-2
SDOF	Single Degree of Freedom
MDOF	Multiple Degree of Freedom
RCC	Reinforced Cement Concrete
CEL	Coupled Euler Lagrange
ALE	Arbitrary Lagrangian Eulerian
CONWEP	Conventional Weapons
EPS	Expandable Polystyrene
SFRC	Steel Fiber Reinforced Concrete
ML	Machine Learning
PDE	Partial Differential Equations
RMSE	Root Mean Square Error
R^2	Coefficient of determination
MAPE	Mean absolute percentage error
VAF	Variability account for

LVDT	Linear Variable Differential Transformer
RR	Reinforcement Ratio
DAMAGET	Tensile Damage parameter
OPC	Ordinary Portland Cement
SG	Strain Gauge
SEM	Scanning Electron Microscopy
CSH	Calcium-Silicate-Hydrate
CH	Calcium Hydroxide
E	Ettringite
JWL	Jones-Wilkins-Lee
NSE	Nash-Sutcliffe Efficiency

Chapter-1

Introduction

1.1 Background and Motivation

Concrete is the second most utilized material throughout the globe following water, and is the most widely used construction material. It is used in the construction of civil as well as protective structures which might be exposed to extreme loading conditions due to intentional or accidental events during their lifespan [1–5]. Distinctive examples in various areas range from: aircraft landing on runways, rockfall protection structures subjected to impact of falling rocks in mountainous regions, vehicular collision with transportation structures. Other examples include: industrial buildings subjected to accidental drop of heavy loads, offshore structures subjected to ship or ice impact, civil structures subjected to projectile impact or blasting events (See Figure 1.1). Although, concrete can sustain quasi-static loading conditions, its performance under extreme loading is debatable due to several reasons.

When a concrete structural element is subjected to extreme events such as impact or blast loading conditions, excessive stresses are transferred, and compression waves are generated on the impacted side of the target. These compression waves traverse towards the distal side and get reflected as tension waves in an extremely short duration of time. Thus, tensile stresses are a direct and predominant consequence of impact or blast loading [6]. Since, the tensile and flexural strength characteristics of concrete are considerably low as compared to that of its compressive strength, an extreme event may affect the overall integrity of structure. Also, concrete has poor energy absorption capability due to its heterogeneous and brittle nature. This significantly affects the ability of concrete to safeguard its integrity under extreme loads resulting in sudden failure and inevitable casualties. Thus, the contemporary strive for enhanced performance under extreme events explains the demand for development of novel techniques and methodologies that can assure the safety of concrete structures under such loading conditions.

(a)

(b)

(c)

(d)

(e)

(f)

Figure 1.1 Various cases of structural damage due to extreme loading conditions (a) aircraft landing on runway (b) rockfall protection structure subjected to falling rocks (c) (d) transportation structures including bridge columns subjected to accidental impact of vehicle (e) civilian structure subjected to projectile impact (f) underground tunnel subjected to internal explosion [7–11]

Previously, several techniques have been explored to improve the response of concrete under impact loading. Most of these studies were mainly focused on the use of strengthening techniques such as addition of steel fibers [12, 13], polypropylene fibers [14, 15], carbon fibers [16], and rubber fibers [17, 18]. The external bonding of steel, and fiber reinforced polymer (FRP) materials have also been found to enhance the impact response of concrete structural elements [19, 20]. Apart from this, researchers have also investigated the use of reinforcement and pre-stressing in concrete for enhanced impact resistance [21–23]. Out of the different methods, the addition of fibers has been widely adapted due to their easy incorporation in the concrete mix. Among the different types of fibers, the use of crumb rubber in concrete imparts several environmental benefits. It reduces the demand for mineral aggregates, and offers an alternative method of disposing off worn-out tires [24]. Hence, crumb rubber may be considered a valuable addition to concrete. Additionally, in order to enhance the performance of concrete under impact loading, a comprehensive understanding related to the influence of several parameters is necessary.

In the past few decades, significant attention has been given towards issues related to dynamic loading. The impact and earthquake loading related issues are relatively old, the dilemmas related to blast loading are new. Due to the recent accidental and intentional episodes across the globe, the studies related to the response of structural components against blast loading have drawn the attention of researchers. Conventionally, the structural components are not designed for resisting blasting events. However, in the recent times, engineers are progressively looking for blast resistant design of critical structures.
Several terrorist events such as the bombings of Chennai Airport (1984), Brahmaputra train (1996), US Embassies, World Trade Center (1993), and subways of different cities such as London (2005), Moscow (2010 & 2004), Belgium (2016), and Saint Petersburg (2017) have raised the concern for the safety of structures. Among the different types of structures, the subsurface RC tunnels have become the easiest and most preferred targets for terrorist attacks. Due to huge patronage and hindered boundaries in a confined space, an explosion inside a

subsurface tunnel is more detrimental as compared to that at ground surface. Also, it may result in degradation of tunnel structure and contribute towards several types of geotechnical hazards such as rock fault, liquefaction, and reduced soil shear strength resulting in possible loss of human lives and huge infrastructural damage.

In order to reduce the potential damage of tunnels in case of an internal explosion, some studies have explored few mitigation techniques involving the use of a sacrificial cladding layer. Some examples include: mild steel cladding [25], aluminium foam panel [26], aluminium alloy or annealed mild steel sandwich panels [27]. Additionally, the external bonding of fiber reinforced polymer (FRP) materials has been verified to be a successful strengthening technique for improving the strength, stiffness, impact resistance, and ductility, of various structural elements [19, 28]. Also, the use of carbon fiber reinforced polymer (CFRP) as protective shield has been found to improve the performance of tunnel against blast loading [29]. Although, among the different FRP materials, glass fiber reinforced polymer (GFRP) is the most economical [30], with low conductivity and high thermal insulation properties, thus making it suitable for strengthening the structural components against blast.

The full-scale experimental studies related to blast loading on subsurface RC tunnels are not feasible from socio-economic considerations. Also, the analytical methods developed for the analysis of blast response till date are based on simplified assumptions, resulting in reduced accuracy. With the recent advancement in computational techniques and evolution of new material constitutive models, numerical methods such as finite element (FE) offer a good opportunity to perform dynamic analysis of complex problems. Due to this, the blast analysis of subsurface RC tunnels has been well studied using numerical techniques. However, the numerical techniques offer various challenges such as: the consideration of effects of post peak dynamic behavior, mesh dependency, contact interaction between two surfaces, immense modeling work, and computational expenses. In short, the numerical blast analysis of RC tunnels is a complicated task with high computational expenses. Also, it is not possible to conduct sensitivity analysis, and parametric studies if wide range of input variables are present. Thus, there is a need to establish a predictive methodology with the accuracy of numerical methods and low computational expenses of semi-empirical methods which could be utilized for detailed blast analysis of subsurface RC tunnels.

Artificial Intelligence (AI) is suitable for accomplishing the objective discussed above. Fully trained AI models are very useful for rendering and establishing highly complex problems with numerous parameters and have the capability to give new predictions and perform a detailed analysis. Nowadays, AI is being widely utilized in civil and infrastructural engineering [31–33], as it demands lesser effort, easier implementation, and low computational expenses from the user. Hence, it may be considered a good contender for predicting the response of subsurface RC tunnels under internal explosion.

1.2 Research Objectives

Based on the above discussion, this thesis involves the following objectives:

- To carry out a comprehensive parametric investigation for identifying the desirable set of values of each concrete parameter which could be used to improve its response under low velocity impact.
- To investigate the influence of crumb rubber on the low velocity impact response of concrete by performing detailed experimental, numerical, and analytical investigations.
- To investigate the effectiveness of GFRP as a protective covering over underground RC tunnels against internal

explosion.

- To explore AI models for predicting the blast induced peak displacement at the crown of subsurface RC tunnels and compare its performance with the existing numerical techniques.

1.3 Organization of the Thesis

This thesis is organized into seven chapters which are as follows:

- Chapter 1: Presents the significance of the study on the response of concrete against extreme loading events such as low velocity impact and explosions. The research background, objectives, and thesis organization are also discussed.
- Chapter 2: A review of the previous studies and research outcomes related to the behavior of concrete against extreme loading events. Different methodologies used for analyzing the response of concrete under such loading conditions are discussed concisely along with their applicability and limitations.
- Chapter 3: Discuss the low velocity impact behavior of concrete, emphasizing the application of CDP model for analyzing the response of concrete. The effect of various parameters is studied, and the desirable set of values of each parameter for attaining an enhancement in the impact resistance are determined.
- Chapter 4: Investigated the low velocity impact behavior of concrete with crumb rubber as partial replacement of sand by performing detailed experimental, numerical, and analytical techniques. The correlation between macroscopic and microscopic attributes of rubberized concrete are also established and simple design guidelines are presented for the use of crumb rubber in concrete.
- Chapter 5: The response of subsurface RC tunnels utilized in underground metro system is investigated against internal explosion using numerical techniques. The influence of different governing parameters is studied and the effectiveness of GFRP as

protective shielding material over underground RC tunnel is explored.

- Chapter 6: Different AI models such as artificial neural networks (ANN), support vector machines (SVM), and random forests (RF) are utilized for predicting the blast induced peak displacement of underground RC tunnels. The performance of each model is evaluated using several statistical parameters, and the most efficient model is presented for the damage assessment of RC tunnels.
- Chapter 7: This chapter presents and draws the conclusion of the overall study.

Chapter-2

Literature review

The design of concrete structures is typically carried out by considering the ultimate limit state criteria under static loading conditions which includes dead loads and live loads [34]. While, the dead loads on structures (such as: self-weight, floor finish etc.) are usually static in nature, the intensity of live loads (such as crane load, vehicular traffic load, pedestrian load etc.) may vary immensely with time. In most of the cases where the rate of loading is comparatively small, the live loads may be postulated to be quasi-static since they result in development of low strain rates (a typical range of strain rates for various loading scenarios is shown in Figure 2.1). However, in case of an extreme loading event (including impact or blast loading conditions) such postulations could be substandard and may be detrimental for the structure. Thus, the need for impact resistant design of concrete structures is a comprehensive domain. Till date, researchers have explored several techniques in order to improve the response of concrete against extreme loading conditions. This chapter provides a brief discussion and a comprehensive review related to the previous studies performed in this area. This chapter also presents a detailed review on the different methodologies other than experimental techniques, which could be used to model the response of concrete under extreme loading conditions. The different phenomenon such as strain rate effects, salient attributes of explicit analysis, and materials constitutive models available in ABAQUS/Explicit [35] have also been discussed.

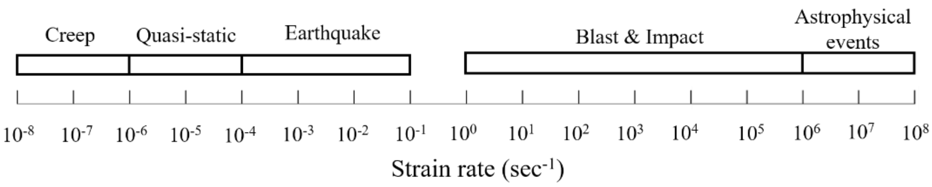

Figure 2.1 Range of strain rates for various loading conditions

2.1 Low velocity impact loading on concrete structures

The low velocity impact loading (impact velocity < 10 m/s) may be considered a typical accidental loading scenario for civil engineering structures. Common cases include: vehicular accidents, aircraft accidents, offshore accidents, accidents at construction site resulting in falling/swinging objects, human activities, rockfall in mountainous areas, etc. [1]. Although, concrete can sustain normal (static) loading conditions successfully, it is not capable of withstanding extreme loading conditions developed in case of accidental events due to brittle nature and low energy absorption capability. Due to this, several investigations have been performed in order to improve the response of concrete under such loading conditions [3, 12–18, 21, 23]. Most of these studies were mainly focused on the use of internal strengthening techniques involving the addition of different types of fibers (such as steel, carbon, polypropylene, rubber, etc.) in the concrete mix.

Siddique et al. [36] used fine bone china ceramic aggregate as fine aggregate replacement in different proportions and found that an increase in impact resistance, compressive strength, split tensile strength, and flexural strength is achieved. Al-Tayeb et al. [37], [38] used crumb rubber as partial sand replacement and observed an enhancement in the impact resistance with reduced compressive strength and tensile strength. Pham et al. [39] developed rubberized concrete beams and observed a reduction in the compressive strength with an increase in impact energy due to increase in rubber content. Saxena et al. [40] utilized shredded Poly Ethylene Terephthalate (PET) bottles as fine and coarse aggregates and observed an improvement in the ductility and energy absorption with a reduction in the compressive strength. Foti and Paparella [41] used PET layers as a replacement of steel bars and concluded that its use is beneficial for airport taxiway pavements as it is less corrosive and economical as compared to carbon of glass mesh. Al-Tayeb et al. [42] used plastic waste as partial replacement of sand and observed an improvement in the impact resistance with poor compressive strength and workability of concrete. Mohammadhosseini et al. [43, 44] used waste polypropylene carpet fibers and waste metalized plastic films in concrete and observed an improvement in the impact resistance, tensile strength, and energy absorption characteristics with a reduction in the compressive strength. Several studies used steel fibers in concrete and observed a marginal improvement in the ductility and energy absorption capacity of concrete [45–48]. Naraganti et al. [15] used sisal fibers, polypropylene, and steel fibers in concrete in different percentages and observed an increase in compressive strength and impact resistance. Similar studies were also conducted by Mo et al. [49], and Yoo et al. [50]. Aliabdo et al. [12] compared the performance of steel and polypropylene fibers and found that steel fibers are superior as compared to polypropylene fibers in terms of improved impact resistance and compressive strength characteristics. Apart from this, several studies have also investigated the influence of reinforcement and pre-stressing on the impact response of concrete [3, 21, 23]. Additionally, the external strengthening techniques involving the external bonding of high tensile strength materials such as FRP and steel have also been studied [51–54].

Out of the above discussed techniques, the use of fibers in concrete has been widely adopted due to several advantages: (1) they can be easily incorporated in the concrete mix, (2) they excellently upgrade the impact resistance properties, (3) most of the fibers are economical. Among the different types of fibers, the use of crumb rubber in concrete provides several environmental benefits [55]. It reduces the demand for mineral aggregates, and offers a method for disposing off waste tires [24]. Also, due to its elastic nature, crumb rubber enhances the ductility and energy absorption capacity of concrete. Hence, crumb rubber may be considered a valuable addition to concrete in order to enhance its impact resistance properties.

Till date, many studies have explored the possibilities and advantages of using crumb rubber in concrete [24, 38, 56–64]. Additionally, its suitability for use in concrete crash barriers and railway sleepers has been proven as well [65, 66]. Khaloo et al. [24] examined the effects of different types and proportions of rubber particles as alternatives to aggregates and concluded that the rubber content in concrete reduced brittleness and compressive strength. Similarly, Sukontasukkul and Chaikaew [56] observed that the inclusion of crumb rubber in concrete enhanced the flexibility, energy absorption capacity, and toughness while causing a reduction in the compressive and flexural strength. Xue and Shinozuka [61] reported an increased energy dissipation capacity and reduced modulus of elasticity due to use of crumb rubber as a coarse aggregate replacement. Li et al. [62] performed a detailed investigation on the compressive stress-strain response of concrete employing crumb rubber as sand replacement (6 - 18 % by volume). Similarly, Abdelmonem et al. [67] investigated the response of high strength concrete with crumb rubber, and observed that rubberized concrete displayed good workability with a marginal reduction in the density.

The low velocity impact response of rubberized concrete has been investigated by a few studies. Some of them utilized simplified test setups, which did not reflect the detailed response. For example, Taha et al. [57] used chipped and crumb rubber as aggregate replacement in different volume proportions and performed impact tests using a drop hammer rig. The beam specimens were impacted by 10 kg weight from 60 mm elevation and the number of blows for first crack and failure were recorded. It was noted that the employment of crumb rubber improved the impact resistance and energy absorption capacity of concrete beam. In another study, Atahan and Yucel [60] used coarse and fine crumb rubber as aggregate replacement and performed drop impact tests on cylindrical specimens. Al-Tayeb et al. [38] carried out experimental and numerical studies to analyze the low velocity impact response of concrete beams in which sand and cement was partially replaced by crumb rubber. In their study, drop impact tests were performed on beams of size 400 mm × 100 mm × 50 mm. The specimens were subjected to an impact of 20 N weight from 300 mm elevation. They observed that the peak impact and bending force increased with the increase in rubber content. Although, several studies have been performed on rubberized concrete, the detailed experimental investigations including the time histories of impact force, displacement, and the fracture energy values for rubberized concrete against low velocity impact are lacking. Also, the design guidelines for using crumb rubber in concrete are not available.

Further, the influence of several types of fibers on the microstructural attributes of concrete has been well investigated [68–71]. It has been reported that the hydrophobic nature of synthetic fibers causes a weak interface with the cement paste in concrete [72]. Also, the microstructural analysis of rubberized concrete has been inspected by some studies [73–76], its influence on the low velocity impact response remains unexplored.

In order to improve the low velocity impact response of concrete, a comprehensive understanding regarding the influence of several parameters is necessary. This could be achieved by performing detailed parametric investigations. The experimental studies are not feasible for performing detailed parametric analysis of material parameters, due to involvement of high costs and considerable time requirement. Also, the analytical methods are very complex and have several limitations. With the recent evolution in numerical approaches, and establishment of material constitutive models, the utilization of numerical simulation methods for non-linear dynamic problems have become more reliable. Due to this, the Finite Element (FE) based numerical techniques have been commonly utilized for investigating the response of concrete under several loading scenarios [2, 77–80]. Thus, the numerical methods are suitable for performing the detailed parametric analysis of material parameters.

The numerical response of concrete can be modeled using several simplified and advanced constitutive models. Some of the examples are:

smeared cracking model, Concrete Damaged Plasticity (CDP) model, brittle cracking model, Holmquist-Johnson-Cook (HJC) model, and Johnson-Holmquist-2 (JH-2) model [23, 81–83]. However, smeared cracking and brittle cracking models are not suitable for modelling the response of concrete under impact loads [81]. These models assume that the compressive behavior of concrete is always linear elastic which is not the actual phenomenon in case of low velocity impact loading. Also, the use of HJC model and JH-2 model involves complexities associated with the determination of several parameters. The CDP model has been successfully used to model the low velocity impact behavior of concrete [2, 47, 83], and thus considered suitable for performing detailed parametric studies.

In the past, several studies have investigated the influence of CDP parameters on the response of concrete [84–87]. Hafezolghorani et al. [85] found that the increment in dilation angle of concrete resulted in higher flexibility. Demir et al. [87] concluded that the use non-zero values of viscosity parameter may lead to doubtful results. However, these studies were mainly focused on quasi-static loading conditions. The only available parametric studies on low velocity impact were conducted by Othman and Marzouk [2, 47]. In a part of their study, they performed parametric investigations on some CDP parameters for calibrating the FE model against experimental results. Although, the detailed parametric studies related to the influence of all CDP material parameters on the low velocity impact response are not available.

2.2 Blast loading on subsurface tunnels

Subsurface tunnels are substantially used for various utilities in metropolitan cities. However, they have become easy targets for terrorist attacks. The recent explosive events on subways of different cities have brought attention towards the blast resistant design of subsurface tunnels. An internal explosion may not only result in possible loss of human lives but also cause huge infrastructural damage and drastic financial losses. The damage induced in subsurface tunnels due to explosion depends on the tunnel lining material, quantity of explosive, and the neighboring geological condition [88, 89]. Thus, to reduce the potential damage of tunnels, it is necessary to explore for blast mitigation methods utilizing new materials as protective layer instead of designing an uneconomical rigid structure.

In the past, several experimental studies have investigated the response of reinforced concrete (RC) structural elements against blast loading [90–92]. Wang et al. [90] performed scaled blast studies on one way RC slabs, and observed that the scaling phenomenon has no effect on the macrostructure damage of the slab. Although, there is a reduction in local damage due to use of small-scale factors. Similar blast experiments have also been performed in other studies [91, 92]. However, the experimental studies related to internal blast loading on subsurface tunnels are not viable from socio-economic and political point of view. Since, the tunnel sections have considerable cross-sectional dimensions and complicated reinforcement arrangements, the experimental testing would require huge costs. Also, the blasting experiments must be performed with due care in a remote area due to the association of high risks, thus causing political issues. Due to this, the literatures related to internal explosion tests on tunnels are very scarce. The only available study was performed by Zhao et al. [93], in which they carried out full-scale internal explosion tests. This study was focused on the determination of critical points which control the response of tunnels as well as the damage and failure mechanisms which take place in case of an internal explosion. The drawback of this study was that the experimental blast tests were performed on vertically assembled tunnel linings, in which the cross-section of tunnel was kept horizontally on the ground. Hence, the effect of overburden pressure of soil lying above the tunnel surface in the practical case was not reproduced.

Apart from the experimental studies, analytical methods could also be utilized for the analysis of RC structural elements against internal blast.

However, the analytical methods evolved till now are based on simplifications, such as conversion of a problem to single degree of freedom (SDOF) or multiple degree of freedom (MDOF) system. The use of such simplifications for complicated subsurface structures such as circular tunnels may not reflect the actual scenario in case of internal blast. Hence, the analytical methods are not very accurate and remain unsuitable for the internal blast analysis of tunnels.

With the current progression in numerical methods, and evolution of material constitutive models, the reliability of numerical techniques for dynamic problems have increased. Therefore, the numerical investigation of tunnels subjected to internal explosion is very significant and can be carried out well using sophisticated FE packages. Previously, several numerical studies have been executed to investigate the dynamic response of underground structures and soil exposed to blast loading. Rigas and Sklavounos [94] generated blast wave using computational fluid dynamics (CFD) in a scaled model of a tunnel. They concluded that the space confinement provided by the tunnel section promotes the shock wave propagation and results in aggravation of the blast effects, while, in an unconfined space, the shock waves are easily deteriorated in a short span. Thus, a confined space is vulnerable to higher damage in case of blast generated shock wave propagation. CFD was also utilized by Chakraborty et al. et al. [88], and Chaudhary et al. [95] for performing a comparative study of different lining materials such as plain concrete, steel fiber reinforced concrete, steel, and various sandwich panels against blast loading. They found that the performance of sandwich panels is superior due to absorption of energy by foam. Also, the box shape tunnels are highly vulnerable to blast loads, and the tunnel linings suffer higher damage (displacement of tunnel crown) in case of rectangular shaped tunnels compared to that of circular tunnels. Gui and Chien [96] performed blast analysis for a reinforced cement concrete (RCC) tunnel passing below Taipei Shongsan airport using a finite difference program based on Fast Lagrangian Analysis of

Continua. This study concluded that the impact of weapon characteristics such as blast load intensity and crater size is much more profound compared to the soil characteristics, and a shielding layer must be used to absorb the blast energy instead of a costly structure.

Apart from these, several researchers utilized coupled 3D-FE analysis such as coupled Euler Lagrange (CEL) and Arbitrary Lagrangian Eulerian (ALE) techniques for studying the response of underground tunnels against explosive loading [97–100]. The use of CEL technique is advantageous in modeling the blast response of tunnels as it considers the different phenomenon such as reflection and focusing of shock waves developed in case of internal explosion accurately. However, due to the complex nature of the problem, the coupled analysis demands rigorous modeling efforts and hefty numerical simulations [101]. On the other hand, the uncoupled 3D-FE analysis methods (such as CONWEP) for modeling the blast loading are simpler and provide a good balance between computational expenses and accuracy. This tool neglects the effects of reflection. However, the validity of CONWEP tool for modeling the blast response of underground tunnels has been verified by many studies [5, 102–107]. Liu [102], Verma et al. [106], and Goel et al. [5] have analyzed the response of RC tunnels against internal explosion. Additionally, the CONWEP tool has been successfully used to study the blast response of steel tunnels [104].

Due to the strategic importance of underground tunnels, several studies have explored different techniques for blast mitigation and anti-blast design of underground tunnels. The idea for utilization of a sacrificial cladding layer is found to be a good option for blast resistant design [25, 108]. Guruprasad and Mukherjee [25] utilized layered mild steel cladding for dissipating blast energy. Hanssen et al. [109] used sacrificial layers of aluminum foam panel. Mandal et al. [110] utilized porous concrete, polymeric syntactic foam and closed cell aluminum foam as energy absorbing materials. Ma and Ye [111] performed an analytical investigation using rigid-perfectly plastic-locking foam model for investigating the performance of foam claddings under blast. Theobald and Nurick [112] performed experimental investigations for studying the response of tube core claddings composed of sandwich panels made of 6063-T6 aluminium alloy, or annealed mild steel. Zhao et al. [113] utilized foamed cement based sacrificial layers composed of expandable polystyrene (EPS) particles and cement matrix for blast mitigation of tunnel structures and concluded that the utilization of sacrificial layer reduces the stresses and velocity values for the tunnel structure in case of blast loading. Tarlochan et al. [114] studied the possibility of utilization of claddings manufactured from epoxy resin, polystyrene foam, and glass fiber using quasi-static compression tests on specimens.

The external bonding of fiber reinforced polymer (FRP) materials has been verified to be a successful strengthening technique for improving the strength, stiffness, impact resistance, and ductility, of various structural elements including columns, walls, beams, and slabs. It has gained high popularity due to its excellent properties, high tensile strength, and outstanding resistance to corrosion [115]. The use of FRP has been verified to improve the blast resistance of RC slabs [19, 116, 117]. In addition to this, it has been found to effectively strengthen the beams, columns, and masonry infills against impact loading [116]. Also, the use of carbon fiber reinforced polymer (CFRP) as protective shield has been found to improve the performance of tunnel against blast loading [29]. However, among the different FRP materials, GFRP is the most economical, with low conductivity and high thermal insulation properties which makes it suitable for strengthening the structural components against blast.

Although, the blast analysis of subsurface tunnels can be performed well using numerical techniques, it offers various challenges such as the consideration of effects of post peak dynamic behavior, mesh dependency, contact interaction between two surfaces, immense modeling work, and computational expenses. In short, the numerical blast analysis of RC tunnels is a complicated task with high computational expenses. Also, it is not possible to conduct sensitivity analysis, and parametric studies if wide range of input variables are present. Thus, there is a need to establish a predictive methodology with the accuracy of numerical methods and low computational expenses of semi-empirical methods which could be utilized for detailed blast analysis of underground RC tunnels.

Artificial Intelligence (AI) is suitable for accomplishing the objective discussed above. Fully trained AI models are very useful for rendering and establishing highly complex problems with numerous parameters and have the capability to give new predictions and perform a detailed analysis. Nowadays, AI is being widely utilized in civil and infrastructural engineering [31–33, 118, 119] as it demands lesser effort, easier implementation, and low computational expenses from the user. It has been used for optimization of parameters in infrastructural applications [120], as well as for detection of clogging in pipejacking operations [121]. Additionally, it has been utilized for forecasting the slump values and compressive strength of concrete [122], shear strength of SFRC, and RC [123, 124], deflection of RC beams [125], impact force due to drop weight in RC beams [126], and crack detection in concrete [127]. Recently, AI techniques have also been investigated for predicting the performance of RC structural members against blast loading. Shishegaran et al. [128] analyzed the performance of RC panels subjected to blast loading in terms of peak displacement. They used FE analysis and four subordinate models: multiple linear regression (MLR), multiple Log natural equation regression (MLnER), gene expression programming (GEP), and a combination of former three models. Almustafa and Nehdi [129] developed a machine learning (ML) model using Random Forests algorithm and a hybrid classification-regression Random Forests algorithm for predicting the maximum displacement of

RC slabs under blast loading considering ten input parameters. Additionally, some researchers have also contributed towards the exploration of novel methodologies for solution of different boundary value problems involving partial differential equations (PDE). Anitescu et al. [130] used a new mesh-free collocation method to improve the robustness as well as computational efficiency of artificial neural networks (ANN). Samaniego et al. [131] explored the possibility of utilization of deep neural networks (DNN) as an alternative to solve PDE involving applications in computational mechanics. They concluded that the energy approach could be effectively used for solving mechanical problems. Thus, from the comprehensive literature review, it was found that the use of AI has been widely explored for different engineering applications. Although, its use for predicting the response of subsurface RC tunnels under internal explosion remains unexplored.

2.3 Finite element analysis

The finite element method stands out as a highly efficient and precise numerical technique for simulating the dynamic response of structural components under extreme loading conditions [132]. Such an analysis could be performed using two softwares: ABAQUS and ANSYS. However, ABAQUS has a more powerful material library which also contains the basic structural components such as concrete, soil, and reinforcement. Further, ABAQUS offers better meshing capabilities for complicated structures and is superior in handling non-linear problems. ABAQUS has inbuilt Implicit/Explicit configurations which could be easily switched between steps. However, ANSYS relies on LS-DYNA for the explicit analysis. Hence, in this study, the finite element analysis is conducted utilizing the general-purpose software ABAQUS/Explicit [35]. This segment discusses the salient features of ABAQUS including the geometric modelling, and constitutive material modelling.

2.3.1 ABAQUS finite element software

ABAQUS is a commercial finite element software which is a widely renowned program, offered by Dassault Systems. It is a comprehensive three-dimensional package that encompasses advanced modeling capabilities. It incorporates an extensive library of elements and material constitutive models, facilitating the simulation of various materials with diverse geometries. ABAQUS is offered in three distinct products: Standard, Explicit, and CFD. Among these, ABAQUS/Standard and ABAQUS/Explicit are the two primary products employed for structural modeling applications.

ABAQUS/Standard can be used to solve an extensive array of linear and nonlinear problems using implicit integration algorithm including heat transfer, mass diffusion, acoustic behavior, as well as load/displacement analyses. The implicit integration method involves solution of a set of equilibrium equations for every time step, making it a direct-integration approach. In other words, implicit analysis demands the solution of complete global stiffness matrix, thus making this approach computationally expensive. Also, ABAQUS/Standard may not be able to provide efficient solutions for discontinuous problems, including sudden impact scenarios.

On the other hand, ABAQUS/Explicit has been specifically designed to effectively handle discontinuous problems including impact and blast loading scenarios. It utilizes an explicit integration algorithm in which the equations for current time step are used to determine the solutions for next time step by utilizing extrapolation techniques. Thus, the explicit method is efficient and demands lesser computational efforts. More information about ABAQUS/Explicit and its integration algorithm can be found in the ABAQUS User Manual [35].

2.3.2 Geometric modeling

In order to reproduce the real-world scenario, the geometric modeling of structural components should be done as accurately as possible. For extreme loading conditions, a three-dimensional finite element (3D-FE) modeling approach is preferred as it allows the consideration of crucial aspects such as confinement effects, shear, and concrete dilation. The geometric modeling of concrete can be done using tetrahedral or hexahedral elements utilizing first or second-order elements with reduced or full integration schemes. First-order elements employ linear interpolation techniques and only have nodes at the corners. While, second-order elements include a centroidal node and employ quadratic interpolation. The reduced integration method employs lesser integration points as compared to the full integration. Also, the first-order reduced-integration elements can be highly efficient and thus widely used for several type of problems in ABAQUS/Explicit [35].

Steel reinforcement can be modeled as a smeared reinforcement, or one-dimensional element inside concrete. While, thin FRP materials could be modeled using two-dimensional shell elements. The last method involves utilization of three-dimensional solid elements, which may be essential for concrete. However, the three-dimensional modeling of thin FRP materials or steel reinforcement would make the FE model highly complex.

2.3.3 Constitutive material modeling of concrete

In this study, the response of concrete structural components is modeled using concrete damaged plasticity (CDP) model. CDP model is one of the most assuring constitutive models utilized for simulating the response of concrete [133]. It was initially developed for monotonic loading by Lubliner et al. [134], later modified for dynamic loading by Lee and Fenves [135], and implemented in commercial 3D-FE software ABAQUS/EXPLICIT [35]. Also, it has the capability to represent the effects of strain rates. Thus, it is suitable for modeling the behavior of concrete under low velocity impact.

2.3.3.1. Uniaxial response

The typical uniaxial compressive and tensile stress-strain characteristics of concrete are shown in Figure 2.2. In uniaxial compression, the response of concrete is modeled in three stages. The first two stages represent the ascending response: linear elastic till initial yield stress (σ_{c0}) and plastic hardening till ultimate stress (σ_{cu}). The third stage represents the softening response (See Figure 2.2(a)). In case of uniaxial tension, response of concrete is linear elastic till failure stress (σ_{t0}), followed by softening response (See Figure 2.2(b)). The progression of yield or failure surface which represents the damage initiation is governed by two parameters: $\tilde{\varepsilon}_c^{pl}$ and $\tilde{\varepsilon}_t^{pl}$. These two parameters are the compressive and tensile equivalent plastic strains, respectively which are also called as the hardening variables. These are responsible for degradation of elastic stiffness.

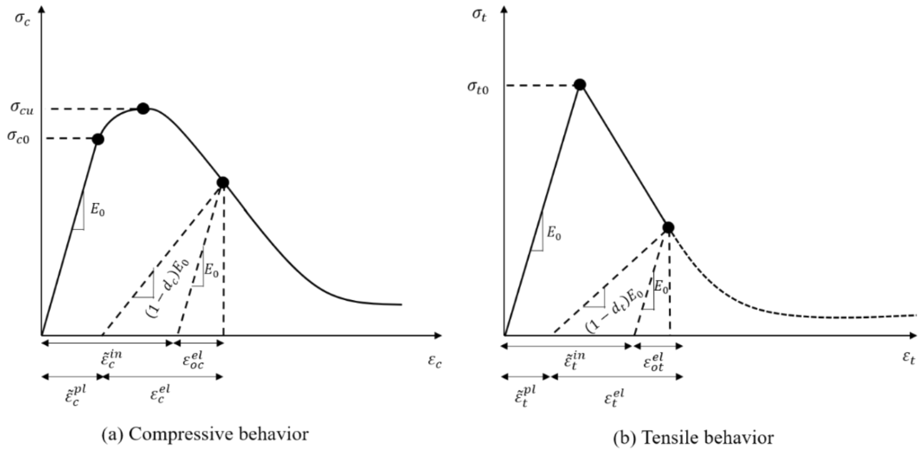

Figure 2.2 Uniaxial stress-strain characteristics in CDP model [35]

In ABAQUS, the uniaxial compressive and tensile characteristics of concrete are described as a tabular input in the form of stress-inelastic/cracking strain. The inelastic/cracking strain values can be calculated by the user by eliminating the elastic response of concrete as shown below:

$$\tilde{\varepsilon}_c^{in} = \varepsilon_c - \varepsilon_{oc}^{el} = \varepsilon_c - \frac{\sigma_c}{E_0} \tag{2.1}$$

$$\tilde{\varepsilon}_t^{in} = \varepsilon_t - \varepsilon_{ot}^{el} = \varepsilon_t - \frac{\sigma_t}{E_0} \tag{2.2}$$

where, compression and tension are represented as c and t respectively, $\tilde{\varepsilon}_c^{in}$ and $\tilde{\varepsilon}_t^{in}$ are the inelastic strain values, ε_c and ε_t are the total strain values, ε_{oc}^{el} and ε_{ot}^{el} are the elastic strain values, σ_c and σ_t are the values of stresses, and E_0 is the elastic stiffness of concrete in undamaged condition. The elastic stiffness degradation is considered using damage variables (d_c, and d_t). The values of these damage variables may vary from zero to one. Where, zero depicts undamaged material, while the latter denotes complete damage of material.

The user defined input stress-inelastic/cracking strain values are automatically converted to stress-plastic strain values by ABAQUS using the provided damage variables and the stress-strain relationships are formulated as shown below:

$$\sigma_c = (1 - d_c)E_o\left(\varepsilon_c - \tilde{\varepsilon}_c^{pl}\right) \tag{2.3}$$

$$\sigma_t = (1 - d_t)E_o\left(\varepsilon_t - \tilde{\varepsilon}_t^{pl}\right) \tag{2.4}$$

2.3.3.2. Yield surface and flow potential

When the concrete material is loaded beyond elastic limit (yield load), a part of deformation exists even after the removal of load which represents permanent material damage. The value of this yield load/stress is governed by a 3D yield surface. In CDP model, the yield surface is a modified Drucker-Prager model [134, 135] (See Figure 2.3(a)). The yield surface is a function of effective stress values as shown below:

$$F = \frac{1}{1-\alpha}\left(\bar{q} - 3\alpha\bar{p} + \beta\left(\tilde{\varepsilon}_{pl}\right)\langle\hat{\bar{\sigma}}_{max}\rangle - \gamma\langle-\hat{\bar{\sigma}}_{max}\rangle\right) - \bar{\sigma}_c\left(\tilde{\varepsilon}_c^{pl}\right) = 0 \tag{2.5}$$

In the above equation, the various parameters are:

$$\alpha = \frac{\sigma_{bo} - \sigma_{co}}{2\sigma_{bo} - \sigma_{co}} = \frac{(\sigma_{bo}/\sigma_{co}) - 1}{2(\sigma_{bo}/\sigma_{co}) - 1} \tag{2.6}$$

$$\beta = \frac{\bar{\sigma}_c\left(\tilde{\varepsilon}_c^{pl}\right)}{\bar{\sigma}_t\left(\tilde{\varepsilon}_t^{pl}\right)}(1-\alpha) - (1+\alpha) \tag{2.7}$$

$$\gamma = \frac{3(1-K_c)}{2K_c - 1} \tag{2.8}$$

$$\bar{p} = -\frac{I_1}{3} = -\frac{1}{3}\text{trace}(\bar{\sigma}) \tag{2.9}$$

$$\bar{q} = \sqrt{3J_2} = \sqrt{\frac{3}{2}\bar{S}:\bar{S}} = \sqrt{\frac{3}{2}\text{trace}(\bar{S}^T\bar{S})} \tag{2.10}$$

$$\bar{S} = \bar{p}I + \bar{\sigma} \tag{2.11}$$

$$K_c = \bar{q}_{TM}/\bar{q}_{CM} \tag{2.12}$$

$$\bar{\sigma}_c = \frac{\sigma_c}{1-d_c} = E_o\left(\varepsilon_c - \tilde{\varepsilon}_c^{pl}\right) \tag{2.13}$$

$$\bar{\sigma}_t = \frac{\sigma_t}{1-d_t} = E_o\left(\varepsilon_t - \tilde{\varepsilon}_t^{pl}\right) \tag{2.14}$$

where, α and γ are the dimensionless constants, $\bar{p}$ is the effective hydrostatic pressure, $\bar{q}$ is the effective Mises stress, $\bar{\sigma}_c$ and $\bar{\sigma}_t$ are the effective stress values in compression and tension respectively, $\tilde{\varepsilon}_{pl}$ is the equivalent plastic strain, $\hat{\bar{\sigma}}_{max}$ is the maximal effective principal stress, $\langle\rangle$ is the Macaulay's bracket which is defined as $\langle x \rangle = (|x| + x) / 2$. σ_{bo} and σ_{co} are the initial biaxial and uniaxial yield stresses in compression (failure compressive stress) respectively, I_1 and J_2 are the first and second stress invariants of stress tensor respectively, $\bar{S}$ is the deviatoric portion of effective stress tensor ($\bar{\sigma}$), I is the identity matrix, T represents the Transpose. $\bar{q}_{TM}$ and $\bar{q}_{CM}$ are the effective Mises stresses in tensile and compressive meridian respectively. The tensile meridian (TM) may be defined as the locus of stress conditions which fulfill the criteria: $\hat{\bar{\sigma}}_{max}$=$\hat{\bar{\sigma}}_1 > \hat{\bar{\sigma}}_2 = \hat{\bar{\sigma}}_3$, while the compressive meridian (CM) is the locus of stress conditions satisfying: $\hat{\bar{\sigma}}_{max} = \hat{\bar{\sigma}}_1 = \hat{\bar{\sigma}}_2 > \hat{\bar{\sigma}}_3$, respectively, where, $\hat{\bar{\sigma}}_1$, $\hat{\bar{\sigma}}_2$, and $\hat{\bar{\sigma}}_3$ are the eigen values of effective principal stress tensors.

The shape of yield surface in deviatoric plane is governed by shape parameter (K_c) which is represented in Figure 2.3(a) in which S_1, S_2, and

S_3 are the principal deviatoric stresses. The value of K_c may range from 0.5 to 1. For K_c=1, the yield surface takes a circular shape as in case of the classical Drucker Prager theory. While, the CDP model incorporated in ABAQUS recommends use of $K_c = 2/3$.

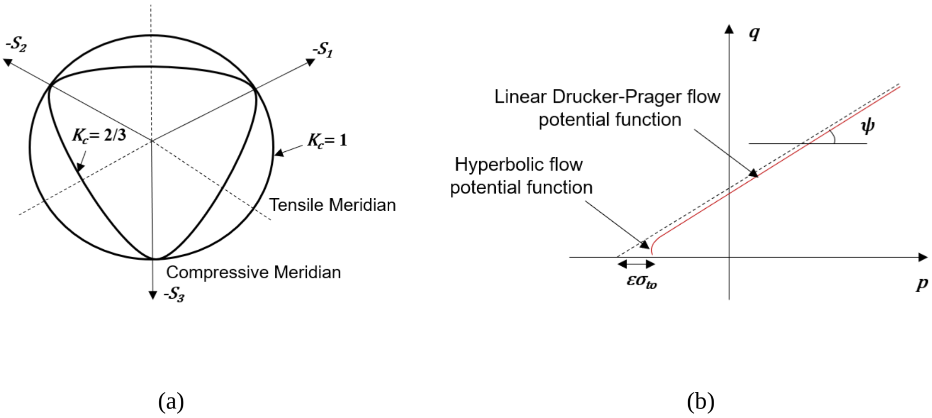

Figure 2.3 Yield surface and flow potential of CDP model in (a) deviatoric plane (b) meridional plane

CDP model considers a non-associated flow potential which is shown in Figure 2.3(b). The equation for flow potential is shown below:

$$\dot{\varepsilon}_{pl} = \dot{\lambda}\frac{\partial G(\bar{\sigma})}{\partial \bar{\sigma}} \tag{2.15}$$

where, $\dot{\varepsilon}_{pl}$ is the plastic strain rate, G is the potential function, and $\dot{\lambda}$ is a hardening parameter. The potential function in the meridional plane (p-q) is given as:

$$G = \sqrt{(\varepsilon\sigma_{t0}\tan\psi)^2 + \bar{q}^2} - \bar{p}\tan\psi \tag{2.16}$$

where, ψ is the dilation angle which is computed in the meridional (p-q) plane (See Figure 2.3(b)). It is the angle at which yield/failure surface is inclined with respect to hydrostatic axis. σ_{t0} is the value of failure stress in uniaxial tension. ε is the eccentricity parameter which governs the rate at which the yield surface advances asymptote in meridional plane (See Figure 2.3(b)). The default value of eccentricity parameter as recommended by ABAQUS is 0.1. $\varepsilon\sigma_{t0}$ is the length of segment along hydrostatic axis between the vertex of hyperbola and the intersection point of asymptotes. Compressive biaxial to uniaxial yield strength ratio

$(\sigma_{bo}/\sigma_{co})$ is another important CDP parameter describing the response of concrete material. Its default value as recommended by ABAQUS is 1.16. The four parameters K_c, σ_{bo}/σ_{co}, ψ, ε, along with the damage parameters and the stress-strain behavior of concrete constitute the complete input characteristics for CDP model. The CDP model does not include the effects of strain rate by itself. Hence, modified stress-strain curves as function of inelastic/cracking strain must be provided as an input in tabular function by the user.

2.3.3.3 Effects of strain rate

The effects of strain rate are commonly accounted using Dynamic Increase Factor (DIF). It is the ratio of dynamic to static strength of material. In the literatures, various DIF models have been reported. However, the DIF formulas presented in CEB-FIP [136] model code are the most thorough formulations and have been successfully utilized by several researchers for modeling the behavior of concrete at high strain rates [2, 47, 137, 138]. One of the main advantages of using this model is that it can be utilized for concrete having compressive strength up to 120 MPa as well as for a maximum strain rate value of 300 s^{-1}. The DIF formulations for concrete at higher strain rates are shown Appendix 1.

Since, CDP model utilizes a non-associated flow potential, it demands solution of unsymmetric equations. This is carried out in ABAQUS, which harmonizes the complete model using backward Euler method in which a material Jacobian consistent with integration operator is used for carrying out iterations [35], and finally the results are obtained as per the applied loading and boundary conditions.

2.3.4 Constitutive material modeling of GFRP

The constitutive modeling of GFRP can be carried out using macroscopic or microscopic models. Among these, the macroscopic models are preferred due to their easy application. However, these models fail to predict the failure mode initiation. The microscopic models reported in Hashin et al. [139, 140] consider the failure mode initiation accurately and are also capable of reflecting the different failure modes. Hence, in the present work the mechanical behavior of GFRP layer is simulated using anisotropic Hashin damage model [139, 140]. This model is based on the average stress-strain method.

$$A_1J_1 + B_1J_1^2 + A_2J_2 + B_2J_2^2 + C_{12}J_1J_2 + A_3J_3 + A_4J_4 = 1 \qquad (2.17)$$

Where J_1, J_2, J_3, J_4 are invariants which are given by,

$$J_1 = \sigma_{11} \qquad (2.18)$$

$$J_2 = \sigma_{22} + \sigma_{33} \qquad (2.19)$$

$$J_3 = {\sigma_{23}}^2 - \sigma_{22}\sigma_{33} \qquad (2.20)$$

$$J_4 = {\sigma_{12}}^2 + {\sigma_{13}}^2 \qquad (2.2)$$

And A_1, A_2, A_3, A_4, B_1, B_2, and C_{12} are the constants determined for different states of stress.

$$A_3 = \frac{1}{\tau_T^2} \qquad (2.22) \qquad A_4 = \frac{1}{\tau_A^2} \qquad (2.23)$$

Eqn. 2.17 can be rewritten as

$$A_f\sigma_{11} + B_f\sigma_{11}^2 + \frac{1}{\tau_A^2}({\sigma_{12}}^2 + {\sigma_{13}}^2) = 1 \qquad (2.24)$$

Also, the matrix failure mode can be denoted as

$$A_m(\sigma_{22} + \sigma_{33}) + B_m(\sigma_{22} + \sigma_{33})^2 + \frac{1}{\tau_T^2}({\sigma_{23}}^2 - \sigma_{22}\sigma_{33}) + \frac{1}{\tau_A^2}({\sigma_{12}}^2 + {\sigma_{13}}^2) = 1 \qquad (2.25)$$

Here, A_f, B_f, A_m, B_m represent the coefficients of the failure criteria, and σ represents the stress.

2.3.5 Modeling of blast loading

In this study, the spherical TNT explosive is modeled using CONWEP tool. It is based on the studies of the U.S. Army Corps of Engineers (USACE) [141]. In CONWEP, pressure-time plot is assumed to take a triangular shape and its time period is determined using the reflected pressure diagram. It is an empirical model based on the experimental results. In this model, the characteristic explosive parameters are used to determine the shock-wave overpressure and its velocity. According to this model, the wave propagates spherically from the point of detonation and impinges the elements of a structure. The equations used in CONWEP tool as reported in ABAQUS user manual [35] are as follows:

$$\overline{\mathrm{P}}(\mathrm{t}) = \mathrm{P}_{\mathrm{incident}}(\mathrm{t}) + [1 + \cos\theta - 2\cos^2\theta] + \mathrm{P}_{\mathrm{reflect}}(\mathrm{t})\cos^2\theta \quad \text{for } \cos\theta \geq 0 \qquad (2.26)$$

$$\overline{\mathrm{P}}(\mathrm{t}) = \mathrm{P}_{\mathrm{incident}}(\mathrm{t}) \text{ for } \cos\theta < 0 \qquad (2.27)$$

Where, $\overline{\mathrm{P}}(\mathrm{t})$ is the total pressure due to explosion, $P_{incident}(t)$ is the pressure due to incident wave, $P_{reflect}(t)$ is the pressure due to reflected wave, and θ is the angle of the line normal to the loading surface with respect to the line connecting it to the point of explosion.

The incident overpressure peak ($\mathrm{P}_{\mathrm{incident}}$) and reflected pressure ($\mathrm{P}_{\mathrm{reflect}}$) is evaluated using equations given by Karlos and Solomos [142] as shown below:

$$\mathrm{P}_{\mathrm{incident}}(\mathrm{t}) = \exp\left(0.14 - 1.49\ln\mathrm{Z} - 0.08\ln^2\mathrm{Z} - 0.62\sin(\ln\mathrm{Z})\right)\left(1 + \frac{1}{2\mathrm{e}^{10\mathrm{Z}}}\right) \qquad (2.28)$$

$$\mathrm{P}_{\mathrm{reflect}}(\mathrm{t}) = \exp\left(1.83 - 1.77\ln\mathrm{Z} - 0.1\ln^2\mathrm{Z} - 0.94\sin(\ln\mathrm{Z})\right)\left(1 + \frac{1}{2\mathrm{e}^{10\mathrm{Z}}}\right) \qquad (2.29)$$

$$Z = \frac{R}{\sqrt[3]{W}} \quad (2.30)$$

Where, Z is the dimensional scaled distance, R is the distance of the point of detonation from the point under consideration, W is the mass of explosive in kg, P_o is the ambient pressure around explosive.

2.4 Artificial intelligence (AI)

2.4.1 Artificial Neural Network (ANN)

ANN is a computational tool developed to analyze and process complex data which can solve most real-life problems. The foundation of AI is mainly based on ANN and it has the capability to solve complex problems in lesser time and low computational cost [143]. One of the most intriguing aspects related to ANN is its capability to mimic human brain by admitting self-organization, adaptive learning, and fault tolerance qualities. With minimum human programming, ANN models can learn as well as enhance their performance while producing high quality outcomes. The intelligence factor associated with ANN along with the speed, latency, accuracy, convergence, and volume makes it a desirable model for several applications [144].

ANN has numerous artificial neurons (processing units) connected by nodes which form a massive, interconnected structure. It is a data driven modeling approach in which an approximation function is used to predict the output of the system. Several types of neural networks (NN's) are available, however, the multilayer NN (See Figure 2.4) is the most widely adopted and also used in the present study. It has several numbers of layers with a dense interconnection as well as back propagation between each layer. The equations for ANN with one and two hidden layers are as given below:

$$v = f_2\left[w_2 \sum_{i=1}^{n} f_1(w_1 y_i + b_1) + b_2\right] \quad (2.31)$$

$$v = f_3\left[w_3 \sum f_2\left(\sum_{i=1}^{n} f_1(w_1 y_i + b_1) + b_2\right) + b_3\right] \qquad (2.32)$$

where, v is the output, $y_i$represents the input parameters, w_1, w_2, and w_3 are the weights connecting the different layers, f_1, f_2, f_3 are the transfer functions, b_1, b_2, b_3 are the biases in different layers.

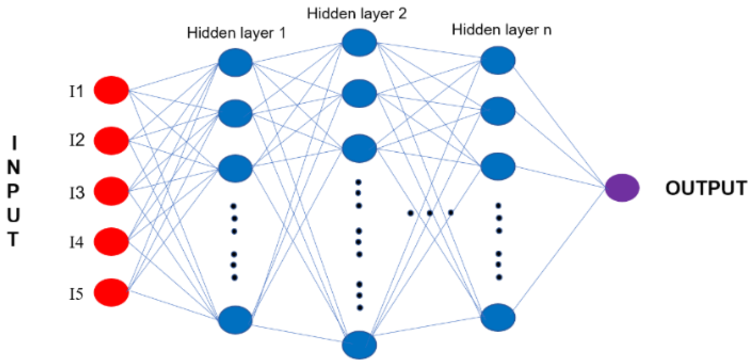

Figure 2.4 General formulation of ANN

2.4.2 Support Vector Machines (SVM)

SVM is a binary learning machine algorithm which can be used for solving classification as well as regression problems. In SVM each data point is plotted in a n-dimensional space and a hyperplane is constructed which acts as a decision surface such that the two different types of samples are well separated. It is a direct learning algorithm in which kernel functions are utilized to transform nonlinear relationship to a linear relationship. This method maps the dataset to a higher dimensional space such that the nonlinearities in the dataset are curbed to form a linearly separable set of data with a specific weight. The prediction of peak displacement of RC tunnel crown is done using regression algorithm of SVM. The algorithm develops an estimation function based on the dataset of peak displacement as shown below:

$$g(x) = w^M \theta(x) + \varepsilon \qquad (2.33)$$

where, x is the input vector; w is the vector weight, $w \in S^n$; M is the intercept; $\theta(x)$ is the mapping of x, $x \in S^n$.

2.4.3 Random Forests (RF)

Random Forests is an ensemble machine learning algorithm which has numerous discrete decision trees which form a forest such that the characteristics of sample data could be predicted. It is fast, accurate, simple, and flexible and can be used for solving classification, prediction as well as regression problems. In this algorithm, each decision tree gives a prediction, and the result is taken as the average or the decision with the highest number of votes (See Figure 2.5). This model is based on the idea that a family of non-related but numerous decision trees will perform better than the individual decision-making models. Since, the trees are very sensitive, each one is free to arbitrarily select the data from dataset with the capability of replacement which is also known as bagging in this algorithm. RF works in such a way that the variance as well as bias in prediction is low. Also, this model utilizes a cross-validation technique during training and helps in preventing overfitting of data [145].

In this model, the probability of non-selection of a data by any sample of the tree is given as $(1 - 1/\mathrm{n})^{\mathrm{n}}$, where n is the number of data points available in training phase. As the value of n advances infinity, the probability of non-selection of a data becomes approximately 0.37 [146]. This data is also known as out of the bag data which is used for internally validating the model during training phase and evaluate the performance and accuracy of RF algorithm utilized.

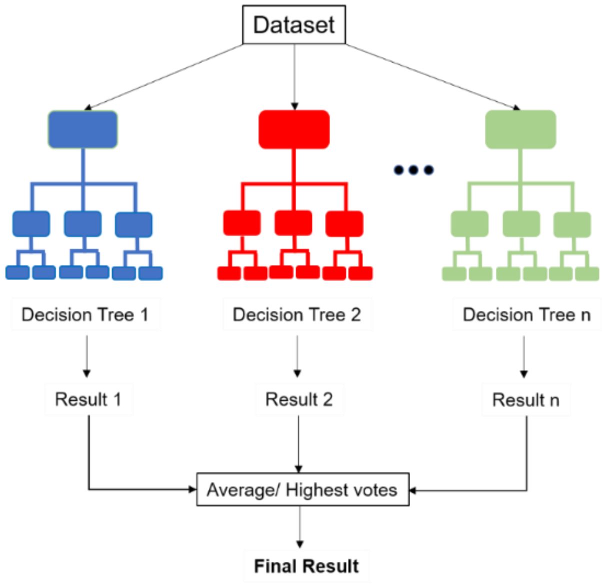

Figure 2.5 Typical random forests algorithm

2.4.4 Performance indices for AI models

The performance of AI models is evaluated using five assessment metrics: root mean square error (RMSE), coefficient of determination (R^2), mean absolute error (MAE), mean absolute percentage error (MAPE), and variability account for (VAF). These are calculated using Eqns. (2.46) - (2.50), and used to select the model exhibiting best performance. The details and significance of statistical parameters used as performance indices in this study are shown below:

$$\mathrm{RMSE} = \sqrt{\frac{\sum_{i=1}^{n}(y_i - \hat{y}_i)^2}{n}} \tag{2.34}$$

$$R^2 = 1 - \frac{\sum_i (y_i - \hat{y}_i)^2}{\sum_i (y_i - \bar{y})^2} \tag{2.35}$$

$$\mathrm{MAE} = \frac{1}{n}\sum_{i=1}^{n} |y_i - \hat{y}_i| \tag{2.36}$$

$$\mathrm{VAF} = \left(1 - \frac{\mathrm{var}(y_i - \hat{y}_i)}{\mathrm{var}(y_i)}\right) \times 100 \tag{2.37}$$

$$\mathrm{MAPE} = \frac{1}{n}\sum_{i=1}^{n} \left|\frac{y_i - \hat{y}_i}{y_i}\right| \times 100\ \% \tag{2.38}$$

In these equations, n is the total number of samples, y_i, $\hat{y}_i$, and $\bar{y}$ are the actual, predicted, and mean values of peak displacement respectively. A complete idea regarding the error distribution is provided by RMSE [147], R^2 is a correlation measure and gives an idea about the fit of the data, MAE is the average magnitude of errors and represents the model stability. MAPE is the mean of absolute percentage errors of forecast and it measures accuracy of a predictive model in terms of percentage. VAF tells whether the model accurately predicts the actual data. For an ideal model, RMSE and MAE should be 0, while R^2 should be 1, MAPE should be 0 % and VAF should be 100 %.

Chapter-3

Comprehensive parametric investigation on the low velocity impact behavior of concrete

3.1 Introduction

Concrete structures such as bridge columns, containments, precast piles, offshore structures, railroad sleepers, and industrial buildings are susceptible to impact loads resulting from accidental events. Most of the accidental events are associated with low velocity impact (≤ 10 m/s) [2, 148]. Different real-life examples include: aircraft landing on runways, rockfall protection structures subjected to impact of falling rocks, vehicular collision with transportation structures, industrial buildings subjected to accidental drop of heavy loads, offshore structures subjected to ship or ice impact, civil structures subjected to projectile impact or blasting events. Typically, the concrete structures are designed to satisfy the ultimate limit state criteria considering quasi-static loading conditions. However, their performance under low velocity impact may be unsatisfactory.

When a concrete structural element is subjected to low velocity impact, extreme stresses are transferred, and compression waves are generated on the impacted side. These compression waves travel towards the far side and get reflected as tension waves in a short duration of time. Thus, tensile stresses are produced due to impact loading. Since, the tensile and flexural strength characteristics of concrete are considerably low as compared to that of its compressive strength, an extreme event may affect its overall performance. Also, concrete has poor energy absorption capability due to its heterogeneous and brittle nature. This significantly affects the performance of concrete under low velocity impact.

Till date several studies have explored different methods for improving the ductility and energy absorption of concrete [3, 12–16, 18, 23, 38, 149]. These methods include: the utilization of fibers in concrete, use of reinforcement and prestressing in concrete, and external bonding of high strength materials. The above discussed methods can beneficially be utilized for improving the response of concrete under impact. However, these methods may have their own drawbacks. For example, the utilization of fibers in concrete may adversely affect the workability, especially when rubber and steel fibers are used [150, 151]. Also, the weak intermolecular bond between cement matrix and rubber fibers may affect the compressive strength and elastic modulus of concrete [73]. Despite the small drawbacks most of the above discussed methods are very useful. Although, it is necessary to develop a comprehensive understanding regarding the effects of several parameters on the low velocity impact response of concrete, such that an improved performance could be achieved.

The experimental studies related to detailed parametric analysis of material parameters are not feasible due to involvement of high costs and considerable time requirement. Also, the analytical methods are very complex and have several limitations. With the recent evolution in numerical approaches, and establishment of material constitutive models, the utilization of numerical simulation methods for non-linear dynamic problems have become more reliable. Due to this, the Finite Element (FE) based numerical techniques have become a favorable choice for investigating the response of concrete under several loading scenarios [47, 77, 80]. Thus, the numerical technique incorporating 3D-FE method has been considered for carrying out the detailed parametric investigation in this study.

Although, the numerical modeling of concrete may be carried out using different simplified and advanced constitutive models [23, 81, 149, 152]. The use of CDP model has gained the attention of researchers in the recent time. Also, CDP model has been found to be suitable for modelling the low velocity impact behavior of concrete [2, 153], and thus given consideration for performing detailed parametric investigation in this study.

Previously, some studies have investigated the influence of CDP parameters on the response of concrete [2, 47, 84–87]. However, most these studies were mainly focused on quasi-static loading conditions. The most closely related work in the context of the present study is the research carried out by Othman and Marzouk [2, 47]. They performed parametric investigations on some CDP parameters. However, the detailed parametric studies related to the influence of all CDP material parameters on the low velocity impact response are not available.

In this work, a 3D-FE approach is used to determine the desirable set of values of CDP model parameters which could be beneficial in improving the response of concrete under low velocity impact. Further, the influence of compressive strength and longitudinal reinforcement is also studied experimentally as well as numerically. In order to achieve this objective, a detailed parametric investigation is performed for a concrete beam which is impacted by 6 kg drop weight from a height of 500 mm. The response of concrete is simulated using CDP model, and the values of stress-strain characteristics of concrete at higher strain rates are developed using dynamic increase factors. The material parameters of concrete beam are varied over an extensive range of values and their influence on the response of concrete beam is investigated. Finally, the desirable value of each parameter resulting in improved response of concrete beam are sought.

3.2 Proposed methodology

In this work, a 3D-FE approach incorporating CDP model is used to develop a set of parameters which could be utilized to improve the response of concrete under low velocity impact. The flowchart of the proposed approach is displayed in Figure 3.1. A FE model of the concrete beam is developed in order to analyze its response. The model is validated against experimental investigations and the default values of CDP parameters reproducing the actual response of concrete beam are established. Different FE simulations are carried out in order to analyze the influence of CDP parameters [e.g., K_c, σ_{bo}/σ_{co}, ψ, ε, G_f (Fracture energy), and stress-strain response of concrete under compression]. The parameters are varied over a broad range (see Figure 3.1) and the performance of concrete beam is investigated. The response of concrete beam is quantified in terms of energy absorption capacity, which is determined as the area under impact force vs displacement curve. Finally, the desirable value of each CDP parameter resulting in an improved response of concrete beam are sought and thus a new set of parameters are recommended.

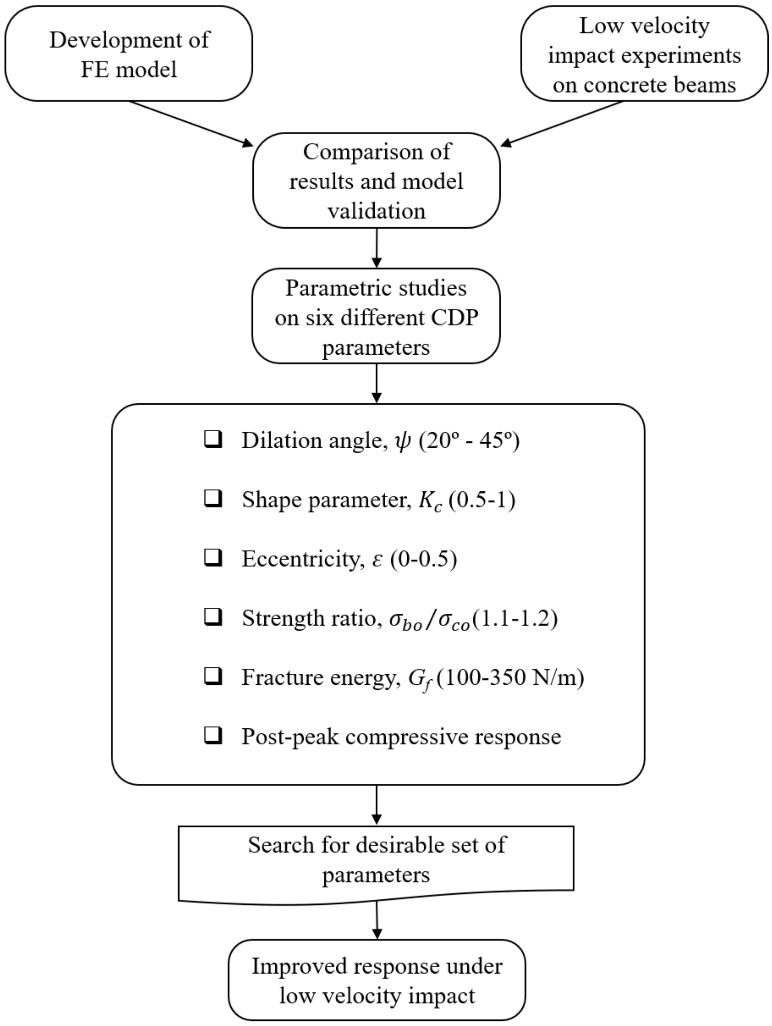

Figure 3.1Flowchart of the proposed methodology

3.3 Numerical modeling

3.3.1 Geometric modeling

The FE analysis is carried out using ABAQUS/EXPLICIT [35]. A 0.5 meter long concrete beam with square cross-section of 100 mm × 100 mm is modelled. The concrete beam is impacted by 6 kg drop weight, freefalling from 500 mm height. The mass of impactor (drop weight) considered in this study represents a typical loading scenario of a small scale rockfall or accidental impact, which is in accordance with the impact loading conditions considered in the previous studies carried out on similar concrete beams [154, 155]. The geometric and meshing details of the various components are shown in Figure 3.2. The supporting arrangement consists of two cylindrical supports, each having a diameter of 15 mm (See Figure 3.2(d)). The supports are provided at a spacing of 400 mm. The beam is placed over cylindrical supports such that an overhang of 50 mm is obtained on each side of the beam as shown in Figure 3.3. The flat nose impactor has a diameter of 15 mm and its height is 30 mm. The size of the impactor is kept fixed and its density is altered in order to achieve 6 kg mass.

The geometric model of beam is developed using 3D deformable solid component and meshed using eight node hex dominated reduced integration solid elements (C3D8R) based on Lagrangian assumption. The reinforcement is modelled as a 3D deformable truss and meshed using 2 node truss elements (T3D2). While, the drop weight (impactor) and supports are modelled using discrete rigid components and meshed using 3 node rigid triangular (R3D3) and 4 node rigid quadrilateral (R3D4) elements, respectively. In order to reproduce accurate shape of components, the deviation of internal angles of an element with respect to regular shaped elements should be negligible [156]. Hence, the drop weight and supports are meshed using sufficiently fine elements such that accurate geometry is achieved. Since, it is observed in the experimental studies that the drop weight and supporting system do not undergo any plastic deformation during the impact experiments, hence they are modelled using elastic material properties of steel (see Table 3.1). Also, the reinforcing steel is modelled using elastoplastic properties of Fe500 structural steel, which are taken from Iqbal et al. [22].

The interaction between beam and drop weight, as well as between beam and supports are defined using general contact algorithm. The general contact algorithm can be used to replicate 3D edge to surface contact. However, the surface-to-surface contact can be used to model contact between two surfaces only. Due to the curved shape of cylindrical supports, general contact algorithm is preferred in this work. The normal direction response reflecting the pressure behaviour of contact interaction is modelled as hard contact, which restricts the transmission of tensile stresses across the interface. The frictional behaviour between contact surfaces is modelled using isotropic penalty function formulation. The friction coefficient value is selected as 0.4 [157]. In order to reduce the computational time, the bottom portion of drop weight is kept very close to the beam with an offset of 1 mm above the beam surface. The velocity of drop weight is obtained from experimental investigations and provided as an input predefined field in the load module of ABAQUS/EXPLICIT. The supporting systems are provided with fixed boundary conditions in all directions using ENCASTRE option in LOAD module of ABAQUS/EXPLICIT. While, the boundary condition for drop weight is kept such that it is allowed to move freely in vertical direction only and the displacements as well as rotations in all other directions are constrained.

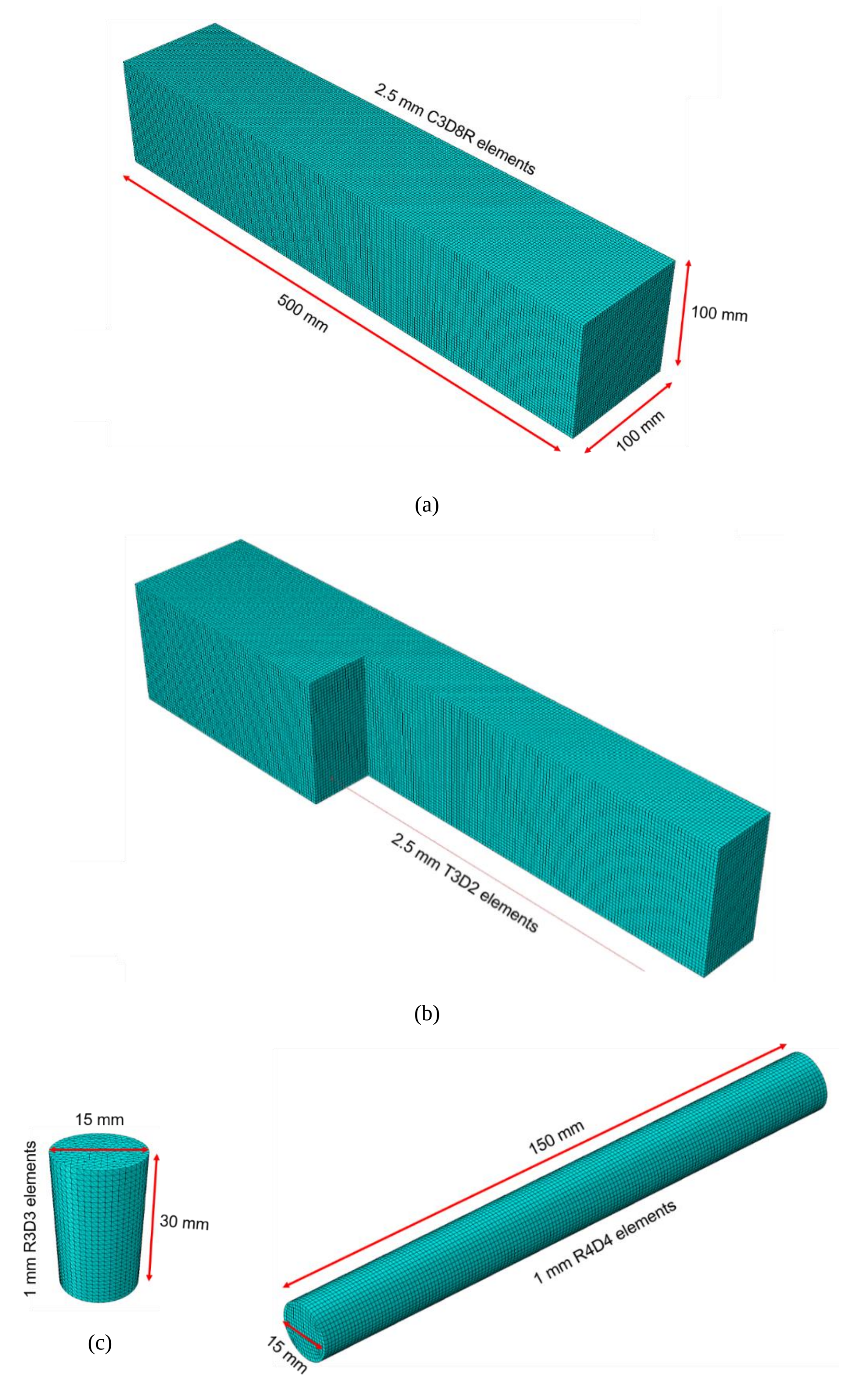

Figure 3.2 Geometric and meshing details of (a) plain concrete beam, (b) RC beam, (c) impactor, and (d) cylindrical supporting arrangement

Table 3.1 Elastic properties of supporting system and drop weight

Component	Elastic properties	Value

Supporting system	Modulus of elasticity (GPa)	210
	Density (kg/m^3)	7850
	Poisson's ratio	0.3
Drop weight	Modulus of elasticity (GPa)	210
	Density (kg/m^3)	1131770
	Poisson's ratio	0.3

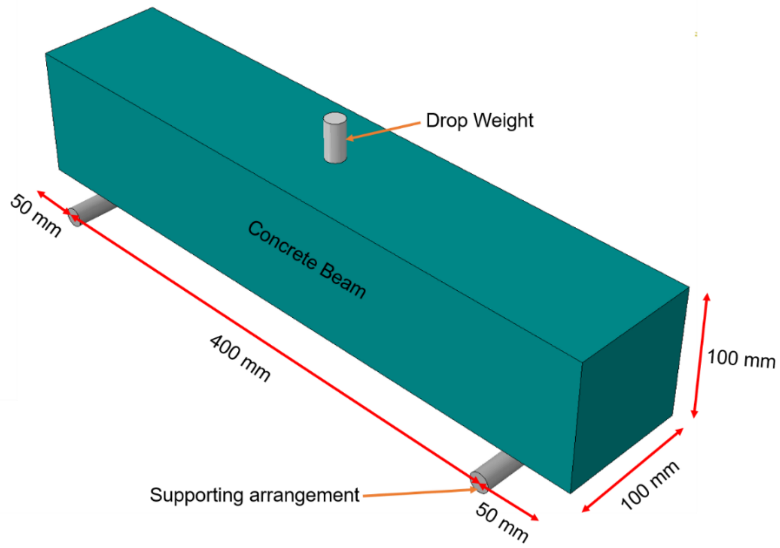

Figure 3.3 FE model of the drop impact test

3.3.2 Material constitutive modeling

The constitutive modelling for concrete is carried out using CDP model. The initial values of input parameters for M50 grade concrete are taken from previous literatures [158, 159]. These, values are used to perform FE simulations and the obtained results are compared with the experimental counterparts for accurate calibration of the FE model. Lastly, the values of parameters reflecting the actual response of concrete beams are established and these values are termed as "Default parameters". Table 3.2 lists the values of default parameters which are used for subsequent parametric investigations. The uniaxial compressive stress-strain behavior of concrete is developed using piecewise linear models utilizing the experimental stress-strain data reported in Jankowiak and Lodygowski [158]. While, the tensile behavior of concrete is modelled using post-peak tensile stress-crack width characteristics, rather than stress-strain characteristics to avoid mesh sensitivity. The post-peak tensile stress-crack width model employed in this study is presented in Figure 3.4. This model utilizes a bilinear curve which is modified version of Hillerborg's crack model [160]. The Hillerborg's crack model allows full damage of material which may critically affect the convergence of solution [35]. Hence, it is modified in order to avoid full damage. It is known that the progression of crack width results in reduction of tensile yield stress. For example, when the value of crack width becomes $\frac{0.8G_f}{f_t}$, the remaining tensile strength is only one third of the ultimate tensile strength. Where, G_f represents the fracture energy, while f_t represents the ultimate tensile strength. The quasi-static uniaxial compressive and tensile response of concrete is presented in Figure 3.5.

Table 3.2 General, elastic material properties and default CDP model parameters of concrete

Property	Value
Density, ρ (kg/m^3)	2,489
Unconfined compressive strength, f_c' (MPa)	48
Elastic modulus, E_c (GPa)	29.955
Fracture energy, G_f (N/m)	112[a]
Poisson's ratio, ν	0.19
Dilation angle, ψ	20°
Shape parameter, K_c	0.67
Flow potential eccentricity, ε	0.1
Biaxial to uniaxial yield strength, σ_{bo}/σ_{co}	1.16
Viscosity parameter, μ	0

[a]Based on Ulfkjaer and Brincker [159]

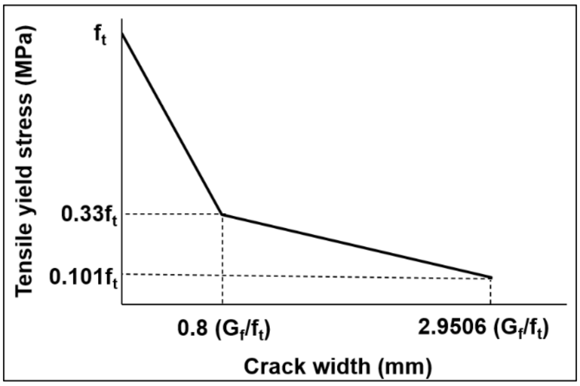

Figure 3.4 Modified Hillerborg's crack model for post-peak tensile response of concrete

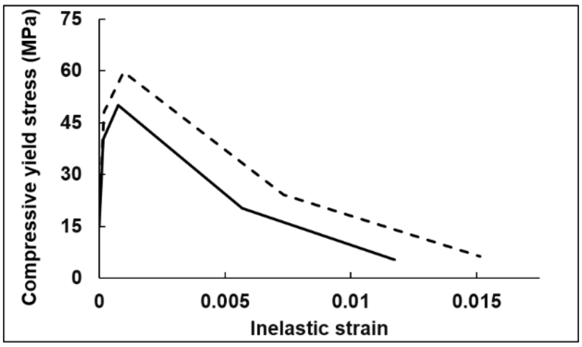

(a)

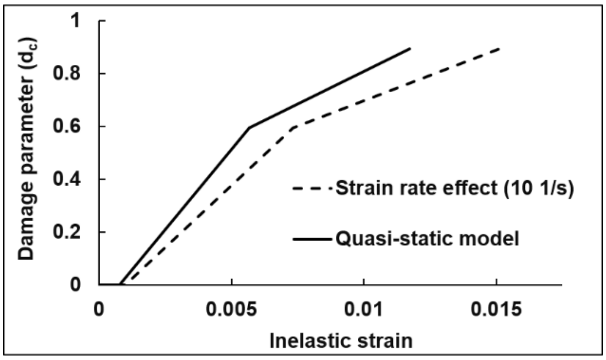

(b)

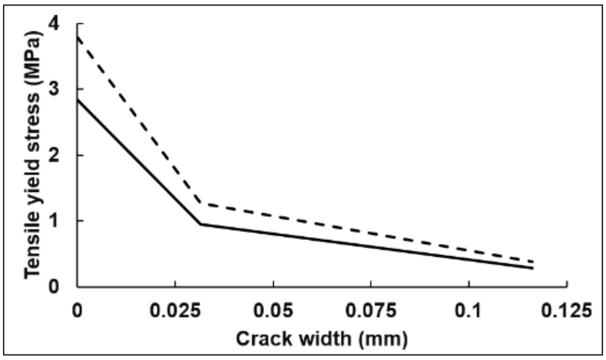

(c)

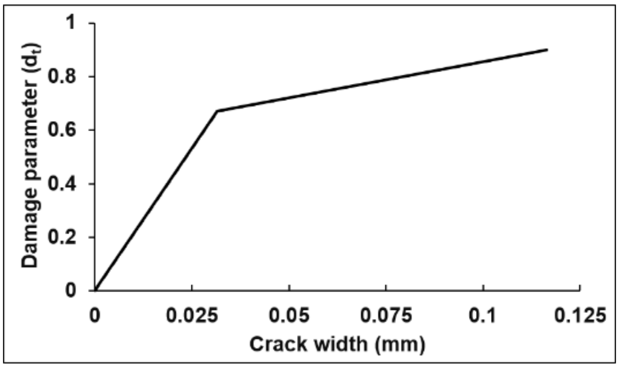

(d)

Figure 3.5 Uniaxial response of concrete utilized in CDP model (a), (b) compressive parameters (c), (d) tensile parameters

Since, low velocity impact problems are associated with development of high strain rates which eventually result in magnification of mechanical properties. Hence, in this work, the effects of strain rate are accounted using mathematical models of DIF reported in CEB-FIP [136] model code. A strain rate of 10 s^{-1} is considered which satisfies the defined low velocity impact range [47, 161]. Also, since the ratio of fracture energy to the tensile strength of concrete remains constant for strain rates less than 80 s^{-1} [162], the crack width is same for both the strain rates.

3.3.3 Mesh convergence

The mesh convergence study is performed to ensure the methodology used for modelling the low velocity impact response of concrete is stable and accurate. It is necessary to adapt an optimum mesh size such that accurate FE results are obtained in optimum computational time. The convergence study is carried out by analyzing the influence of mesh size on the peak impact force. In this work, the beam is meshed using cubic elements with unit aspect ratio, as the use of aspect ratios larger than one often result in mesh sensitivity [35]. The influence of mesh size is observed and the obtained results are compared with the actual values acquired from the experimental investigations. The beam is meshed using explicit hex dominated C3D8R elements with enhanced hourglass stiffness control to minimize the zero stress nonphysical deformation modes. Previous investigations have reported that the use of first order elements (for example C3D8) do not experience shear and volumetric locking [163]. However, the use of linear elements in accordance with the reduced integration method (such as C3D8R) lead to formation of nonphysical zero energy/stress modes (hourglass problem) which results in extreme mesh distortions with no resisting stresses [35]. Thus, in order to solve this problem, hourglass stiffness control is utilized which imparts artificial stiffness to the elements such that the analysis could be performed accurately.

A total number of five different seed sizes of 20 mm, 10 mm, 5 mm, 2.5 mm, and 2 mm consisting of 625, 5000, 40000, 320000, and 625000 elements, respectively are checked for investigating the convergence of solution. For each mesh size, the FE analysis is performed and the peak impact force values are compared with the experimental results. The results of convergence study are displayed in Figure 3.6. For a better representation, results are normalized with respect to finest mesh size of 2 mm. It is observed that the refinement of mesh size results in convergence towards a particular value. The correct prediction of peak impact force is obtained for mesh size of 2.5 mm. Based on the convergence study, a mesh size of 2.5 mm is found to be appropriate for producing stable and accurate solutions as the difference of results between mesh sizes of 2.5 mm and 2 mm is negligible. The selected mesh size and enhanced hourglass stiffness technique are further validated using principle of energy balance. In order to get a stable solution in ABAQUS/EXPLICIT, the following conditions should be satisfied: first, the fluctuation in total energy should not be more than 1% throughout the complete analysis, second, the artificial hourglass energy developed should be minimum [47]. The energy time histories for coarse meshing of 20 mm and the adapted meshing of 2.5 mm are presented in Figure 3.7.

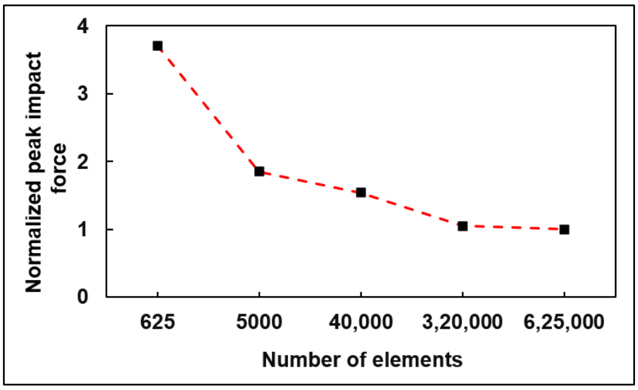

Figure 3.6 Mesh convergence study for different size of elements

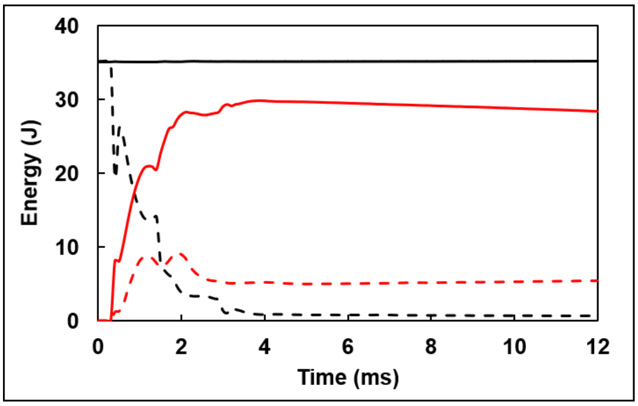

(a)

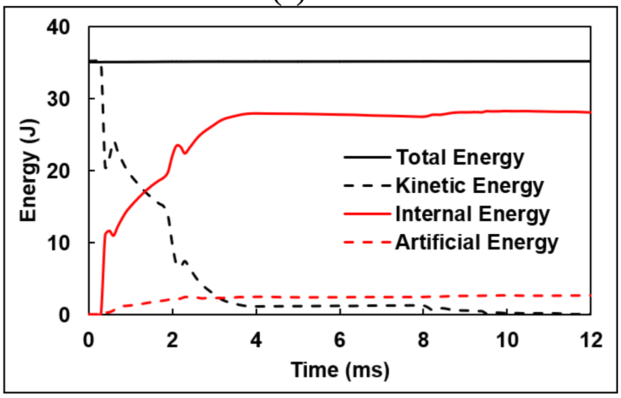

(b)

Figure 3.7 Energy-time histories (a) 20 mm mesh (b) 2.5 mm mesh

From the energy time history analysis, it can be observed that for both mesh sizes, the variation in total energy is less than 1% throughout the analysis. However, for coarser meshing (See Figure 3.7(a)), the artificial energy is found to exceed 40 % of internal energy, which represents excessive mesh distortions and hence considered to be unacceptable. On the other hand, the use of 2.5 mm mesh size produces lower values of artificial energy (see Figure 3.7 (b)) and satisfies the energy balance criteria. Hence, the selected mesh size (2.5 mm) and the enhanced hourglass stiffness technique are validated.

3.4 Experimental studies

The objective of the experimental programme is to determine the influence of compressive strength and reinforcement on the low velocity impact response of concrete beams. In addition to this, the results from experimental studies are also utilized to validate the FE model and establish the default values of CDP parameters which reflect the actual response of system. The validated model is then used for carrying out the parametric investigations.

For the plain concrete beams, three concrete mixes of characteristic compressive strength 50 MPa, 40 MPa, and 30 MPa are designed as per IS 10262-2019 [164]. While, the Reinforced Concrete (RC) beams are provided with two Fe500 grade longitudinal steel bars. The influence of reinforcement ratio is studied by varying the diameter of steel bars (8 to 16 mm). The other parameters for the design mix are as follows: OPC 43 grade cement, 0.36 water cement ratio, Zone II sand, and coarse aggregates with nominal maximum size of 20 mm. The specific gravity and normal consistency of cement is 3.038 and 29 percent respectively. The water absorption of fine and coarse aggregates is found to be 3 percent and 0.85 percent, respectively. While, their density is 2645 kg/m^3, and 2831 kg/m^3, respectively. The desired workability of fresh concrete is achieved by using liquid Masterpolyheed 8385 superplasticizer procured from BASF. The mix design adopted for three different grades of concrete is shown in Table *3.3*. The slump values of the concrete are obtained in the range of 75 - 110 mm as per IS 1199-1959(R 2018: Part 2) [165].

The low velocity impact tests are performed utilizing an instrumented drop impact test setup as per ACI 544.2R-89 [166]. The actual test setup is shown in Figure 3.8(a). For a better representation of various components, the schematic of drop impact test setup is also presented which is shown in Figure 3.9. The impact testing setup comprises of a flat nose impactor of mass 6 kg which can be dropped from variable heights (100 – 1400 mm). The concrete beam specimens have a length of 500 mm and cross-section of 100 mm × 100 mm. The specimens are placed over cylindrical supports such that the supported span is 400 mm with 50 mm overhangs on each side (Please see: Figure 3.8(b)). During the tests, the impact force time history is recorded using dynamic load cell provided at the top of impactor (See Figure 3.8(c)). While, the mid-point displacement of concrete beam specimen is recorded using Linear

Variable Differential Transformer (LVDT) provided below the mid-point of bottom surface of the specimen. The additional instrumentations include velocity sensors and data acquisition system. The output from load cell, and LVDT, is recorded at 0.11 millisecond intervals.

Table 3.3 Mix proportion of various components for 1 m^3 of concrete

Concrete Mix	Cement (kg)	Water (kg)	Aggregate		Super-plasticizer (kg)	w/c ratio
			Fine Aggregate (kg)	Coarse Aggregate (kg)		
M50	442	160.25	635	1281	1.65	0.36
M40	431	158	786	1115	1.32	0.36
M30	418	160	790	1120	1.25	0.36

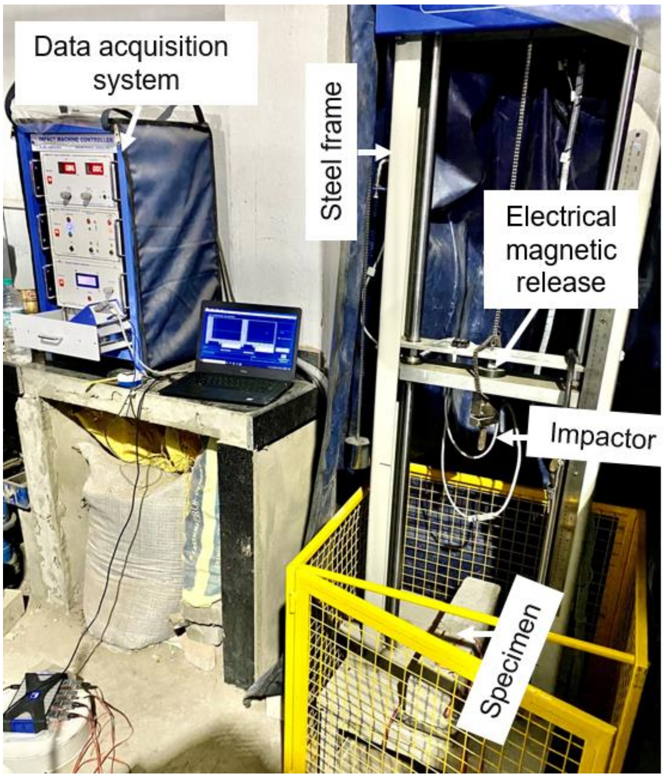

(a)

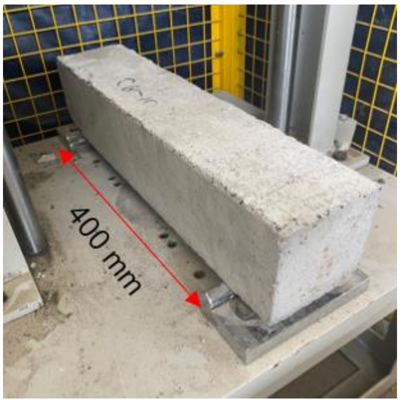

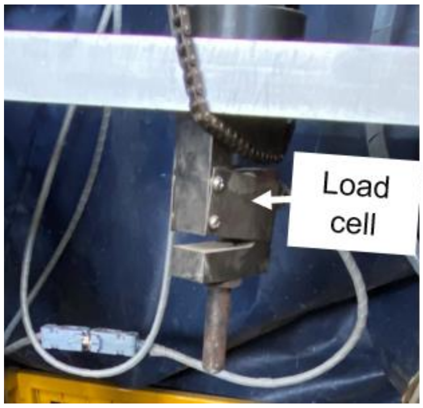

(b) (c)

Figure 3.8 (a) Drop impact test setup (b) Supported span of specimen (c) Load cell and impactor

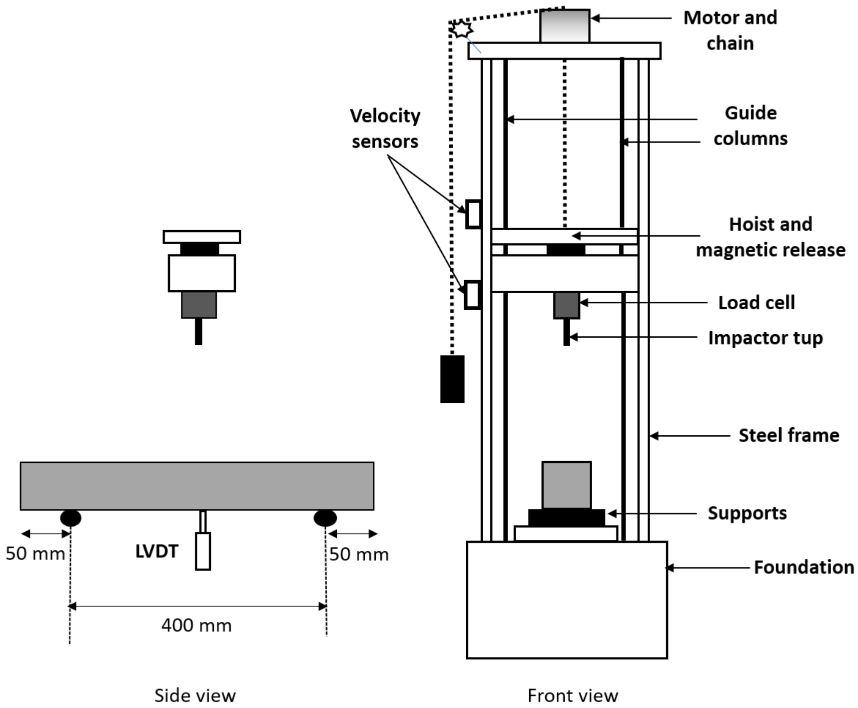

Figure 3.9 Schematic of the drop impact test setup

A total of 12 beam specimens for drop impact test, 18 cube specimens (100 mm size) for compressive strength test, and 18 cube specimens (150 mm size) for split tensile strength test are casted and retained for wet curing after a period of 24 hours at a temperature of 25 – 30 º C.

3.5 Experimental results and validation of Finite Element model

The concrete cubes are tested under uniaxial compression at a strain rate of 2.2×10^{-5} s^{-1} and the 28-day compressive stress-strain curves are obtained as shown in Figure 3.10. Also, the 28-day split tensile strength of M50, M40, and M30 grade concrete are found to be 3.33 MPa, 2.82 MPa, and 2.26 MPa, respectively. Further the low velocity impact tests are performed on plain and reinforced concrete beam specimens and their results are presented in subsequent subsections.

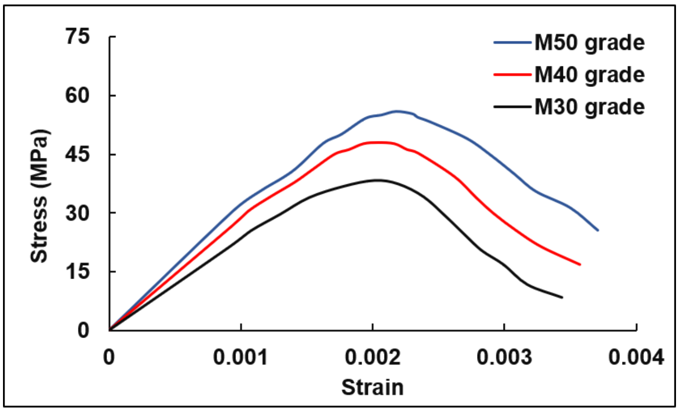

Figure 3.10 Stress-strain curves for different grades of concrete

3.5.1 Plain concrete beams

The plain concrete beams are impacted by 6 kg drop weight freefalling from 500 mm height. For each grade of concrete, three specimens are tested and the response of beam is recorded in terms of: impact force time histories, and impact force vs mid-point displacement curves as displayed in Figure 3.11. The results obtained from FE investigations are also plotted in order to have a better comparison. Additionally, the validation of FE model is done using the experimental results and the default values of CDP model parameters are established. The damage contours for different grades of concrete beam obtained from experimental and numerical investigations are shown in Figure 3.12.

In the experimental investigations, when the drop weight comes in contact with the concrete beam, the inertial resistance offered by the beam results in a sudden rise in the impact force values. The impact force then attains a peak value when the concrete beam is completely damaged. However, after complete damage, the concrete beam undergoes post peak reduction in the impact force values. However, in numerical investigations due to absence of the actual inertial resistance of the concrete material, resistant forces are developed after a time lag due to which the delayed response of impact force time histories is obtained.

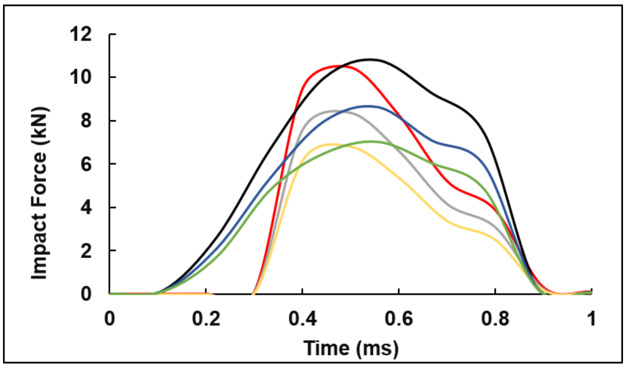

(a)

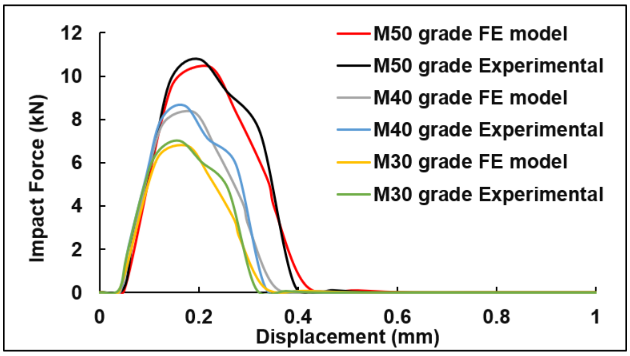

(b)

Figure 3.11 (a) Impact force vs time (b) Impact force vs displacement for plain concrete beams

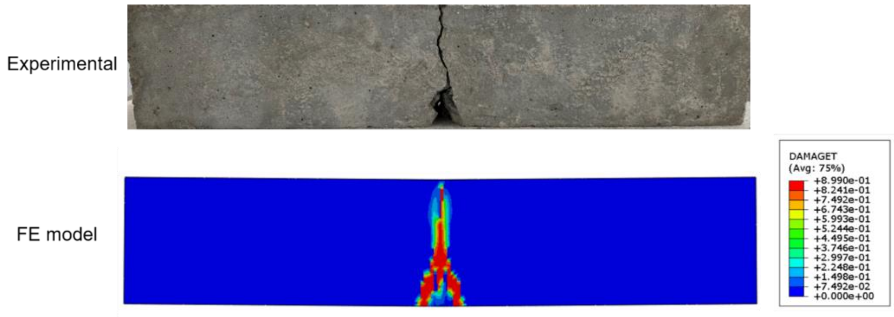

(a)

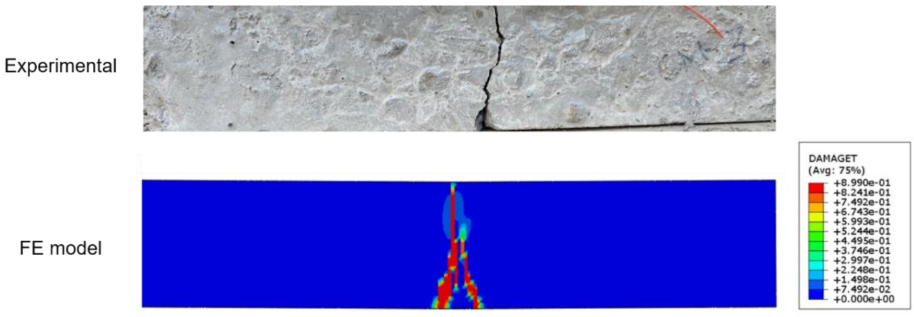

(b)

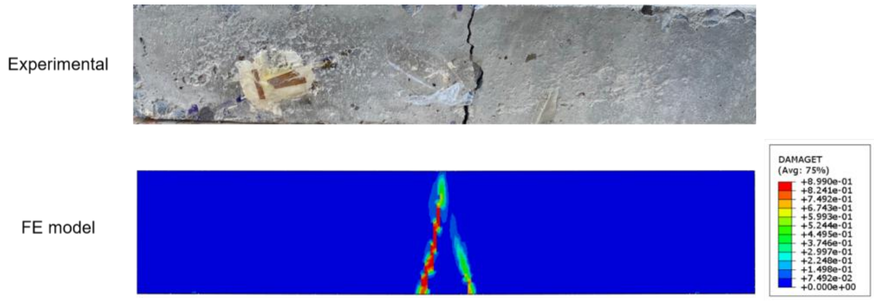

(c)

Figure 3.12 Damage contour of plain concrete beams Experimental and Numerical study (a) M30 grade (b) M40 grade (c) M50 grade

The use of higher grade of concrete offers increased resistance against external loading due to its dense nature and higher internal bond strength. Hence, the reaction forces developed inside the beam are higher and consequently increased impact force values are obtained for the same drop height. Additionally, the response of different grades of concrete are also compared in terms of energy absorption capacity which is determined as the area under the impact force-displacement curve. The values of energy absorption capacity are shown in Table 3.4. It is evident that the use of high strength concrete enhances the energy absorption capacity of beams under low velocity impact loading.

From Figure 3.12, it can be noticed that the plain concrete beams undergo failure under flexural mode. The flexural cracks originate from the extreme bottom fibre of concrete beam and propagate vertically upward towards the zone of impact. The use of higher grade of concrete results in reduced damage under low velocity impact. Also, the flexural failure of concrete beams obtained from the experimental investigations are accurately predicted by the FE simulations. The damage of concrete beam is quantified by measuring the horizontal width of crack at the mid-section of front face as explained in Figure 3.13. In the experimental investigations, the crack width is measured using digital imaging. The values of crack width obtained from experimental and FE investigations are shown in Table 3.5. It can be observed that for M30 grade concrete, slightly higher impact force values are obtained in the experimental studies. Hence the M30 grade concrete modelled using FE method offers slightly lower resistance to the drop weight. Also, the displacement values are higher in the FE model, thus concluding that the concrete beam modelled using FE method has slightly weaker impact resistance as compared to that of experimental model. Thus, the M30 grade concrete modelled using FE method shows 20% higher crack width values. Also, The use of higher grade of concrete produces lesser crack width due to reduced damage and higher internal bond strength of concrete. It can be observed that the FE model accurately depicts the impact force vs displacement curves as well as the damage contours. Also, the peak impact impact force values are predicted with a minimal error. Hence, it is concluded that the results obtained from FE simulations are in good correlation with the experimental results. Thus, the numerical simulation approach adopted in the current study is validated and found to be suitable for carrying out the parametric investigations.

Table 3.4 Energy absorption capacity for different grades of concrete

Grade of Concrete	Energy absorption capacity (N-m)
M30	1.84
M40	2.1
M50	3.5

Table 3.5 Values of crack width obtained at mid-section of beam

Grade of Concrete	Experimental (mm)	Numerical (mm)
M30	1.82	2.21
M40	1.663	1.71
M50	1.3635	1.267

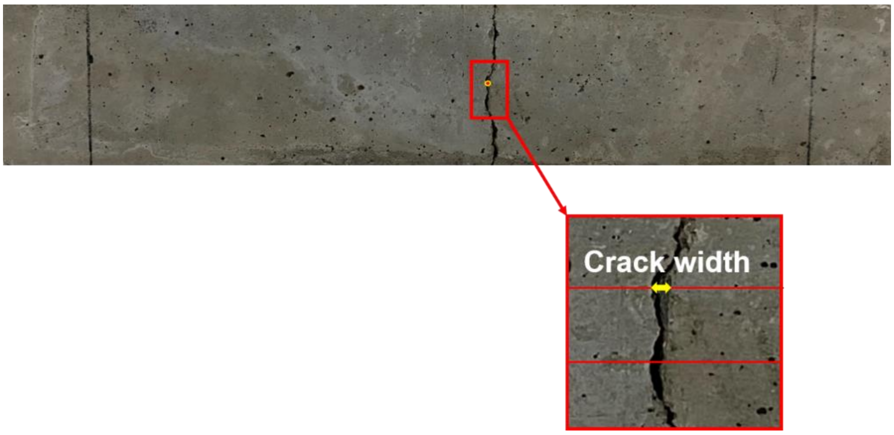

Figure 3.13 Measurement of crack width at front face of concrete beam

3.5.2 Reinforced concrete beams

The RC beams are impacted by 6 kg drop weight freefalling from 1.2 m height. A total number of three specimens are tested. Each specimen had two 12 mm diameter steel bars (reinforcement ratio of 2.26 percent). The main objective is to determine the influence of longitudinal reinforcement on the response and failure pattern of the concrete beams against low velocity impact loading. The beam response is quantified in terms of: impact force time histories, and impact force vs mid-point displacement.

The FE model for RC beams is validated using the experimental results which is subsequently utilized for investigating the effects of reinforcement ratio (RR). In the FE investigations, three different reinforcement ratios are considered: 1 percent, 2.26 percent, and 4 percent. The response as well as the damage contour of concrete beam obtained from experimental and FE investigations are plotted in Figure 3.14 and Figure 3.15 respectively.

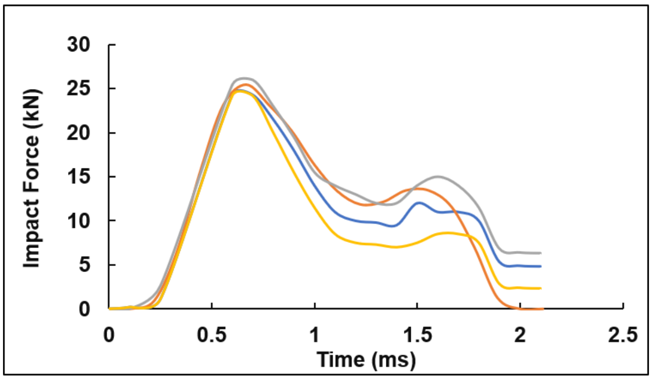

(a)

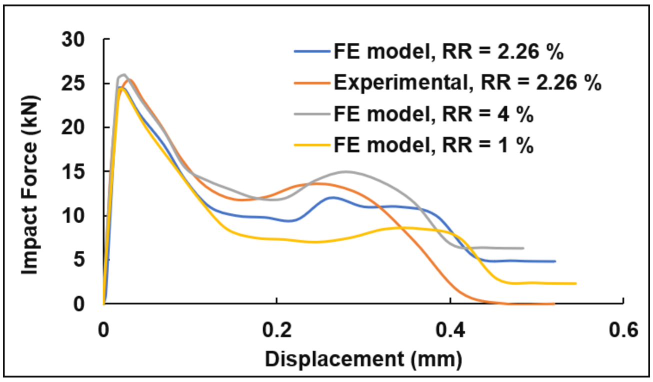

(b)

Figure 3.14 (a) Impact force vs time (b) Impact force vs displacement for RC beams

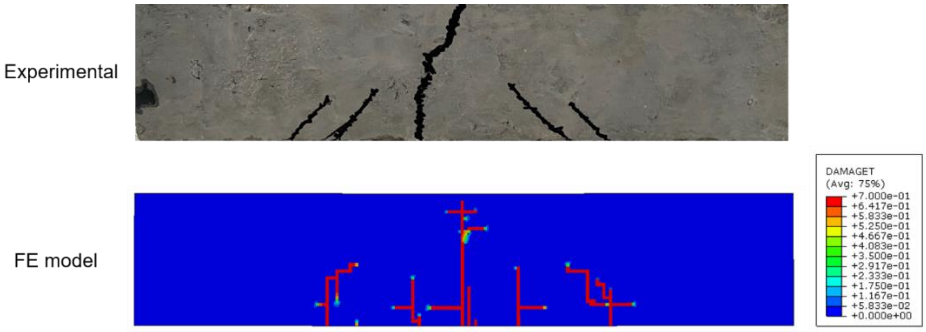

Figure 3.15 Damage contour of RC beams obtained from experimental and FE analysis

The RC beams undergo an overall flexural failure with higher impact force values compared to plain concrete beams. The origination of minor flexural cracks is observed near the bottom portion of RC beam in both the experimental as well as FE investigations. At the sections away from mid-span, the cracks are inclined towards the point of load application. The provision of reinforcement prevents localized failure and dissipates the impact energy throughout the concrete beam due to which the performance of RC beams is superior as compared to that of plain concrete beams. Also, the RC beams suffer much lesser damage compared to plain concrete beams, although the imparted energy is much higher in case of RC beams. The energy absorption capacity for RC beams with different reinforcement ratios is presented in Table 3.6. The increase in reinforcement ratio enhances the impact energy absorption capacity of RC beams. From this analysis, it is concluded that the provision of longitudinal reinforcement results in an improved performance of concrete beam under low velocity impact.

Table 3.6 Energy absorption capacity for different reinforcement ratios

Reinforcement ratio, RR (%)	Energy absorption capacity (N-m)
1	4.126
2.26	4.367
4	4.839

3.6 Results of parametric studies on Concrete Damaged Plasticity (CDP) model parameters

The low velocity impact response of a concrete beam is directly related to the parameters of CDP model. Hence, a parametric investigation has been carried out in order to search for a desirable set of parameters. This objective is achieved by varying the CDP parameters over a range of possible values. The various parameters of CDP model considered in the present study include: dilation angle (ψ), deviatoric plane shape parameter (K_c), ratio of compressive strength in biaxial state to uniaxial state (σ_{bo}/σ_{co}), flow potential eccentricity (ε), fracture energy (G_f), and compressive stress-strain characteristics of concrete.

3.6.1 Dilation angle

The dilation angle (ψ) is the angle at which yield/failure surface is inclined with respect to hydrostatic axis in meridional plane. In physical terms, this parameter governs the evolution of volumetric strain in case of plastic shearing. Hence, it may also be termed as the ratio of volumetric to shear strain. For traditional concrete, its value ranges from 20 to 45 degree [85, 157, 167]. In this work, the value of dilation angle is varied from 20 to 45 degree at 5 degree intervals, and the parametric investigation is performed taking default values of other parameters. The effects of variation of dilation angle on the response of concrete beam is displayed in Figure 3.16. The impact force time history of the concrete beam which represents the force imparted by the impactor on beam specimen is shown in Figure 3.16(a). While, Figure 3.16(b) represents the impact force vs displacement response of concrete beam which is subsequently used for determining the energy absorption capacity.

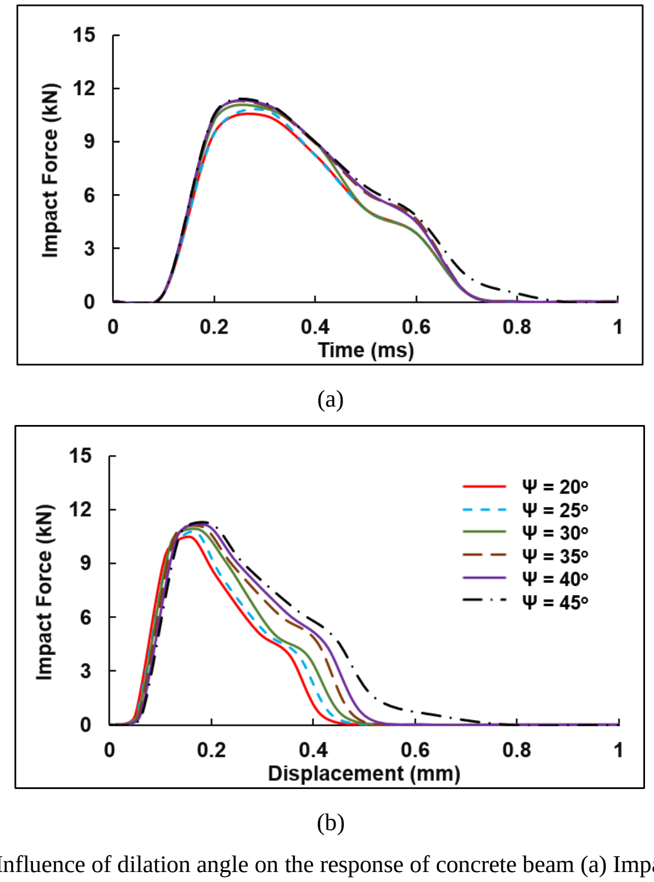

Figure 3.16 Influence of dilation angle on the response of concrete beam (a) Impact force time history and (b) Impact force vs displacement

The response of concrete beam against low velocity impact is considerably affected by the variation in dilation angle. The increase in dilation angle results in a slight increment in the impact force values while, there is a significant enhancement in the ductility. In other words, the use of higher dilation angle enhances the deformation capability which eventually results in higher energy dissipation. The energy absorption capacity (area under impact force vs displacement curves) of concrete beam for different values of dilation angle is shown in Table 3.7. The increase in dilation angle improves the impact energy absorption capacity of concrete beam, which reflects superior performance under impact loading. Thus, a higher value of dilation angle (say 45º) is suitable as it improves the energy absorption capacity by approximately 33%. It can also be concluded that the enhancement in flexibility of concrete improves the response under low velocity impact. In practice, this result can be used to design a relatively flexible concrete mix by improvising the use of different type of fibers or plastic waste.

Table 3.7 Energy absorption capacity of concrete beam at various dilation angles

Dilation angle, ψ	Energy absorption (N-m)
20º	2.266
25º	2.398
30º	2.613
35º	2.89
40º	3.014
45º	3.6

3.6.2 Deviatoric plane shape parameter

Shape parameter (K_c) governs the profile of yield surface in deviatoric plane. This parameter is used to modify the yield surface in order to consider different values of tri-axial tensile and compressive yield stresses. In physical terms, this parameter is the ratio of second stress invariant in tension to that in compression for the same value of confining pressure. For the yield surface to have a convex shape, K_c should lie between 0.5 and 1. In this work, three different values of shape parameter (0.5, 0.67, 1), have been studied and their effect on the impact response is displayed in Figure 3.17.

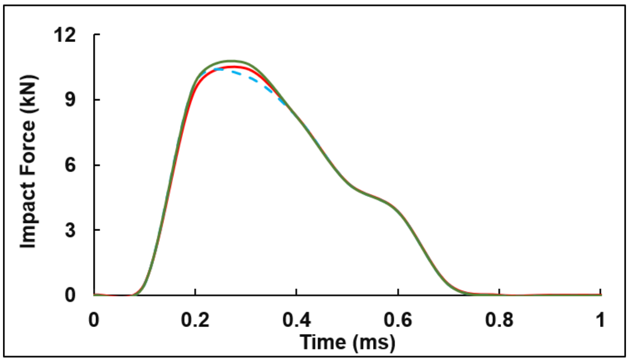

(a)

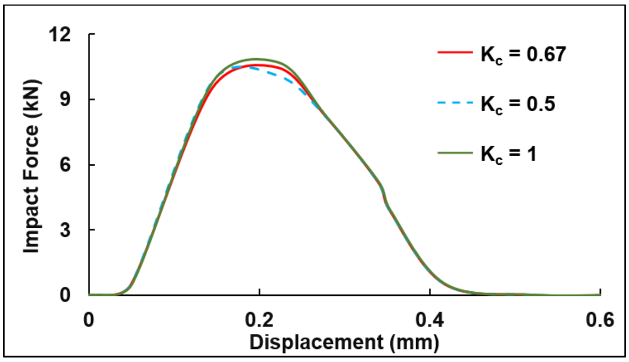

(b)

Figure 3.17 Influence of shape parameter (K_c) on response of concrete beam (a) impact force vs time (b) Impact force vs displacement

The variation in shape parameter (K_c) has negligible influence on the impact force time histories, as well as the impact force vs displacement curves. Consequently, the energy absorption capability of concrete beams also remains unaffected. Hence, it is concluded that K_c has no significant influence on the low velocity impact response of concrete beam. Since, in the present case of loading, damage is mainly induced due to tension resulting from bending in the concrete beam. However, the shape parameter K_c takes effect only under triaxial compression. Thus, no variations are observed in the response of concrete beam. Hence, the default value of K_c=0.67 is selected as the recommended value of shape parameter.

3.6.3 Flow potential eccentricity

Eccentricity parameter (ε) is the rate at which flow potential advances asymptote. When compressive loading is applied to concrete under low confining pressure, the volume expansion is high. In order to consider the high values of volume expansion, flow potential eccentricity (ε) is used to increase the value of dilation angle such that the actual response of concrete is captured by the model. Its value may be taken as the ratio of tensile to compressive strength of concrete [158]. In this work, five different values of ε (0, 0.05, 0.1, 0.25, and 0.5) have been considered. The effects of variation of ε on the low velocity impact response of concrete beam is shown in Figure 3.18.

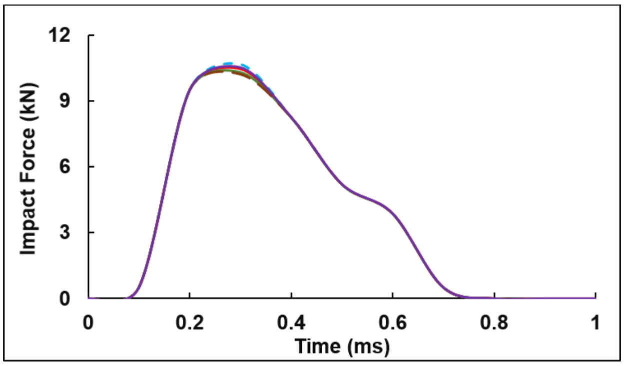

(a)

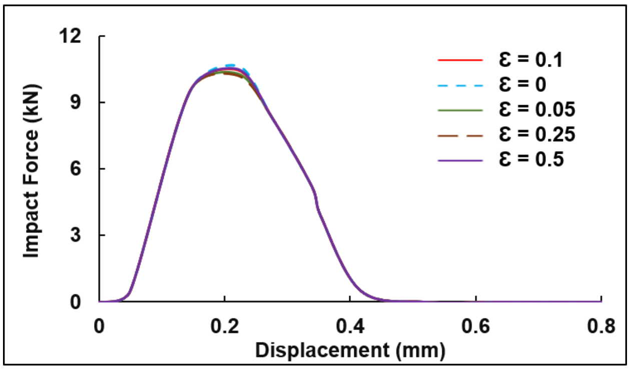

(b)

Figure 3.18 Influence of flow potential eccentricity (ε) on response of concrete beam (a) impact force vs time (b) impact force vs displacement

The flow potential eccentricity (ε) has negligible effect on the impact force time histories and the impact force vs displacement curves of the concrete beam. Eventually, this results in no variations in the energy absorption capability. Thus, it is concluded that the influence of flow potential eccentricity (ε) on the low velocity impact response of concrete beam is insignificant. This, response is expected since the eccentricity parameter specifies change in volume at low confining pressures, and impact problems mostly involve stress state at high confining pressures. Also, the damage initiation follows immediately after yielding of concrete in tension. However, the eccentricity parameter is only predominant in the flow potential, which eventually results in an insignificant influence on the low velocity impact response of beam. Therefore, the default value of eccentricity parameter i.e., ε = 0.1 is selected as the recommended value.

3.6.4 Ratio of biaxial to uniaxial yield strength

Strength ratio parameter is the ratio of initial biaxial to the initial uniaxial yield stress in compression (i.e., σ_{bo}/σ_{co}). When concrete is subjected to equal biaxial compression, its strength may be around 16% higher as compared to its uniaxial strength due to the effect of poisson's ratio [167]. Thus, this parameter represents the yield strength of concrete under biaxial state of loading. Its value may range from 1.1 to 1.2 [85]. In this work, six different values of σ_{bo}/σ_{co} (1.1, 1.12, 1.14, 1.16, 1.18, 1.2) are considered, along with the default values of other parameters. The effects of variation of σ_{bo}/σ_{co} on the response of concrete beam is displayed in Figure 3.19.

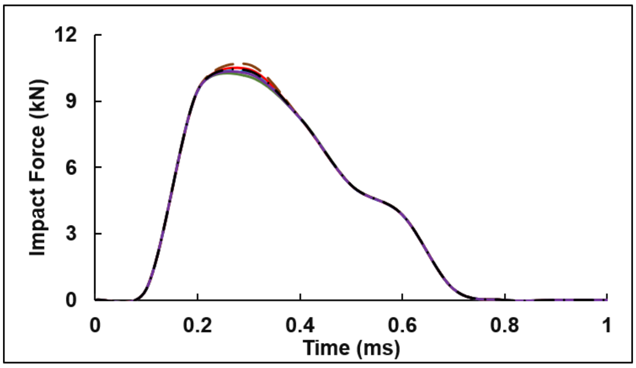

(a)

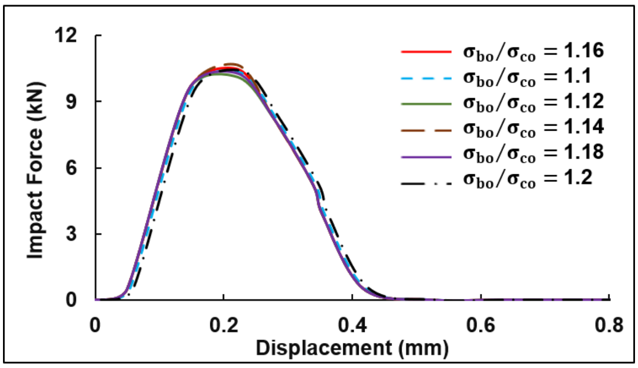

(b)

Figure 3.19 Influence of strength ratio parameter on the response of concrete beam (a) impact force vs time (b) impact force vs displacement

The variation in strength ratio (σ_{bo}/σ_{co}) has negligible influence on the on the low velocity impact response of concrete beams. In such loading cases, the damage is mainly induced in concrete due to tensile bending. However, the strength ratio parameter is associated with the response of concrete under biaxial and uniaxial compressive loads. Hence no influence of this parameter is observed and the default value (σ_{bo}/σ_{co}=1.16) is considered as the recommended value.

3.6.5 Fracture energy

Fracture energy (G_f) may be defined as the energy needed to generate a unit area of cracked surface in tension. For plain and fiber reinforced concrete, it may be calculated as the area under stress-crack width displacement curve in the post-peak response of concrete under uniaxial tension. In this work, five different values of fracture energy (100 N/m, 112 N/m, 200 N/m, 300 N/m, 325 N/m) are considered. The value of fracture energy is varied by changing the crack width while keeping tensile strength to be constant. The different cases of fracture energy considered in this study are shown in Figure 3.20, and their influence on the response of beam is shown in Figure 3.21.

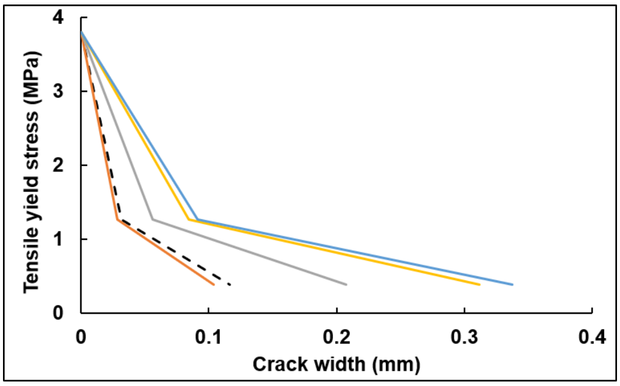

(a)

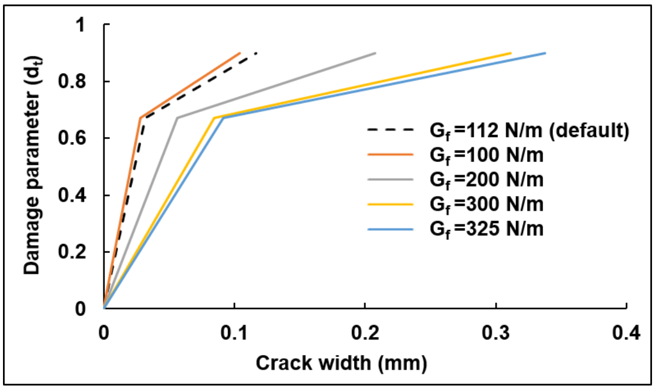

(b)

Figure 3.20 Different cases of fracture energy considered in this study (a) tensile yield stress vs crack width (b) damage parameter vs crack width

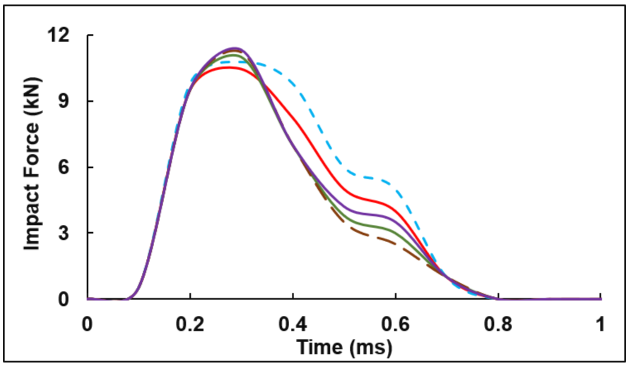

(a)

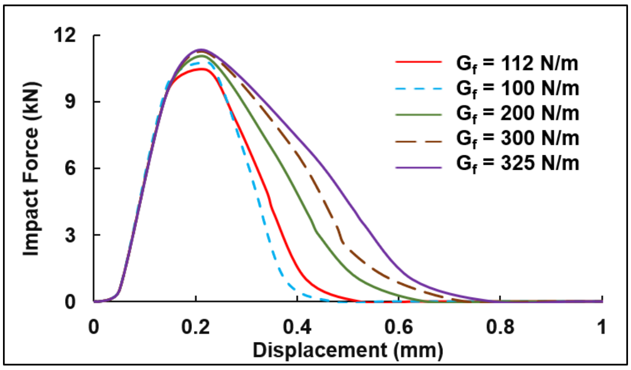

(b)

Figure 3.21 Influence of fracture energy on the response of concrete beam (a) impact force vs time (b) impact force vs displacement

The low velocity impact response of concrete beam is found to be considerably affected by the variation in fracture energy. The increase in fracture energy results in a slight increment in the impact force values, while the ductility is significantly improved. The enhanced ductility eventually results in higher impact energy absorption capacity of concrete beams (See Table 3.8) and improved performance under low velocity impact. Thus, in this work a value of G_f= 325 N/m is considered as the recommended value as it enhances the energy absorption capacity of concrete beam by approximately 42% as compared to the default value of fracture energy. Although, a further increase in fracture energy would improve the performance of concrete, this study helps in comprehending the improved response of concrete which is obtained due to a certain increase in the fracture energy properties.

Table 3.8 Energy absorption capacity of concrete beams at different values of fracture energy

Fracture energy, G_f (N/m)	Energy absorption (N-m)
100	3.35
112	3.5
200	3.8
300	4.15
325	4.79

3.6.6 Uniaxial stress-strain behavior in compression

The compressive stress-strain curve reflects the response of concrete under uniaxial compressive loading. In this work, the influence of different compressive stress-strain models on the low velocity impact response of concrete beams is analysed. A total of six different models are considered. Among these models, the first three account for the effect of descending slope of stress-strain curve while keeping the strain values to be constant (Model M1, M2, M3)). In the remaining models, the strain values are varied while keeping the stresses to be constant (Model N1, N2, N3). The different stress-strain models are shown in Figure 3.22, and the influence of utilization of these models on the impact response of concrete beam is shown in Figure 3.23. Since, the strain values in the Models M1, M2, and M3 are kept constant, the damage parameter curves remain the same for these models.

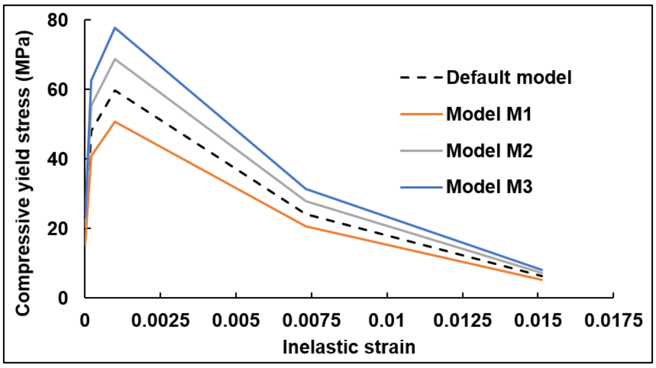

(a)

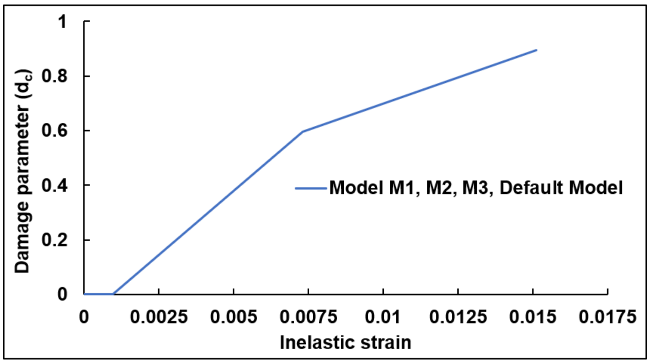

(b)

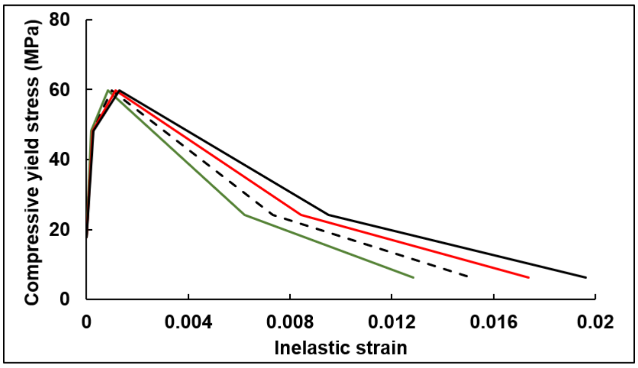

(c)

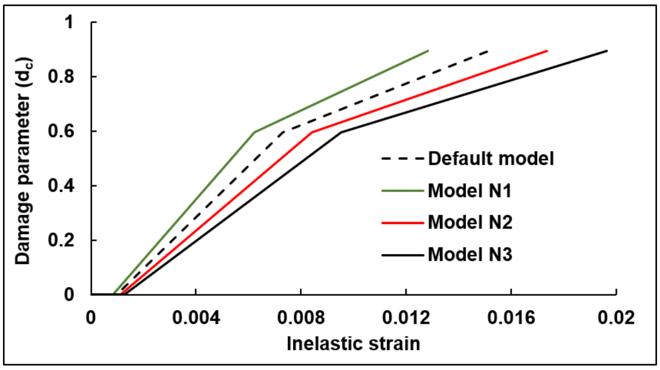

(d)

Figure 3.22 Different cases of uniaxial compression (a), (b) Model M1, M2, M3, (c), (d) Model N1, N2, N3

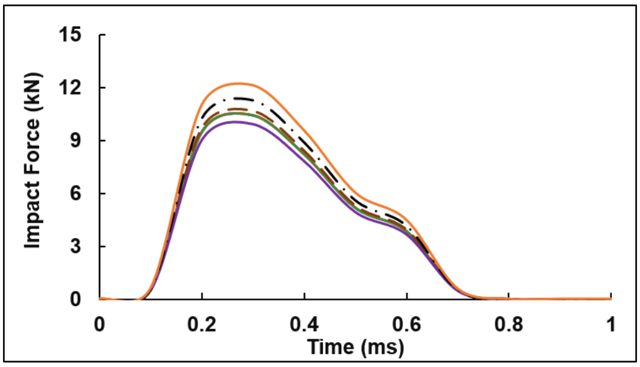

(a)

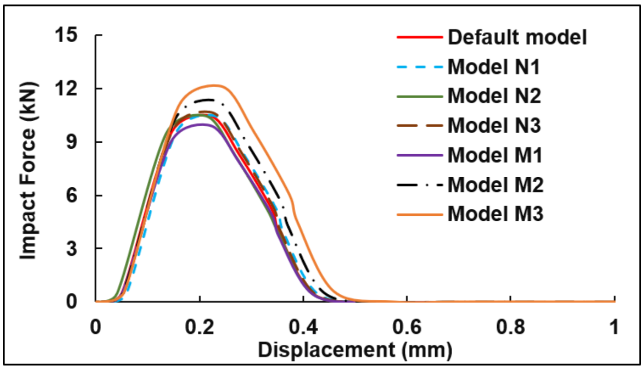

(b)

Figure 3.23 Influence of compressive stress-strain relationship (a) impact force vs time (b) impact force vs displacement

The use of Models N1, N2, and N3 with variations in strain values do not affect the impact force time histories and the impact force vs displacement curves of the concrete beam. Consequently, the influence on energy absorption capacity of beam is also negligible. Hence, it is concluded that the Models N1, N2, and N3 have insignificant influence on the response of concrete beam. However, the Models M2, and M3 produce considerable enhancement in the impact force, and displacement values of the concrete beams. Thus, the use of Models M2, and M3 eventually improve the energy absorption capability. This is observed due to higher compressive strength of concrete, which offers an increased resistance to the applied loading. The energy absorption capacity of concrete beam utilizing different stress strain models is presented in Table 3.9. The concrete beam utilizing Model M3 dissipates the highest amount of energy (27.6 % higher compared to default model). Hence, Model M3 is considered as the recommended model for improving the response of concrete beam under low velocity impact loading.

Table 3.9 Energy absorption capacity of concrete beams for different compressive stress strain models

Compressive stress-strain model	Energy absorption (N-m)
Default model	3.5
Model M1	3.68
Model M2	3.744
Model M3	4.084
Model N1	3.617
Model N2	3.622
Model N3	3.766

3.7 Beam response utilizing recommended CDP parameters

In order to check the performance of concrete with recommended CDP parameters (as obtained in the previous subsection), a FE analysis has been carried out. The comparison of the response of concrete beam utilizing recommended and default values of the CDP model parameters is shown in Figure 3.24. The damage pattern of concrete beam with recommended parameters represented as color map of DAMAGET is shown in Figure 3.25.

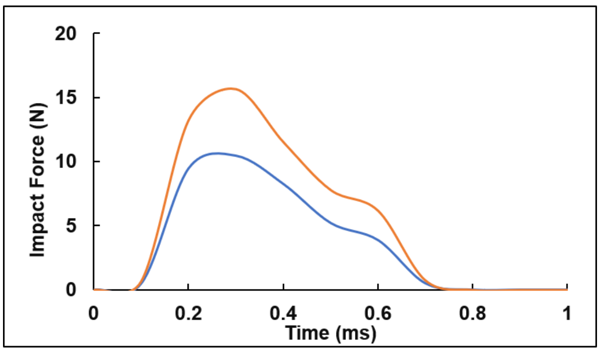

(a)

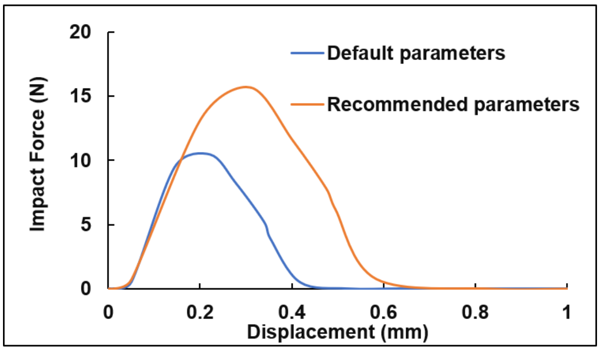

(b)

Figure 3.24 Response of concrete beams with default and recommended parameters (a) impact force vs time (b) impact force vs displacement

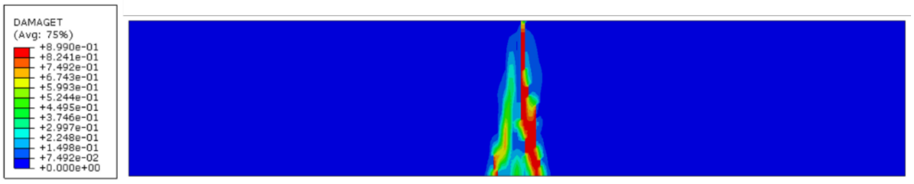

Figure 3.25 Damage contour of concrete beam with recommended material configuration for present loading condition

The use of recommended parameters results in superior performance of concrete beam under low velocity impact. The ductility as well as peak impact force values of the concrete beam are enhanced, which eventually results in an increased energy absorption capacity (~112 % increment). The improved performance of concrete beam can also be observed from the damage contour. The beam with recommended parameters suffers lesser damage as compared to default concrete beams. It is thus concluded, that the use of recommended parameters effectively reduces the damage and cracking of concrete beam and results in an improved response under low velocity impact.

3.8 Summary

This work takes an important step towards understanding the importance of various governing parameters which could be used for designing a concrete mix with impact resistant properties. This objective is achieved by carrying out a parametric investigation in ABAQUS/EXPLICIT. A 3D-FE model of the concrete beam is developed which is impacted by 6 kg drop weight from a height of 500 mm. The experimental investigations are performed to validate the FE model as well as to establish the default values of CDP model parameters. In the parametric studies, the values of CDP model parameters are varied over a broad range and their influence on the response of concrete beam is investigated. Finally, a set of values are recommended which can be utilized to improve the response of concrete under impact loading. Additionally, the influence of compressive strength of concrete and the provision of longitudinal reinforcement are also examined.

The recommended values of CDP parameters for plain concrete beam against low velocity impact loading are determined as: dilation angle (ψ)= 45º, fracture energy (G_f)= 325 N/m, and Model M3 for uniaxial compressive stress-strain response. It is concluded that the dilation angle (ψ), fracture energy (G_f), and uniaxial compressive stress-strain response inputs in CDP model can be considered as predominant parameters influencing the response of plain concrete beams against low velocity impact. Also, it is found that the shape parameter (K_c), ratio of biaxial to uniaxial yield strength (σ_{bo}/σ_{co}), and flow potential eccentricity (ε) can be considered insignificant in the 3D nonlinear FE analysis of concrete beams against low velocity impact.

The results obtained from 3D-FE analysis show that the use of recommended material parameters improve the energy absorption capacity by 112.62% with reduced damage and cracking of concrete beam. However, it must be noted that these material parameters are hypothetical and might not exist. The use of higher grade of concrete results in an improved performance with reduced damage and higher energy absorption capacity under low velocity impact. Also, the provision of reinforcement in concrete results in globalization of overall damage which eventually causes reduced cracking and higher impact energy absorption in comparison to plain concrete beams.

Chapter-4

Influence of crumb rubber as partial sand replacement on the low velocity impact response of concrete

4.1 Introduction

Concrete structures are susceptible to low velocity impact loading resulting from several unprecedented events. Thus, the concrete used for such applications should have relatively high energy absorption capacity, ductility, fracture toughness, and impact resistance [168]. Till date, several studies have explored the possibilities and advantages of using crumb rubber in concrete [38, 56–62] In general, crumb rubber has been found to enhance the ductility and energy absorption capacity, while reducing the compressive strength. Furthermore, the use of crumb rubber in concrete provides several environmental benefits. It reduces the demand for mineral aggregates, and offers an alternative method of disposing off worn-out tires [150]. Hence, crumb rubber may be considered a valuable additive for enhancing the impact resistance of concrete.

In the past, only a few studies have investigated the low velocity impact response of rubberized concrete [38, 57, 60]. Taha et al. [57] utilized chipped and crumb rubber as partial aggregate replacement in concrete and observed an improvement in the impact resistance and energy absorption capacity. Atahan and Yucel [60] utilized coarse and fine crumb rubber in cylindrical concrete specimens and observed similar results. However, these studies utilized simplified test setups which did not record the impact force, displacement time histories, and fracture energy values and only captured the response at a material level. Thus, the detailed structural response of concrete structural elements was not covered in these studies and are still lacking in literatures. The only available literatures in this area include the study performed by Al-Tayeb et al. [38]. However, the design guidelines for using crumb rubber in concrete are not available in literatures.

In this work, detailed experimental investigations are performed to analyze the influence of crumb rubber as partial sand replacement on the low velocity impact response of concrete beams. The results obtained from experimental investigations are compared with those of 3D-FE simulations and analytical method. The main contributions of this work are the followings: first, the influence of crumb rubber on the response of concrete beams against low velocity impact has been studied by conducting detailed experimental investigations; second, the macroscopic low velocity impact response of rubberized concrete is linked with the microscopic properties; third, an analytical and a 3D-FE model has been developed for investigating the low velocity impact behavior of plain and rubberized concrete beams and finally, design guidelines have been proposed for the selection of optimum rubber content in concrete.

The proposed approach used for this work is shown in Figure 4.1. Initially, several concrete mixes are prepared by varying the proportion of crumb rubber as sand replacement. The concrete mix specimens are tested using a low velocity impact test setup. The response of concrete beams is assessed in terms of energy absorption capacity, which is the area under load vs displacement curve. The cause of variation in the response of rubberized concrete at a macroscopic level is also assessed by performing microstructural analysis. Finally, the results of quasi-static tests and energy absorption capacity are used to develop a design guideline chart. This chart could be used to select an optimum rubber content in concrete such that a desired minimum compressive strength is achieved with the enhancement in energy absorption capacity.

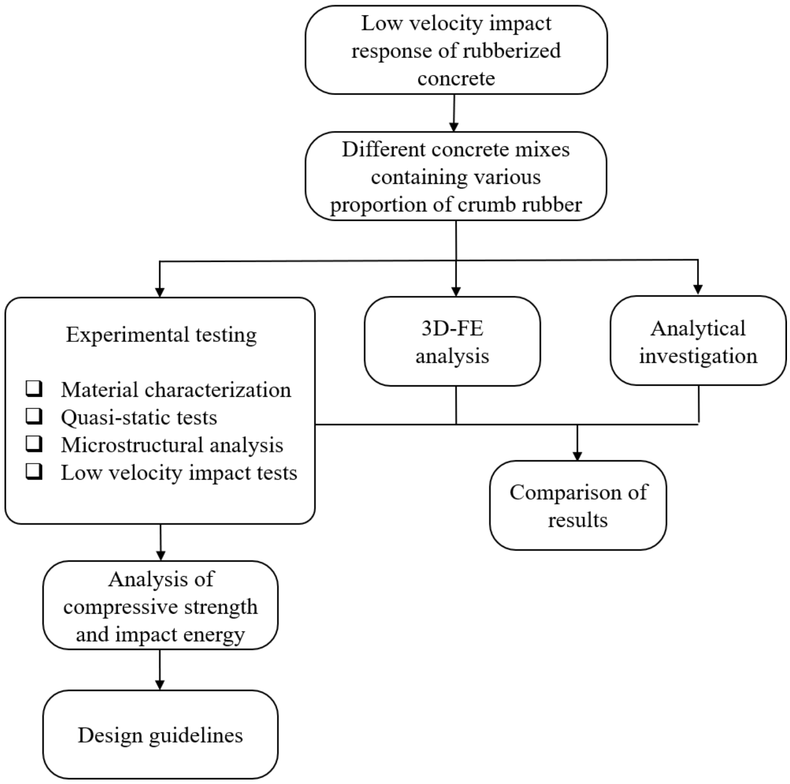

Figure 4.1 Flowchart of the complete methodology for analyzing the low velocity impact response of rubberized concrete

4.2 Details of experimental program

For the proposed experimental program, the following properties of concrete mix have been considered: characteristic compressive strength of 50 MPa, and water/cement ratio of 0.36. OPC 43 grade cement adapting to IS 8112-1989 [169] with a specific gravity 3.038, and normal consistency of 29% is used for casting the specimens. The nominal maximum size of coarse aggregate is 20 mm with a specific gravity of 2.831 and water absorption of 0.85%. Zone II sand with a specific gravity of 2.645 and a water absorption of 3% is used. Crumb rubber of size 0.2-4.75 mm is used as partial sand replacement in various volumetric proportions of 5-30% at intervals of 5% (designated as CR5 – CR30). The specific gravity of crumb rubber sample, and fine aggregates is determined using pycnometer test and found the be 0.9 and 2.645, respectively. The sample of crumb rubber and zone II sand used in this work is shown in Figure 4.2. The sieve analysis for sand and crumb rubber is presented in Figure 4.3. The desired workability of fresh concrete is attained by using liquid BASF Masterpolyheed 8385 superplasticizer. The mix proportions for plain and rubberized concrete are determined as per IS 10262-2019 [164]. The quantities of cement, water, and coarse aggregate are found to be 415 kg, 161 kg, and 1281 kg respectively for 1 m^3 of concrete. While, the fine aggregate, crumb rubber, and superplasticizer content for the several concrete mixes are shown in Table 4.1. In this table, 'CM' represents the control mix with no rubber content, while 'R' represents the concrete mix with crumb rubber. The concrete mixes 'R1' to 'R6' represent increase in crumb rubber content from 5 to 30 % at 5 % intervals. The slump values of all concrete mixes are checked as per IS 1199-1959 (R 2018: Part 2) [165] and obtained in the range of 75 – 110 mm.

(a) (b)

Figure 4.2 Sample of (a) crumb rubber and (b) Zone II sand employed in this study

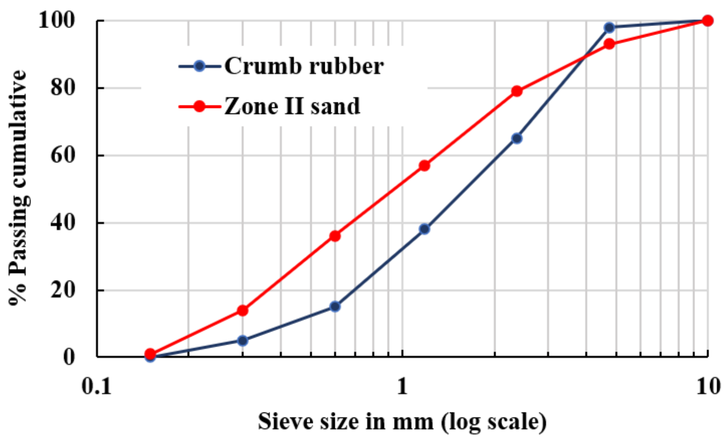

Figure 4.3 Particle size distribution of crumb rubber and fine aggregates (Zone II sand)

Table 4.1 Mix proportion for 1 cubic meter of concrete

Concrete Mix	**Fine Aggregate (kg)**	**Super-plasticizer (kg)**	**% crumb rubber [by volume]**	**Fiber (kg)**
CM	635	1.65	0	0
R1	603	1.65	5	13.2
R2	571	1.65	10	26.4
R3	540	2.47	15	39.6
R4	508	2.47	20	52.8
R5	476	2.47	25	66
R6	444	2.47	30	79.2

For each mix type, six cubes of size 100 mm and 150 mm each have been casted for assessing the quasi-static properties. The compressive strength of concrete cube specimens (100 mm) is determined as per IS 516 (Part 1/Sec 1):2021 [170]. Tests are conducted at 7 and 28 days on three specimens each. For the flexural impact loading test, three beams measuring 500 mm × 100 mm × 100 mm are cast for each mix. All the specimens are subjected to wet curing for 28 days.

The drop impact tests are conducted using an instrumented test setup as per ACI 544.2R-89 [166]. The test setup is the same as that used for the previous objective. The schematic figure and the actual test setup are shown in Figure 3.8 and Figure 3.9 in the previous section. In the present work, a drop height of 500 mm is considered. Moreover, strain gauges SG1 and SG 2 (See Figure 4.4) are installed at the top and bottom face of concrete beam, respectively to record the compressive and tensile longitudinal strains in concrete beam specimens. The concrete beam specimen instrumented with strain gauge on the compressive face is shown in Figure 4.4. The data from all instrumentations are recorded at an interval of 0.11 milliseconds.

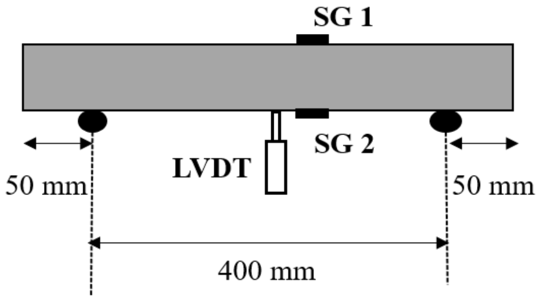

(a)

(b)

Figure 4.4 (a) Schematic representation of strain gauge instrumentation (b) strain gauge installation on compressive face of concrete beam

4.3 Numerical modeling

The 3D-FE model used for the previous objective is used for analyzing the low velocity impact response of rubberized concrete beam. The geometric and material modeling details have already been discussed in Section 3.3. The material parameters for rubberized concrete mixes such as density (ρ), compressive stress-strain response, tensile strength and elastic modulus (E_c) are determined from the experimental tests. The tensile behavior is modeled using modified Hillerborg's model (See Figure 3.4). The effects of high strain rates are incorporated using DIF (Dynamic Increase Factor). In this work, we have used the mathematical DIF models reported in CEB-FIP model code [161]. These models are applicable for plain concrete as well as several fiber-reinforced cementitious materials including crumb rubber concrete. The DIF values obtained from the mathematical models are multiplied with the respective quasi-static values in order to modify the compressive and tensile response models of plain or rubberized concrete. A strain rate of 10 s^{-1} is considered as an upper bound for satisfying the low velocity hard impact strain rate range [163]. The modified compressive and tensile response models used for simulating the behavior of plain and rubberized concrete are shown in Figure 4.5. The dilation angle for plain concrete is taken as 10 degrees. The remaining CDP model parameters for M50 grade concrete are taken from Jankowiak and Lodygowski [158]. The CDP parameters for rubberized concrete are calibrated using experimental results. Since, the use of crumb rubber mainly affects the flexibility of concrete, its influence is considered by varying the dilation angle and fracture energy. Due to lack of testing facilities, the fracture energy values for plain and rubberized concrete are obtained from Raj et al. [171, 172]. The remaining material parameters are the same for plain and rubberized concrete as shown in Table *4.2*. The complete meshing details of the individual components of FE model are shown in Figure 4.6.

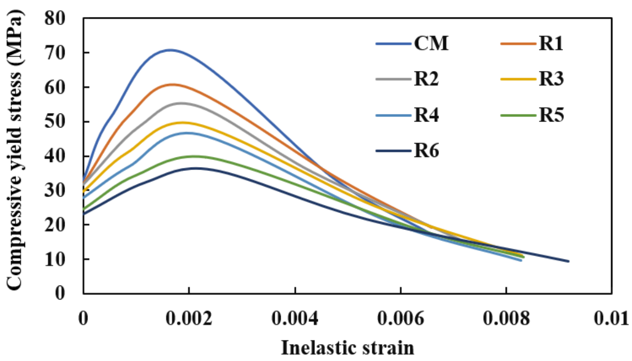

(a)

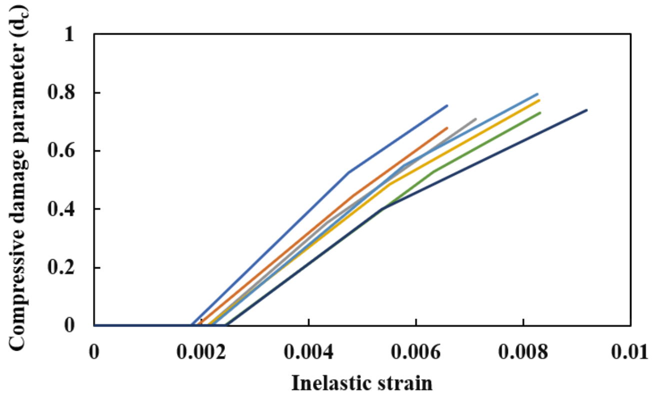

(b)

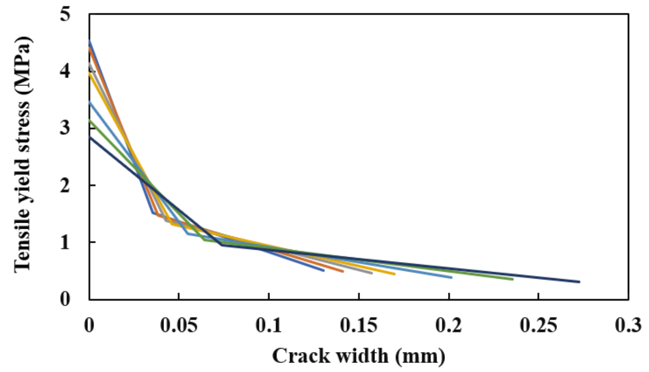

(c)

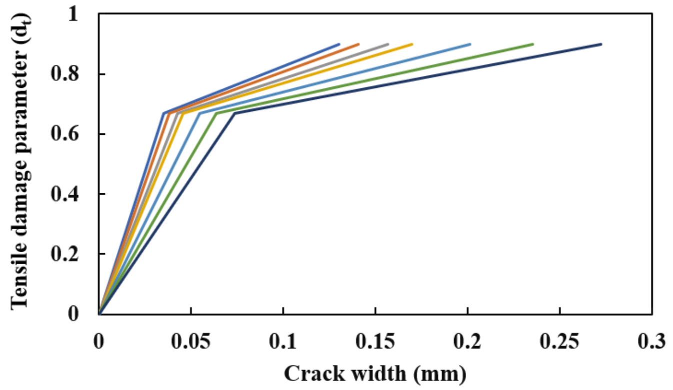

(d)

Figure 4.5 Adapted uniaxial relationships of plain and rubberized concrete for CDP model: (a), (b) compressive parameters (c), (d) tensile parameters

Table 4.2 CDP model parameters for plain and rubberized concrete

Poisson's ratio (ν)	K_c	ε	σ_{bo}/σ_{co}
0.19	0.67	0.1	1.16

Mix	**CM**	**R1**	**R2**	**R3**	**R4**	**R5**	**R6**
ρ **(kg/m^3)**	2490	2471	2453	2435	2417	2398	2390
f_{ck} **(MPa)**	58.9	50.3	45.8	41.2	38.8	32.9	30.2
E_c **(MPa)**	36283	34470	30480	29030	27940	27210	26120
G_f **(N/m)**	148	157.5	165	171	177	187.5	196.5

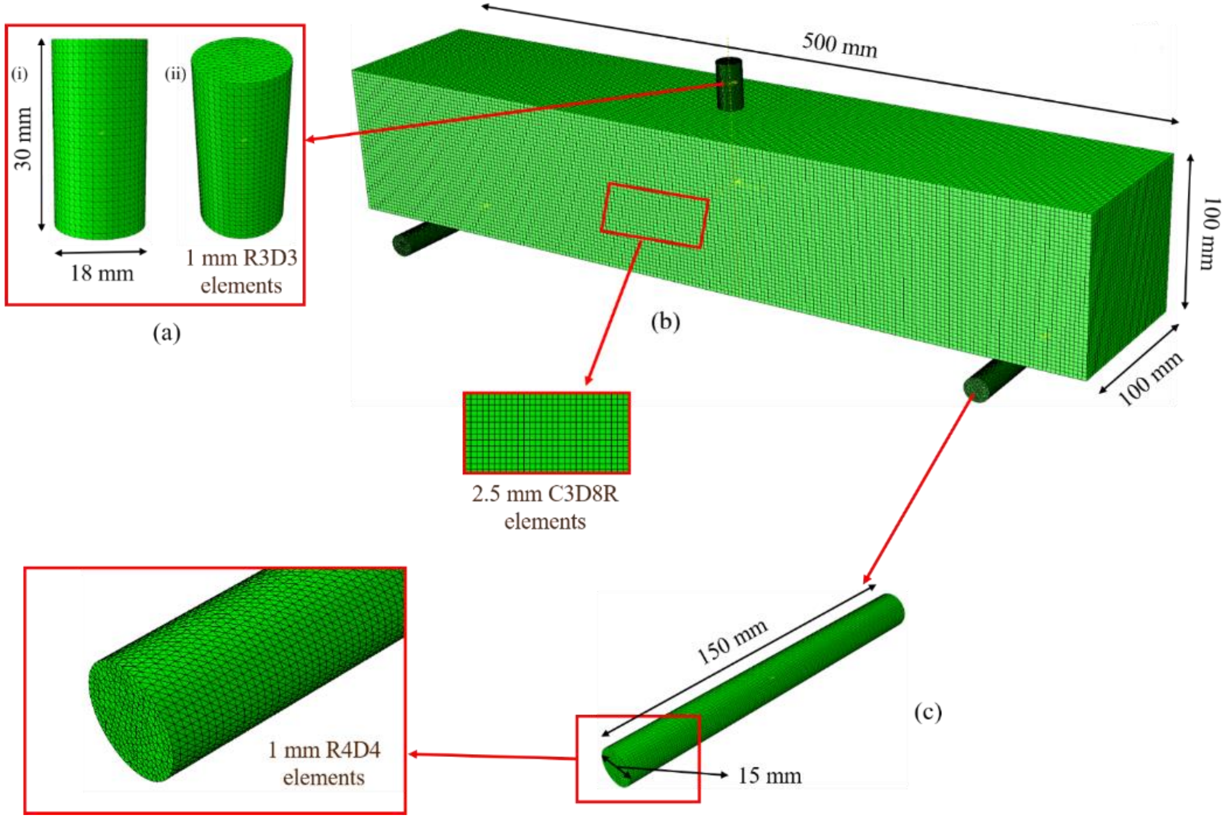

Figure 4.6 Meshing details of various components (a) impactor [(i) front view (ii) front isometric view] (b) concrete beam (c) supporting system

4.4 Experimental test results, numerical results, and a comparison

This section demonstrates the findings of experimental, and numerical analysis performed in the present work. The influence of partial replacement of sand by crumb rubber has been discussed in detail, and the response of concrete beams obtained from the two investigation methods has been compared.

4.4.1 Quasi-static test results

Quasi-static tests are conducted in order to characterize the developed concrete mixes and to compare their general mechanical characteristics. The average uniaxial compressive relationships for various concrete mixes are shown in Figure 4.7. The addition of crumb rubber improves the ductility of concrete as it allows the concrete specimens to withstand compressive loading up to higher strain values. The values of average compressive strength, and modulus of elasticity for various concrete mixes are shown in Table 4.3. It is found that the replacement of sand by crumb rubber reduces the compressive strength of concrete by 15, 22, 30, 34, 44, and 49% while, the modulus of elasticity reduces by 5, 16, 20, 23, 26, and 28% for 5, 10, 15, 20, 25, and 30% rubber replacement, respectively as compared to plain concrete. The results obtained from the present study are in concordance with the previous investigations in [38, 150].

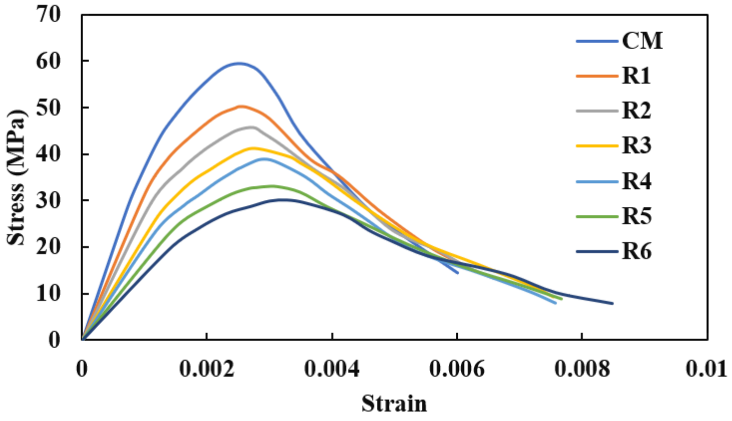

Figure 4.7 Average 28-day compressive relationships for different concrete mixes

Table 4.3 Quasi-static test results for different concrete mixes

Concrete mix	Average compressive strength (MPa)	Average modulus of elasticity (MPa)
CM	58.9	36283
R1	50.3	34470
R2	45.8	30480
R3	41.2	29030
R4	38.8	27940
R5	32.9	27210
R6	30.2	26120

4.4.2 Low velocity impact test results

The results of impact force time histories obtained from experimental and 3D-FE simulations for plain and rubberized concrete are shown in Figure 4.8. The impact force attains a peak value suddenly which is obtained due to inertial resistance, followed by damage induced softening of the curve. The time period of impact event ranges from 1.5 ms to 1.78 ms. The increase in crumb rubber content in concrete results in an increment in the peak impact force values (See Table 4.4), which is consistent with the results of Al-Tayeb et al. [17]. Also, the contact time between drop weight and specimens is higher for rubberized concrete specimens. These trends are observed due to flexible nature of rubberized concrete beams which is obtained due to high plastic energy capacity of crumb rubber. The presence of crumb rubber enhances the impact strength, and the ability of concrete beams to resist higher impact loads. At 30% replacement level, the peak impact force value is increased by approximately 23%. It is also observed that the developed 3D-FE model reproduces the impact force time histories with reasonable accuracy. The use of higher values of dilation angle and fracture energy results in an enhancement in the flexibility, plastic energy absorption capacity, strength, as well as resistance to crack development [85, 173]. Hence, crumb rubber concrete displays higher peak impact force values in the FE analysis. The peak impact force values are predicted with a maximum error of 4.6% with respect to the experimental results.

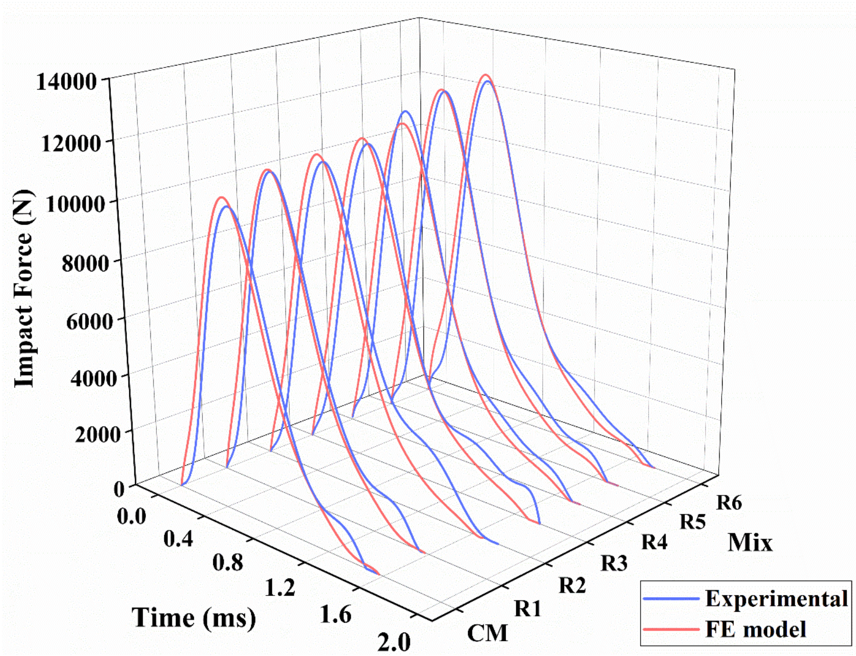

Figure 4.8 Experimental and predicted impact force-time histories for different mixes

Table 4.4 Peak impact force values for plain and rubberized concrete mixes obtained from experimental and 3D-FE analysis

Concrete Mix	Experimental results		Predicted results by 3D-FE method	
	Peak impact force (N) (1)	**% increase w.r.t. CM**	**Peak impact force (N) (2)**	**% error w.r.t. (1)**
CM	10212	0	10681	4.6
R1	11057	8.27	11159	0.93
R2	11081	8.5	11239	1.42
R3	11403	11.66	11437	0.29
R4	11669	14.27	11547	1.05
R5	12249	19.94	12411	1.32
R6	12547	`22.86	12663	0.93

The displacement time response of plain and rubberized concrete beams obtained from experimental and 3D-FE simulations is shown in Figure 4.9. As the impact force is applied to the specimens, the displacement magnitude increases. However, it is observed that as soon as the specimens reach peak impact force, the displacement values start increasing at a higher rate until the impact force becomes zero. The provision of crumb rubber enhances the flexibility of concrete beams, which is reflected in the displacement time histories of various concrete mixes. This trend is observed due to higher plastic energy absorption capacity and flexibility of crumb rubber. The 3D-FE model reproduces the experimental results with a good accuracy. The peak displacement values for various concrete mixes obtained from experimental and numerical investigations are presented in Table 4.5. The increase in percentage of crumb rubber results in an increase in the peak displacement values. At 30% replacement, the peak displacement value is increased by approximately 71%. The developed 3D-FE model reproduces the peak mid-point displacement values with a maximum error of 11.3% with respect to the experimental results.

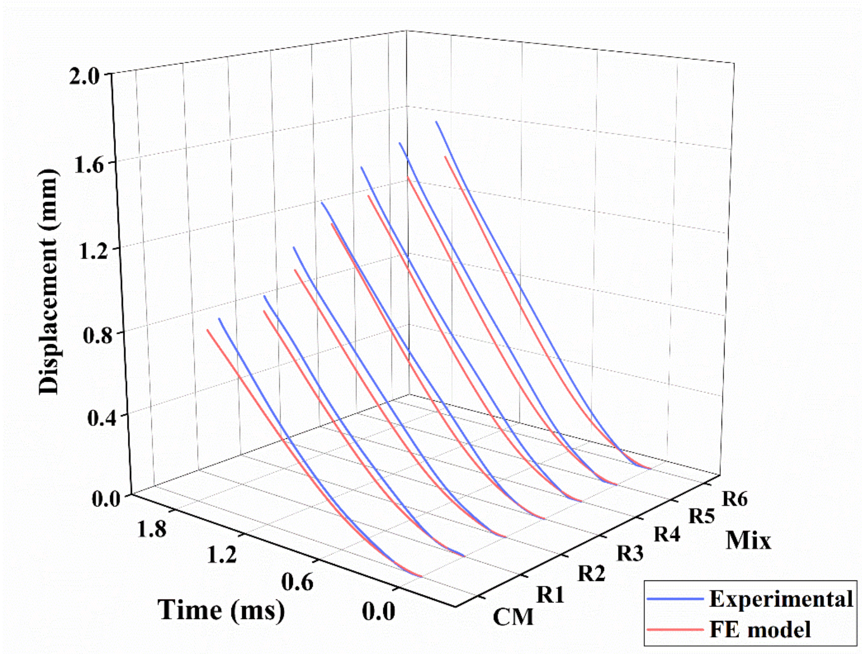

Figure 4.9 Mid-point displacement time histories for different mixes

Table 4.5 Peak displacement values for plain and rubberized concrete mixes obtained from experimental and 3D-FE analysis

Concrete Mix	Experimental results		Predicted results by 3D-FE method	
	Peak mid-point displacement (mm) (1)	% increase w.r.t. CM	Peak mid-point displacement (mm) (2)	% error w.r.t. (1)
CM	0.919	0	0.85	7.5
R1	0.967	5.2	0.89	7.86
R2	1.13	22.96	1.02	9.7
R3	1.29	39.9	1.19	7.46
R4	1.42	54.3	1.28	9.76
R5	1.5	63.2	1.33	11.3
R6	1.57	70.84	1.393	11.3

The load (impact force) vs displacement curves for various concrete mixes obtained from experimental and 3D-FE simulations are displayed in Figure 4.10. The energy absorption capacity is evaluated as the area under the load vs displacement curve. The values of energy absorption capacity for different concrete mixes are presented in Table 4.6. With the use of crumb rubber as 10, 20, and 30% replacement of sand, the energy absorption capacity increases by 49, 71, and 98% respectively. Thus, it can be concluded that the use of crumb rubber significantly enhances the energy absorption capacity of concrete, which is a desirable trait for the case of concrete safety and protection barriers. Also, the load-displacement curves obtained using 3D-FE analysis agree with the experimental load-displacement curves. The energy absorption capacity is well predicted by the FE analysis with a maximum error of 25%.

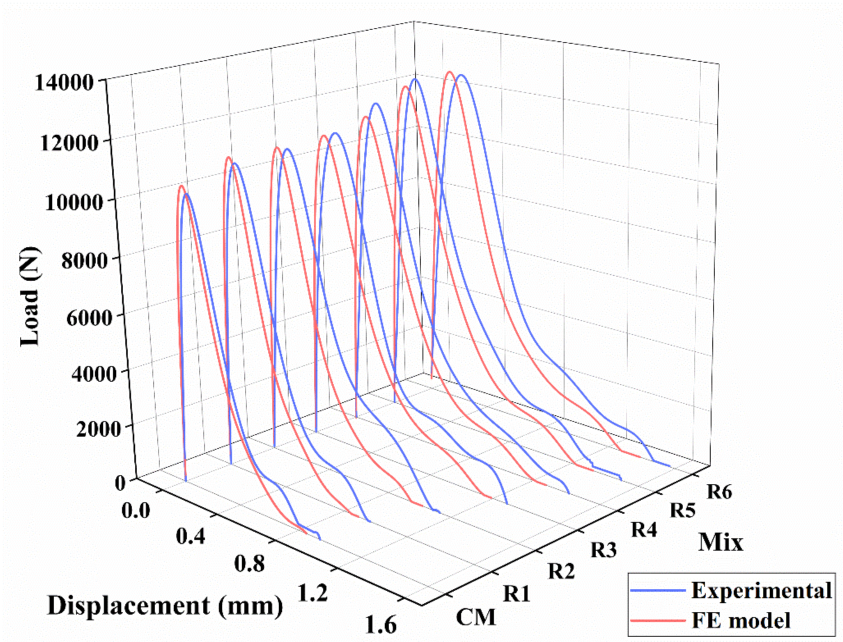

Figure 4.10 Load vs displacement curves for different mixes

Table 4.6 Energy absorption capacity of different concrete mixes

Concrete Mix	Experimental results		Predicted results by 3D-FE method	
	Energy absorption (N-m) (1)	% increase w.r.t. CM	Energy absorption (N-m)	% error w.r.t. (1)
CM	3.5	0	3.16	9.7
R1	4.26	21.7	3.33	21.8
R2	5.19	48	3.86	25.6
R3	5.69	62.6	4.65	18.3
R4	5.99	71.2	5.21	13
R5	6.44	84	5.33	17.3
R6	6.93	98	5.52	20.3

The strain-time histories obtained at the compressive and tensile faces of different concrete beams are shown in Figure 4.11. SG1 represents compressive strain values at the top surface of concrete beam near the point of impact, while SG2 represents tensile strain values at the bottom face. The magnitude of strain at top as well as bottom face increases as the beam deformation occurs due to the application of impact force. The concrete beam attains a maximum strain value when the peak impact force is reached. This is followed by crack initiation, which eventually reduces the resistance of concrete beam and results in decreased impact force values. The reduced resistance of concrete beam causes a relaxation in the strain values. As the complete failure of concrete beam occurs, the impact force as well as strain values also become zero. The provision of crumb rubber results in an increase in the peak strain values which is attributed to improved flexibility and deformation capacity of crumb rubber concrete.

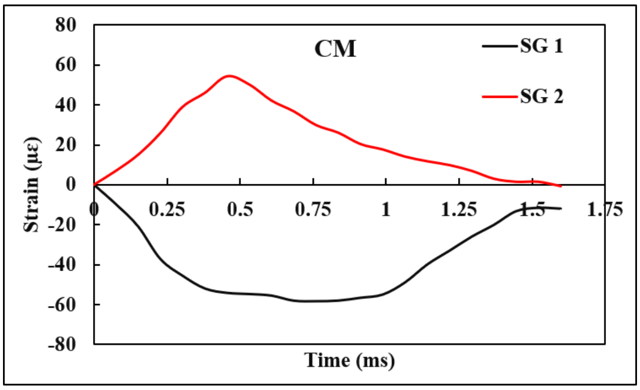

(a)

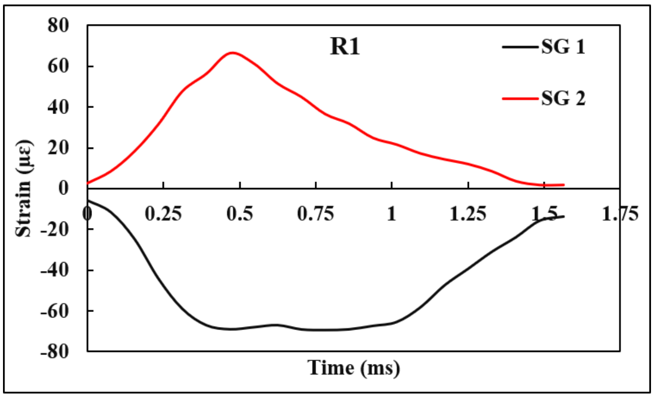

(b)

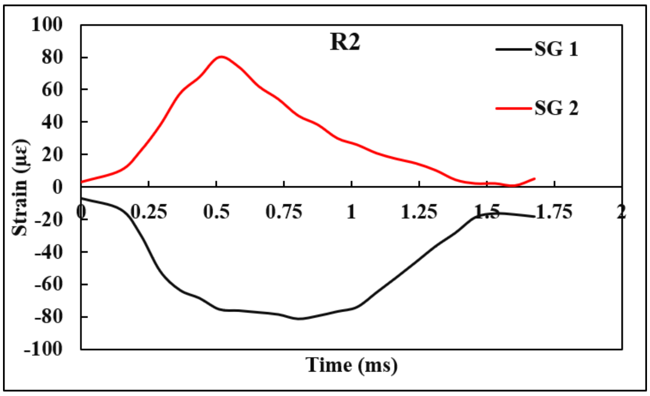
R2
SG 1
SG 2
Strain (με)
Time (ms)
100
80
60
40
20
0
-20
-40
-60
-80
-100
0
0.25
0.5
0.75
1
1.25
1.5
1.75
2

(c)

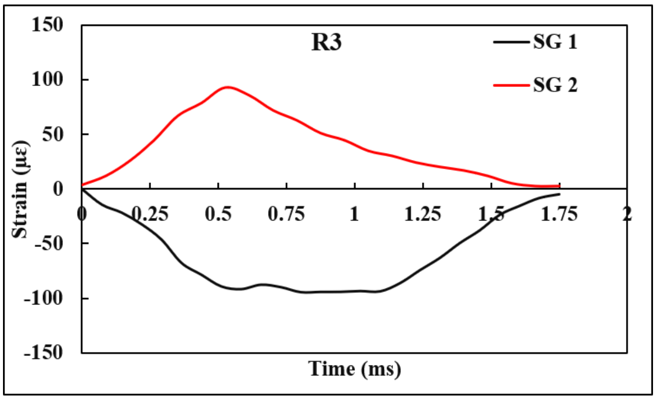
R3
SG 1
SG 2
Strain (με)
Time (ms)
150
100
50
0
-50
-100
-150
0
0.25
0.5
0.75
1
1.25
1.5
1.75
2

(d)

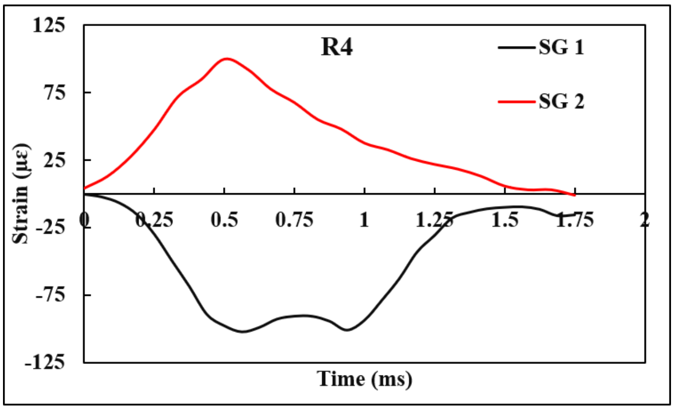
R4
SG 1
SG 2
Strain (με)
Time (ms)
125
75
25
-25
-75
-125
0
0.25
0.5
0.75
1
1.25
1.5
1.75
2

(e)

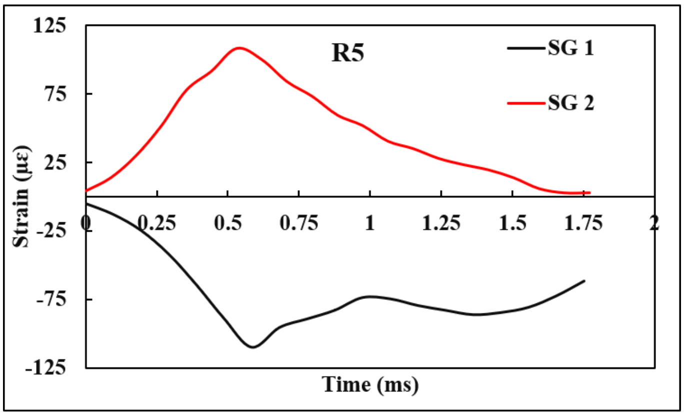

(f)

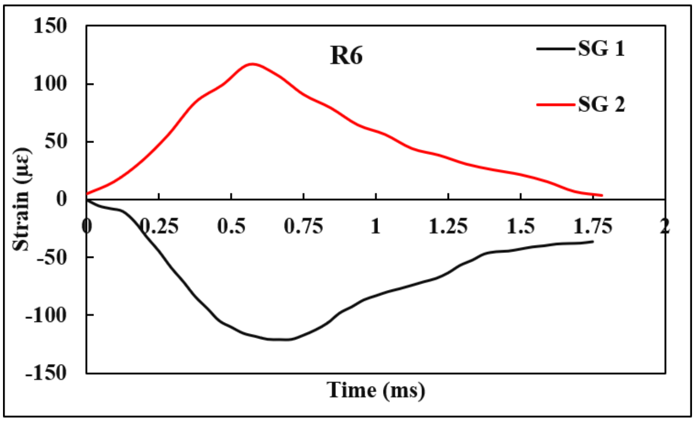

(g)

Figure 4.11 Strain time histories for different mixes (a) Control mix (b) R1 (c) R2 (d) R3 (e) R4 (f) R5 (g) R6

The typical failure pattern for all concrete mixes is shown in Figure 4.12. The plain as well as rubberized concrete beams exhibit flexural failure mode. The initiation of flexural cracks occurs on the lower surface of concrete beam, propagating vertically upwards towards the zone of impact. The 3D-FE model accurately reproduces the failure mode of concrete beams. Furthermore, the damage resulting from low velocity impact on plain and rubberized concrete beams is quantified in terms of crack width. Prior to the complete failure of specimens, the horizontal crack width is measured at the middle section on the front face with the help of digital imaging (See Figure 4.13). The tests are recorded using slow motion digital imaging. The stage before which concrete completely splits off and separates into two different components is captured. A total number of three specimens are tested, and the average of this data is used to evaluate the crack width. The values of crack width for different concrete mixes are presented in Table 4.7. It is evident that the increase in percentage of crumb rubber results in a nominal reduction in the crack width. This is observed due to the bridging action and crack arresting properties of crumb rubber.

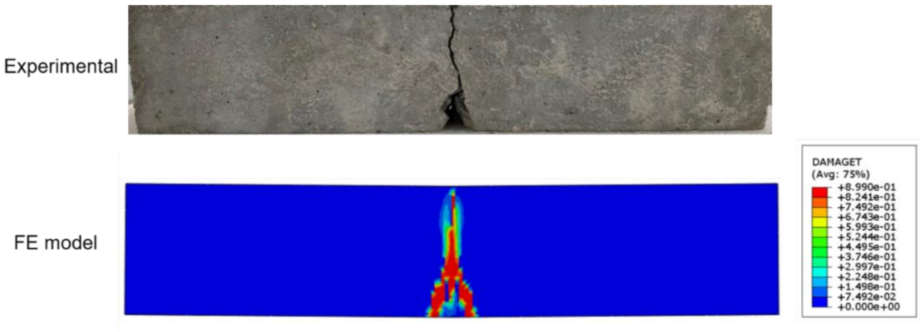

Figure 4.12 Failure pattern of concrete beams

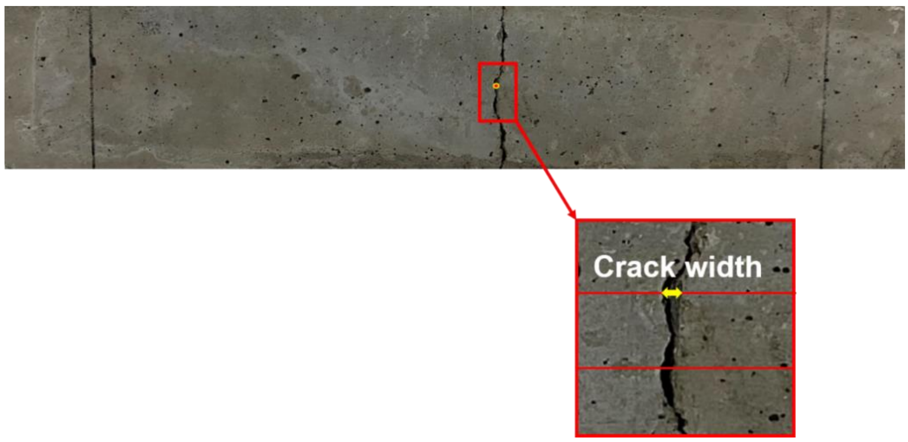

Figure 4.13 Crack width measurement at frontal face of concrete beams

Table 4.7 Results of crack width for plain and rubberized concrete specimens

Concrete Mix	Crack width (mm)	% reduction w.r.t. CM
CM	1.363	0
R1	1.26	7.59
R2	1.22	10.52
R3	1.218	10.67
R4	1.168	14.32

R5	1.159	15.03
R6	1.156	15.2

4.5 Analytical investigation

In this work, a methodology has been derived for estimating the peak displacement of concrete beams, which is based on mass, energy and momentum conservation. From the experimental investigations, it has been observed that the flexural failure of concrete occurs with negligible or no fragmentation. Hence, the mass of beam remains constant during impact testing. The concrete beam is considered to be impacted by a drop hammer, which has an initial velocity of v_o (See Figure 4.14). After impact, the velocity of hammer becomes v_t, and the beam also starts moving downward.

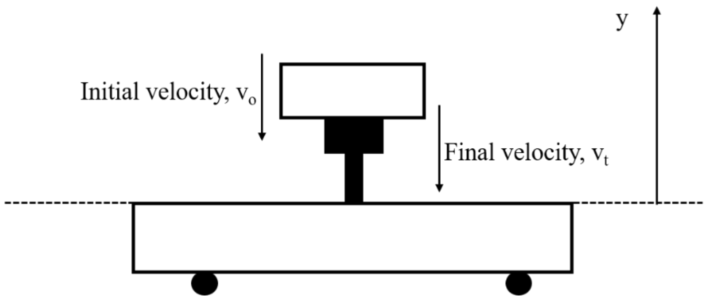

Figure 4.14 Impulse and momentum change of drop hammer

The initial velocity of drop weight may be given as:

$$v_o = \alpha\sqrt{2gh} \quad (4.1)$$

where, h is the drop height, g is the acceleration due to gravity, α is the ratio of actual impact velocity to the free fall velocity. The factor α considers frictional losses between the steel frame and impactor arrangement.

According to the principle of momentum conservation, the change in momentum of drop weight must be equal to the impulse (S) produced by the reaction force from the concrete beam. Hence,

$$S = M_h v_t - M_h v_o \quad (4.2)$$

where, M_h is the mass of drop weight.

Since, the impulse (S) is the area under load time history plot. Hence, Eqn. (4.2) may be written as:

$$\int p(t)dt = M_h v_t - M_h v_o \tag{4.3}$$

By rearranging Eqn. (4.3), the final velocity of drop weight may be written as:

$$v_t = v_o - \frac{1}{M_h}\int p(t)dt \tag{4.4}$$

Based on the principle of energy conservation, the change in kinetic energy of drop weight must be equal to the energy imparted on the concrete beam. Hence,

$$\frac{1}{2}M_h(v_t^2 - v_o^2) = E_{abs} + KE_{beam} \tag{4.5}$$

where, E_{abs} is the energy absorbed/dissipated by the concrete beam, KE_{beam} is the kinetic energy of beam.

Substituting the values of v_t and v_o from Eqns. (4.1) and (4.4) to Eqn. (4.5), we have:

$$\frac{1}{2}M_h\left[\left(\alpha\sqrt{2gH} - \frac{1}{M}\int p(t)dt\right)^2 - 2gH\alpha^2\right] = E_{abs} + \frac{1}{2}M_{beam}V_{beam}^2 \tag{4.6}$$

Now, it is assumed that the velocity of concrete beam at its center point is equal to the initial velocity of the impactor (v_o). Since, the exact velocity profiles of concrete beams under low velocity impact are unavailable in the literatures. Hence, two different velocity profiles are assumed i.e., parabolic, and sinusoidal (See Figure 4.15), and the average beam velocity is calculated. The average beam velocity is then used to determine the kinetic energy of the beam. The energy absorbed by the concrete beam is calculated as:

$$E_{abs} = \frac{1}{2}M_h\left[\left(\alpha\sqrt{2gH} - \frac{1}{M}\int p(t)dt\right)^2 - 2gH\alpha^2\right] - \frac{1}{2}M_{beam}V_{beam}^2 \tag{4.7}$$

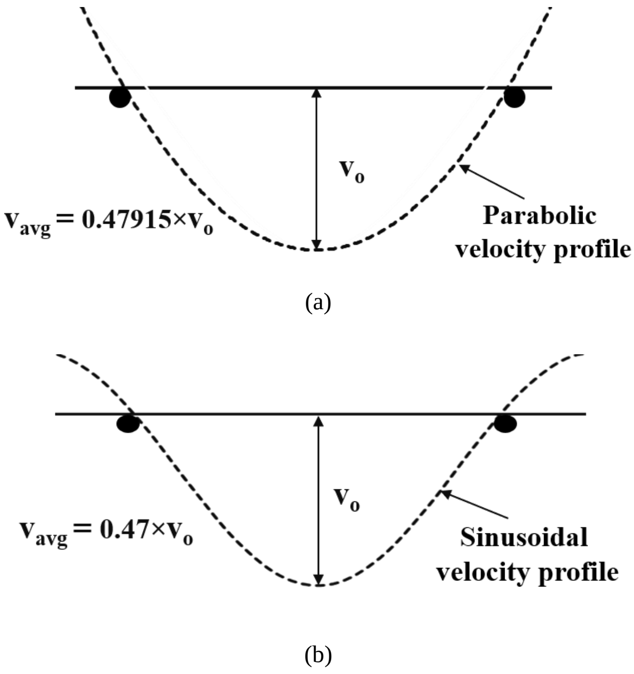

Figure 4.15 Assumed velocity profiles for concrete beam (a) parabolic (b) sinusoidal

Now, the momentum conservation principle is used to convert the impact load history to an equivalent static load value (P_{static}) throughout the loading period (See Figure 4.16).

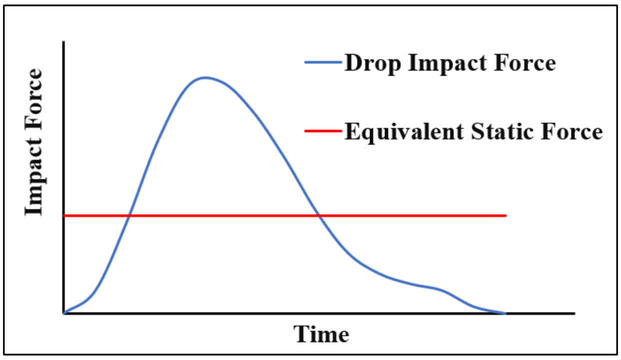

Figure 4.16 Idealization of drop impact force to equivalent static force

According to principle of energy conservation, the energy absorbed by beam should be equal to the work done by equivalent static load in producing a displacement ‘u’. Hence, the displacement ‘u’ is determined as:

$$u = \frac{E_{abs}}{P_{static}} \tag{4.8}$$

The peak displacement values for various concrete mixes are calculated using Eqn. (4.8), and compared with the experimental values as shown in Table 4.8. It is evident that the results obtained using the proposed analytical equation have a good correlation with the experimental counterparts. A maximum deviation of 0.106 mm with an error of 11.2% is observed. Additionally, the energy absorption capacity is also compared in Table 4.9. The proposed analytical method predicts the energy absorption capacity of concrete beams with a maximum deviation of 13.8 %.

Table 4.8 Comparison of peak displacement values obtained from the proposed analytical method

Mix	Peak displacement (mm)						
	Exp. [a]	Using assumed velocity profiles and Eqn. (4.7) and Eqn. (4.8)				Using load-displacement curve and Eqn. (4.8)	
		Par. velocity profile		Sin. velocity profile			
		Value	% error w.r.t. [a]	Value	% error w.r.t. [a]	Value	% error w.r.t. [a]
CM	0.919	0.816	11.2	0.898	2.3	0.813	11.5
R1	0.967	0.945	2.6	1.05	8.2	0.989	1.96
R2	1.13	1.12	0.89	1.245	10.2	1.206	6.7
R3	1.29	1.23	4.6	1.332	3.3	1.323	2.56
R4	1.42	1.345	5.3	1.456	2.5	1.393	1.9
R5	1.5	1.38	8.1	1.489	0.74	1.497	0.2
R6	1.57	1.425	9.2	1.533	2.36	1.61	2.5

Exp.=Experimental

Table 4.9 Comparison of energy absorption capacity using experimental and analytical method

Mix	Experimental results		With par. velocity profile and Eqn. (4.7)		With sin. velocity profile and Eqn. (4.7)	
	Energy abs. (N-m)	% increase	Energy abs. (N-m)	% error	Energy abs. (N-m)	% error

	(1)	w.r.t. CM		w.r.t. (1)		w.r.t. (1)
CM	3.5	0	3.36	4	3.86	10.3
R1	4.26	21.7	4.35	2.1	4.85	13.8
R2	5.19	48.3	5.61	8.1	5.82	12.1
R3	5.69	62.6	5.76	1.2	6.26	10
R4	5.99	71.1	5.97	0.33	6.47	7.4
R5	6.44	84	6.16	4.3	6.65	3.3
R6	6.93	98	6.41	7.5	6.9	0.44

4.6 Microstructural analysis

Microstructural investigation of plain and rubberized concrete specimens has been carried out using SEM (Scanning Electron Microscopy) imaging. The tests are performed on cuboidal cores of size 1 cm × 1 cm × 0.8 cm, which are extracted from the concrete cube specimens. The surface of the cores is polished using abrasive grit papers (silicon carbide) of grades 200, 400, 600, 800, 1200, 2000, and 2500 µm. The surface is then polished with diamond paste of three different micron sizes (1, 2, 3). Finally, the specimens are oven dried and polished with a gold coating to prevent any charge collection during the investigation. The SEM images of plain as well as rubberized concrete (20% crumb rubber replacement) specimens are shown in Figure 4.17. The various microstructural characteristics such as C-S-H (Calcium-Silicate-Hydrate), C-H (Calcium Hydroxide), E (Ettringite), and interfacial transition zone are clearly visible in these Figures. For the plain concrete specimens, the dense interfacial zones are attributable for the superior mechanical properties (compressive strength, split tensile strength, and elastic modulus). While, in case of rubberized concrete specimens, the interfacial zones between crumb rubber and cement matrix consist of gaps, which reflects a weaker bond of crumb rubber with the cement matrix due to its hydrophobic character. This is responsible for reduced denseness of interfacial zones, which consequently affects the mechanical properties. However, the presence of crumb rubber acts as a bridge in arresting crack propagation and reduces the crack velocity due to its elastic nature, which eventually results in an improved response of concrete under impact loading. The presence of elastic crumb rubber as well as gaps/microcracks in rubberized concrete also behaves as a toughening mechanism, and may also be responsible for the improvement in the performance of rubberized concrete under impact loading.

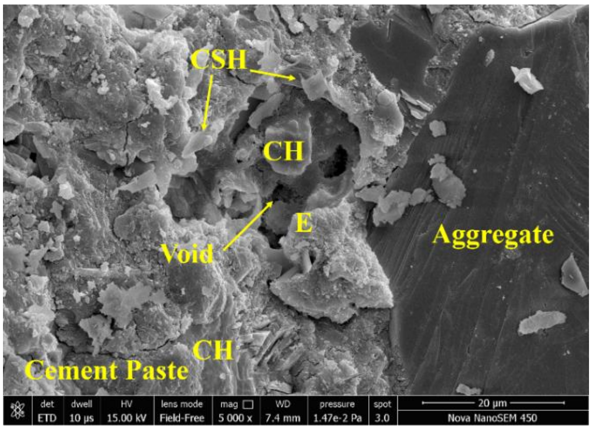

(a)

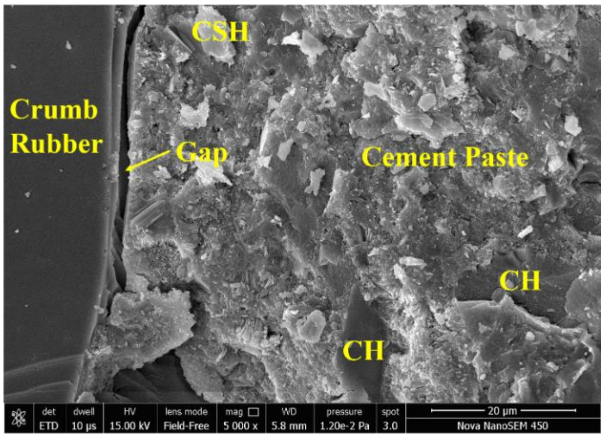

(b)

Figure 4.17 SEM image of (a) plain concrete at 5,000x magnification and (b) rubberized concrete (20 % crumb rubber) at 5,000x magnification

4.7 Design guidelines for selection of optimum rubber content

This section presents the design guidelines for selection of optimum rubber content as partial sand replacement in concrete. Compressive strength and energy absorption capacity of concrete are taken as the two main parameters. The energy absorption capacity is calculated as the area under load vs displacement curve. However, this value is not an absolute measure of the absorbed energy, as it depends on the loading conditions, rate of loading, geometry and weight of specimen. Based on the previous studies carried out by Pham et al. [39] and Hu et al. [174], a specific energy value (SEV) parameter is taken, which is an absolute measure of the energy absorbed by concrete. SEV parameter is a dimensionless number which may be calculated as:

$$SEV = \frac{Energy\ absorption\ capacity}{V \times f_{ck}} \tag{4.9}$$

where, V is the volume of the concrete specimen tested under low velocity impact, f_{ck} is the static compressive strength of concrete.

The proposed design guideline chart for M50 grade concrete is shown in Figure 4.18. This chart represents the values of compressive strength and SEV for different proportions of crumb rubber in concrete. The following chart can be utilized to select an optimum rubber content such that a desired minimum compressive strength is achieved with the enhancement in impact resistance and SEV of concrete. The SEV value determined from this chart can then be utilized for determining the energy absorption capacity based on the size and compressive strength of the concrete.

The design guideline chart has several limitations. It could be utilized for M50 grade concrete only. Also, this chart is valid for the specific particle size distribution of crumb rubber. A larger deviation in particle size distribution may result in reduced accuracy. Hence, further experimental studies are suggested for development of thorough design guidelines considering a range of parameters.

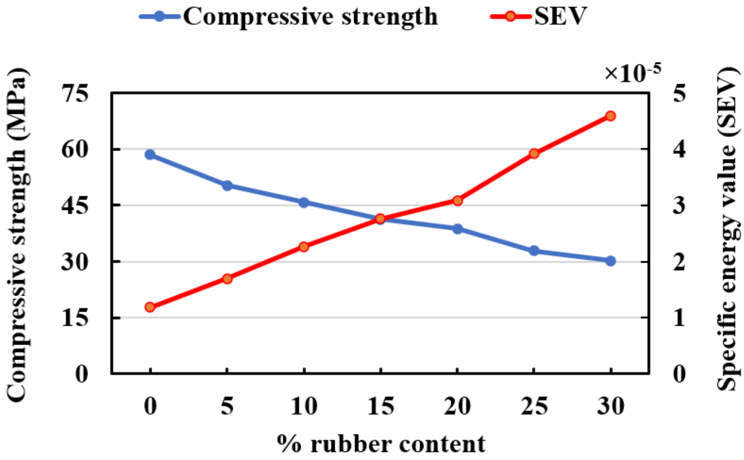

Figure 4.18 Design guideline chart for selection of rubber content

4.8 Summary

In this work, detailed experimental investigations have been performed to analyze the influence of crumb rubber as partial sand replacement on the low velocity impact response of concrete beams. Further the macroscopic response of concrete is linked with its microscope attributes by conducting SEM analysis. Various proportions of crumb rubber as partial replacement of sand (0 – 30%) are considered. The response of concrete beams is also investigated numerically and analytically. Further, an effort has been given to link the macroscopic response of plain and rubberized concrete with the respective microscopic attributes by conducting microstructural investigations.

The addition of crumb rubber enhances the peak impact force values of the concrete beams. At 30% replacement, the peak impact force is increased by approximately 23%. The developed 3D-FE model predicts the peak impact force values with a maximum deviation of 4.6%. Also, the crumb rubber has been found to increase the ductility and energy absorption capacity of concrete beams, which is observed due to higher plastic energy absorption capacity of rubber. This is a desirable trait for concrete safety and protection barriers. At 30% replacement, the peak displacement of concrete beam is increased by approximately 71%, while the energy absorption capacity is increased by 98%. The 3D-FE model as well as the proposed analytical method reproduce the peak displacement values with a maximum deviation of 11.3% and 11.5%, respectively. While, the energy absorption capacity of concrete beams is predicted with a maximum deviation of 25% and 13%, respectively.

The presence of elastic crumb rubber as well as the gaps/microcracks in rubberized concrete promote toughening mechanism leading to improved impact resistance. Also, the presence of crumb rubber imparts bridging action which eventually arrests the crack development. Although, the presence of gaps/microcracks between crumb rubber and cement matrix results in a weak interfacial zone, which is mainly responsible for the reduction in the quasi-static mechanical properties of concrete. Finally, simple design guidelines have been proposed for M50 grade concrete which could be utilized for selecting optimum rubber content such that the desired minimum compressive strength is achieved with improved impact resistance properties.

Chapter-5

GFRP as a protective covering over subsurface Reinforced Concrete tunnels

5.1 Introduction

Subsurface tunnels are substantially used in metropolitan cities as rapid transit system for masses. However, the recent terrorist attacks on subways of different cities such as London (2005), Moscow (2010 & 2004), Minsk (2011), Istanbul (2015), Belgium (2016), and Saint Petersburg (2017) have raised the concern for the safety of tunnels in case of an internal blast [95]. An internal blast may result in development of circumferential faults and fractures which can merge together and degrade the tunnel structure. Also, it may contribute towards several types of geotechnical hazards such as rock fault, liquefaction, and reduced soil shear strength. The above discussed consequences may not only result in possible loss of human lives but also cause huge infrastructural damage and drastic financial losses. The damage induced in underground tunnels due to explosion depends on the tunnel lining material, quantity of explosive, and the neighboring geological condition [88, 89]. Thus, to reduce the potential damage of tunnels in case of internal blast loading, it is necessary to explore for blast mitigation methods utilizing new materials as protective layer instead of designing an uneconomical rigid structure.

Previously, several experimental studies have investigated the response of structural elements such as RC slabs against blast and impact loading [3, 23, 82, 90–92, 175–177]. However, the experimental studies related to internal blast loading on tunnels are not viable from economic and political point of view. Since, the tunnel sections have considerable cross-sectional dimensions and complicated reinforcement arrangements, the experimental testing would require huge costs. Also, the blasting experiments must be performed with due care in a remote area due to the association of high risks, thus causing political issues in any area. Due to this the literatures related to internal explosion tests on tunnels are very scarce. The only available study has been performed by Zhao et al. [93], in which they carried out full-scale internal explosion tests. This study focused on the determination of critical points which control the response of tunnels as well as the damage and failure mechanisms which take place in case of an internal explosion. The drawback of this study was that the experimental blast tests were performed on vertically assembled tunnel linings, in which the cross-section of tunnel was kept horizontally on the ground. Hence, the effect of overburden pressure of soil lying above the tunnel surface in the practical case is not reproduced.

Apart from the experimental studies, analytical methods could also be utilized for the analysis of tunnels against internal blast. However, the analytical methods evolved till now are based on simplifications, such as conversion of a problem to single degree of freedom (SDOF) or multiple degree of freedom (MDOF) system. The use of such simplifications for complicated subsurface structures such as circular tunnels may not reflect the actual scenario in case of internal blast. Hence, the analytical methods are not very accurate and remain unsuitable for the internal blast analysis of tunnels.

With the current progression in numerical methods, and evolution of material constitutive models, the numerical techniques such as 3D-FE methods have become more reliable for solution of complex dynamic problems. Thus, the numerical blast investigation of tunnels is highly preferrable and can be carried out well using sophisticated FE packages. Several numerical studies have utilized different methods to investigate the dynamic response of underground structures and soil against blast loading. Some common methods include: computational fluid dynamics (CFD) [88, 95], coupled Euler Lagrange (CEL) and Arbitrary Lagrangian Eulerian (ALE) [97–100], and CONWEP tool [5, 102–107]. Among the different methods, the use of CEL and ALE techniques are highly advantageous in modeling the blast response of tunnels as they accurately consider the different phenomenon such as reflection and focusing of shock waves developed in case of internal explosion. However, due to the complex nature of the problem, the coupled analysis demands rigorous modeling efforts and hefty numerical simulations [101]. On the other hand, the uncoupled 3D-FE analysis methods (such as CONWEP tool) are simpler and provide a good balance between computational expenses and accuracy. Due to this, uncoupled analysis method utilizing CONWEP tool has been given a consideration in this work.

Due to the strategic importance of subsurface tunnels, several studies have explored different methods for the mitigation of blast effects and the anti-blast design of tunnels. The idea of utilizing a sacrificial cladding layer for absorption of blast energy is found to be a good option for blast resistant design [25, 108]. Among the different sacrificial materials, the external bonding of fiber reinforced polymer (FRP) has been verified for improving the strength, stiffness, impact resistance, and ductility, of various structural elements including columns, walls, beams, and slabs. It has also gained high popularity due to its excellent properties, high tensile strength, and outstanding resistance to corrosion [115]. Also, the use of carbon fiber reinforced polymer (CFRP) as a protective shield has been found to improve the performance of tunnel against blast loading [29]. However, among the different FRP materials, GFRP is the most economical and has a low conductivity and high thermal insulation. Thus, GFRP is a highly suitable material for strengthening the structural components against blast. However, its utilization as a sacrificial layer over RC tunnels against internal explosion remains unexplored.

In this work, the blast effectiveness of GFRP as a protective covering has been explored over typical subsurface RC tunnels utilized in Indian Underground Metro System [Delhi Metro]. The response of underground tunnels with two different surrounding soil mediums (saturated and unsaturated) and additional protective layer of 20 mm thick GFRP blanket against different explosive charges is investigated in detail. Considering the context of metro tunnels, they are more likely to be subjected to lower explosive charges of 10 to 50 kg [102]. Additionally, higher explosive charges have also been assessed to check the efficiency of protective layer. The FE investigations are performed using ABAQUS/EXPLICIT [35]. The influence of high strain-rate is incorporated by utilizing strain-rate dependent material properties for all the components. The behavior of concrete, soil, GFRP and steel bars has been modeled using Mohr-Coulomb plasticity, concrete damaged plasticity (CDP), Hashin damage, and Johnson-Cook models, respectively. The blast loading has been simulated using CONWEP tool. The performance of these tunnels is quantified based on the displacement, von-Mises stress-time histories, damage, and plastic strain values.

5.2 3D Finite Element Modeling

In this work, a segment of 300 mm thick RC tunnel having 2.7 m internal radius is considered as a representative of the RC tunnels utilized in the Indian Underground Metro system [Delhi Metro]. This section elaborates the establishment of FE model used for analyzing the efficacy of GFRP as a protective cover over underground RC tunnels exposed to different intensities of internal blast loading.

5.2.1 Modeling of RC tunnel, soil, explosive and GFRP layer

The 3D model of underground tunnel is created using ABAQUS/EXPLICIT [35] as shown in Figure 5.1(a). A tunnel section measuring 20 m in length, 2.7 m internal radius and thickness of 300 mm is neighbored by the soil medium of size 20 m × 26 m × 26 m (See Figure 5.1(b)). Considering a typical context of metro tunnels, the center point of tunnel is kept 13 m below the ground surface. A sacrificial GFRP layer of thickness 20 mm is considered to cover the inner walls of the tunnel. The longitudinal and transverse/confining reinforcement consist of 10 mm diameter Fe-415 steel bars. The confining reinforcement rings in transverse direction are spaced at 300 mm center to center distance. The rings are provided in two layers with a thickness of 120 mm in between them. The longitudinal reinforcement along the circumference of each transverse ring consists of 20 bars. The reinforcement detailing and spacing data typically used for metro tunnel linings in Delhi Metro, India are simplified and adapted as per previous literatures [5, 100] as shown in Figure 5.1(c). In order to prevent the reflection of blast waves from the soil boundaries, non-reflecting type boundary conditions have been used using acoustic impedance technique in ABAQUS.

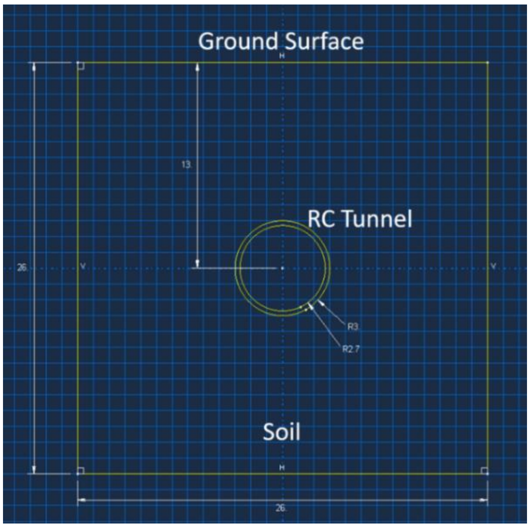

(a)

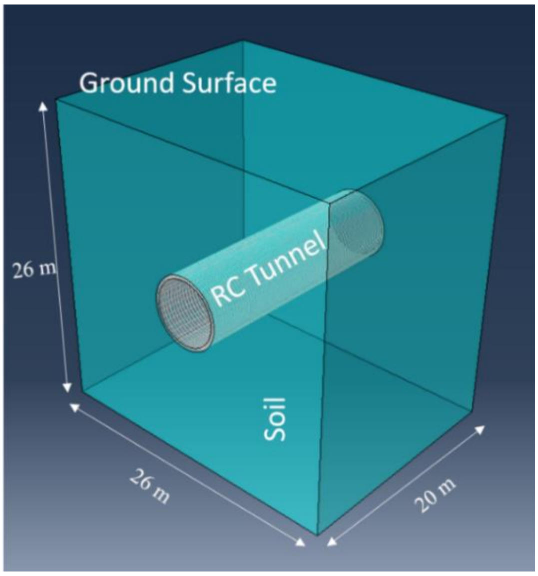

(b)

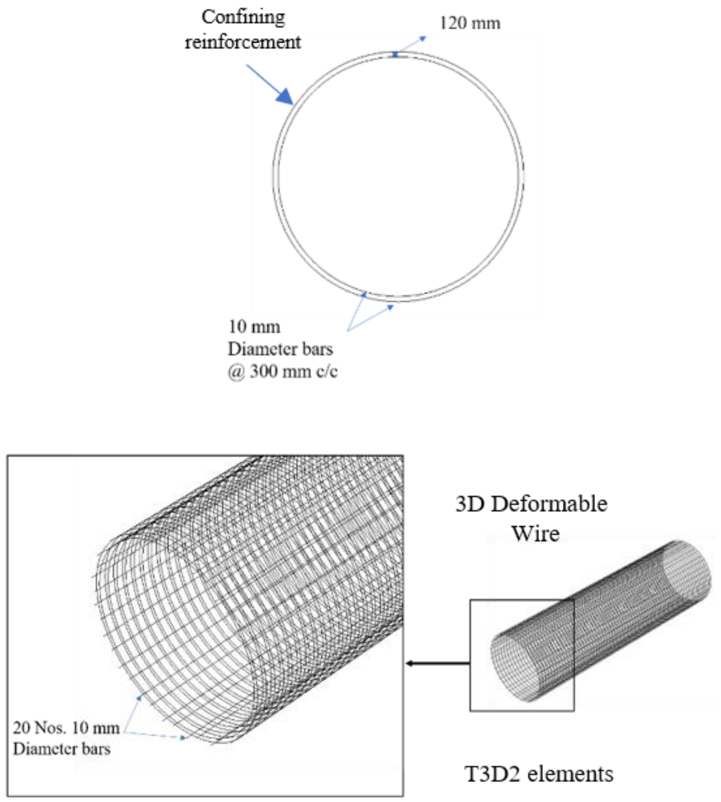

(c)
Figure 5.1 Details of FE model (a) Geometry in XY plane (All dimensions are in m) (b) Isometric view of model (c) Complete reinforcement details of RC tunnel

The FE meshing details of soil domain, tunnel lining, and GFRP layer are displayed in Figure 5.2. The concrete and soil components are modeled as 3D solid deformable parts and meshed using eight-node linear elements (C3D8R) with reduced integration, hourglass, and distortion control. Since, explicit method is utilized for the FE analysis, the first-order elements such as C3D8R can provide accurate results. The reinforcement bars are modeled as 3D deformable wires and meshed using two-node truss elements (T3D2). Embedded constraints are used between concrete lining and reinforcement bars to model perfect bond between the guest elements and host elements. The interaction between concrete lining and soil is simulated using general contact in ABAQUS/EXPLICIT [35]. The interaction behavior in normal direction is specified as hard contact and a penalty value of 0.2 is used for frictional contact in tangential direction. GFRP blanket is modeled using hexahedral continuum shell elements (SC8R). The interaction between GFRP and RC lining is modeled using cohesive behavior option in surface-to-surface contact algorithm. It is evident that in case of blast loading on GFRP strengthened RC structures, the failure takes place at concrete stratum instead of adhesive layer due to inferior properties of concrete under tension and shear [178]. Hence, the strain rate dependence of the adhesive layer has not been considered. The cohesive behavior of adhesive is modeled using the properties as given in Table 5.1. The base of soil medium is provided with fixed boundary conditions while, the vertical surfaces of soil medium are restrained against displacements normal to the surface. The blast loading is modeled using CONWEP tool in the interaction module of ABAQUS/EXPLICIT [35]. The CONWEP pressure is applied to the inner walls of tunnel. The inner face of tunnel is categorized into different regions. The first region near the point of explosion has a length of 1 m in longitudinal direction from the point of explosion. In this region, the pressure is applied as a normally reflected pressure. The subsequent regions have length of 1 m, 4 m, and 4 m respectively. The pressures acting in these regions are calculated based on angle of incidence of the line joining the point of explosion and the central point of each region.

Mesh convergence study is performed for the FE model as displayed in Figure 5.3(a). The number of elements in Figure 5.3(a) represent the total number of finite elements in the different components (soil, RC tunnel, steel reinforcement inside RC tunnel, and GFRP) as shown in Figure 5.2**.** For the mesh convergence study, the number of elements is increased by dividing the FE components into higher divisions, for example, in Figure 5.2(a) the number of elements along the cross-section of tunnels is changed from 50 to some other value. Higher number of elements are provided in every single trial and the influence of this refinement on the response (displacement) of tunnel is analyzed. Finally, a mesh configuration is selected such that further refinement has no significant influence on the accuracy of results. In this work, a higher mesh density is provided in the zone near to the point of explosion in order to attain desired accuracy. The mesh density is reduced away from the detonation center to assure the computational efficiency of FE model. The position of explosion and the key analysis points are displayed in Figure 5.3(b) and Figure 5.3(c) respectively. The values of displacement, velocity, and stress obtained at the specified points on the crown of tunnel lining, and top surface of soil domain are considered for comparative studies.

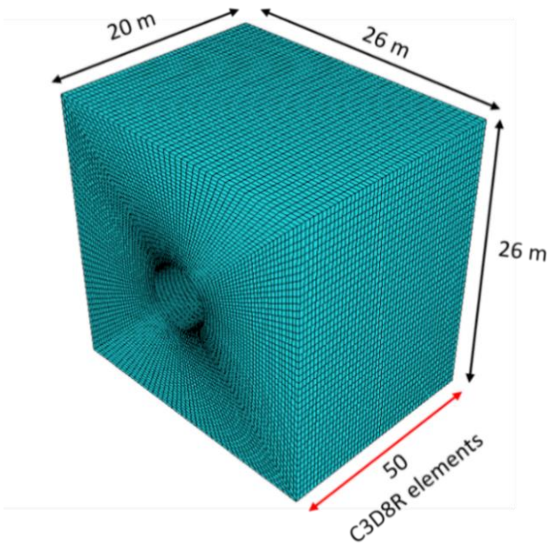

(a)

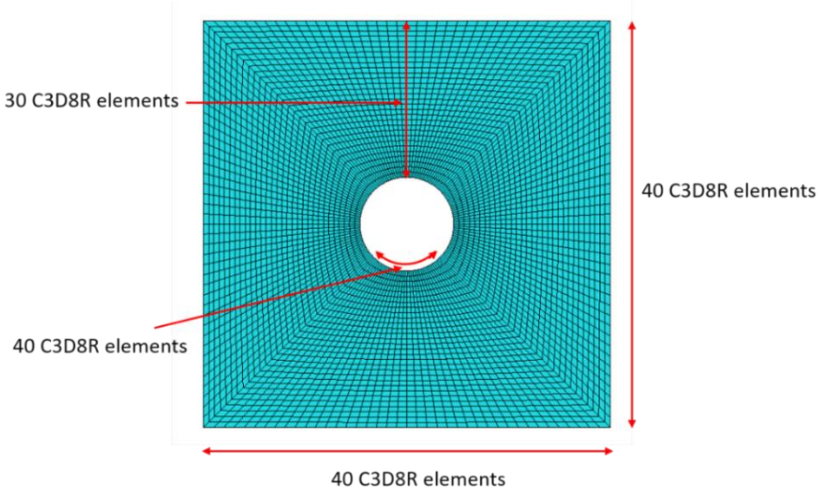

(b)

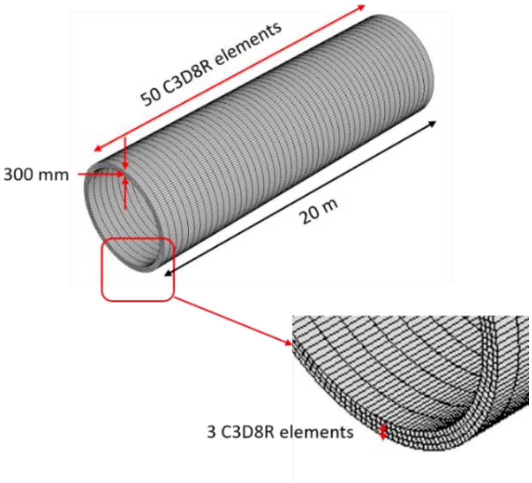

(c)

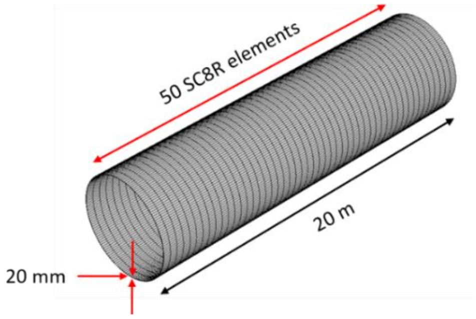

(d)

Figure 5.2 Meshing details of (a) Soil domain [Isometric view] (b) Soil domain [Front view] (c) RC tunnel and (d) GFRP blanket

Table 5.1 Adhesive properties for cohesive interaction between GFRP and RC tunnel

Properties	**Value**
Modulus of Elasticity	12.7 GPa [42]
Modulus of Rigidity	0.665 GPa [43]
Thickness (t)	0.1 mm (Assumed)
Coefficient of Thickness	$K_{nn}= 1.724 \times 10^{14}$ N/m^3 $K_{ss}= 6.65\times 10^{12}$ N/m^3 $K_{tt}= 6.65\times 10^{12}$ N/m^3
Cohesion	6 MPa [44]
Shear strength	2.84 MPa [43]
Fracture energy	900 N/m (Estimated)

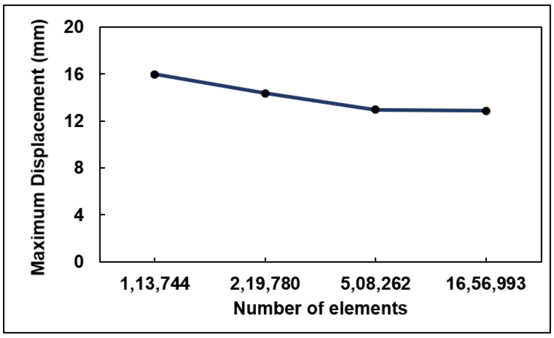

(a)

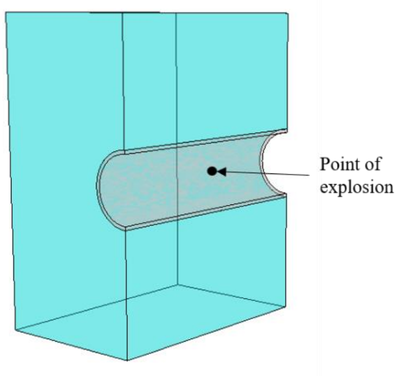

(b)

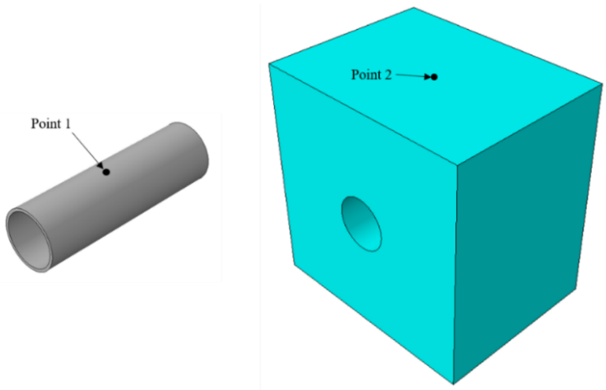

(c)

Figure 5.3 (a) Mesh convergence study (b) Location of explosion inside tunnel (c) Key observation points for analysis

5.2.2 Constitutive material modeling

5.2.2.1 Constitutive model of concrete

In the present work, the M50 grade concrete for tunnel lining has been modeled using CDP criteria. The details for this model have already been discussed in Section 2.3.3. The elastic properties of M50 grade concrete including the elastic modulus, poisson's ratio, and density value are taken as 35.36 GPa, 0.19, and 2400 kg/m^3 respectively. The yield function and the material parameters of CDP model are taken from Jankowiak and Lodygowski [158]. The uniaxial compressive as well as tensile input constitutive relationships of concrete for CDP model are shown in Figure 5.4. Since, in case of blast loading, structural elements including concrete show higher strength compared to static loading. The strain rate dependence of concrete is incorporated by defining the dynamic increase factor (DIF) under compression and tension. In this work, the DIF value in compression have been calculated using CEB-FIP Model Code [161] formulations, while the tensile DIF is calculated using the modified formulas of Malvar and Crawford [179]. The use of these two models have been found to produce accurate response of structural elements under blast loading in some studies [29, 180, 181]. A strain rate value of 100 s^{-1} is considered to prevent overestimation of strain rate effect [100, 180]. The DIF values are calculated as 2 and 6 respectively for compression and tension. These values match well with the values of DIF obtained using Bischoff and Perry [182], and UFC code [183] for a strain rate value of 100 s^{-1}. Additionally, the above obtained values have also been found to accurately predict the dynamic response of underground RC tunnels against blast loading [5, 100]. Hence, these values have been utilized for modifying the uniaxial compressive and tensile constitutive relationships of concrete.

5.2.2.2 Constitutive model of steel

The elastic-plastic behavior of steel is simulated using Johnson-Cook (J-C) model. The material parameters for Fe415 steel including the yield strength, density, elastic modulus, and poisson's ratio are taken as 415 MPa, 7800 kg/m^3, 200 GPa, and 0.3 respectively. The effects of temperature on the material properties are not considered. The effects of strain rate for J-C model have been adopted based on the test results reported in Goel et al. 2012, 2020 [5, 184]. The values are taken as A=360 MPa, B=635 MPa, n= 0.114, C= 0.075.

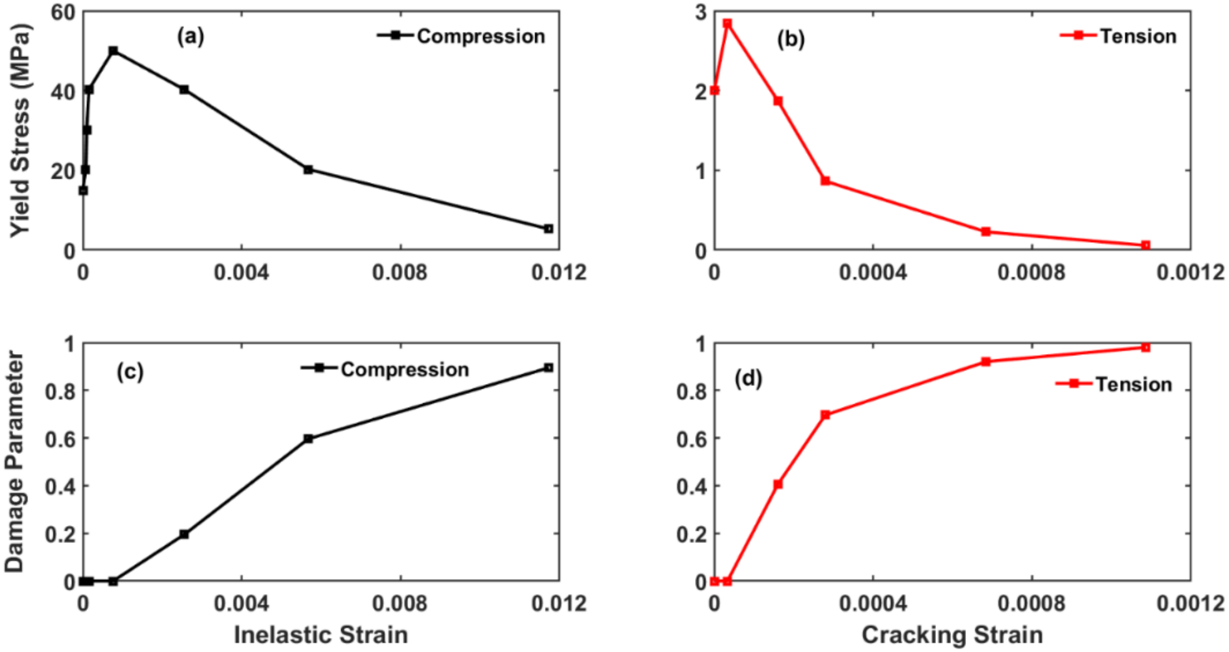

Figure 5.4 Uniaxial response of concrete in compression [a, c] and tension [b, d] for CDP model

5.2.2.3 Constitutive model of soil

In this work, the response of saturated and unsaturated clay has been modeled using Mohr-Coulomb plasticity model. These properties are obtained from Amli et al. [185], and Goel et al. [5]. For saturated soil, the elastic modulus, poisson's ratio, and cohesion values are taken as 40 MPa, 0.49, and 50 kPa respectively, while the friction and dilation angle are taken as 0º. For the unsaturated soil, the above values are 50 MPa, 0.3, 90 kPa, 20º, and 0º respectively.

5.2.2.4 Constitutive model of Glass Fiber Reinforced Polymer

The mechanical behavior of GFRP layer is simulated using anisotropic Hashin damage model. The properties of GFRP material are taken from Bhatnagar et al. [186], and Caliskan et al. [30], enlisted in Table 5.2. It is evident that the Hashin damage model is strain rate independent, however, blast loading phenomenon may result in development of high strain rates typically above the order of 1000 s^{-1} [187]. Hence, the effects of strain rate in GFRP material are accounted by using the dynamic increase factors. These enhancement factors have been obtained from the experimental results reported in previous literatures. The values of enhancement factors for tensile strength, and elastic modulus are considered close to 2 and 3 respectively [188, 189], while that for compressive strength, and shear strength are taken close to 1.30 and 1.37 [190, 191], respectively.

Table 5.2 Properties of GFRP material

Material properties	**Values**	
	Goel et al. [30, 186]	**Present study**
Elastic modulus in longitudinal direction, E_{11} (GPa)	48	138
Elastic modulus in transverse direction, $E_{22} = E_{33}$ (GPa)	10	10
Shear modulus, $G_{12} = G_{13}$ (GPa)	6	6
Shear modulus, G_{23} (GPa)	3	3
Poisson's ratio, $\upsilon_{12} = \upsilon_{13}$	0.3	0.3

Poisson's ratio, υ_{23}	0.42	0.42
Tensile strength in longitudinal direction, X^T (MPa)	988	2004
Compressive strength in longitudinal direction, X^C (MPa)	800	1197
Tensile strength in transverse direction, $Y^T = Z^T$ (MPa)	59	59
Compressive strength in transverse directio $= Z^C$ (MPa)	128	180
Shear strength in longitudinal direction, S^L (MPa)	92	137
Shear strength in transverse direction, S^T (MPa)	25	42
Fiber volume	54 %	54 %

5.2.3 Validation studies for 3D FE model

The validity of CONWEP tool utilized for modeling the blast response as well as the FE methodology incorporating CDP model for the analysis of internal blast loading on RC tunnels is verified. This is done by comparing the results with the (1) Experimental results of GFRP strengthened RC panels [192], (2) Numerical simulation results of blast analysis of RC tunnels reported by Goel et al. [5], and (3) Numerical simulation results of Phulari and Goel [29].

5.2.3.1 Validation of current FE methodology for modeling blast response of GFRP strengthened RC members using results of Tanapornraweekit et al. [192]

Tanapornraweekit et al. [192] performed experimental investigations for studying the response of GFRP strengthened RC slabs measuring 2000 mm × 1000 mm × 75 mm against blast loading. They considered a 0.45 kg explosive charge at a standoff distance of 0.5 m. GFRP sheets of thickness 2 mm are used at the top and bottom surface of RC slab to develop a sandwich scheme. The concrete utilized in RC slabs has a compressive strength of 32 MPa while the steel material utilized as reinforcement has a yield strength of 356 MPa. The GFRP laminates have an elastic modulus of 75.6 GPa, and tensile strength of 1330 MPa. The GFRP laminates are bonded to RC slab using epoxy material. In the current validation study, the RC slab, and GFRP laminates have been modeled using the same geometry, material properties, explosive charge, and standoff distance. The behavior of concrete is simulated using CDP model, reinforcing steel is modeled using J-C model, and the GFRP laminate has been modeled using Hashin damage model. The interaction between GFRP laminates and RC slab (epoxy) has been modeled using surface to surface contact algorithm utilizing the properties of epoxy material. The blast loading is simulated using CONWEP tool. All the components are meshed using 10 mm elements. The displacement time histories of non- and GFRP sandwiched RC slabs obtained from the present study are compared with the results of Tanapornraweekit et al. [192] as shown in Figure 5.5. The comparison of peak and residual displacement of RC slabs is presented in Table *5.3*. The damage profiles for the two types of slabs are also compared with the experimental damage profiles as shown in Figure 5.6 and Figure 5.7. The size of crater on the bottom face of RC slab is 197 × 281 mm, which is close to the crater size (200 × 300 mm) reported in experimental studies. Overall, the results from present validation study are in good agreement with the results of Tanapornraweekit et al. [192]. Hence, the current FE methodology utilized for modeling the response of GFRP strengthened RC members is considered to be validated.

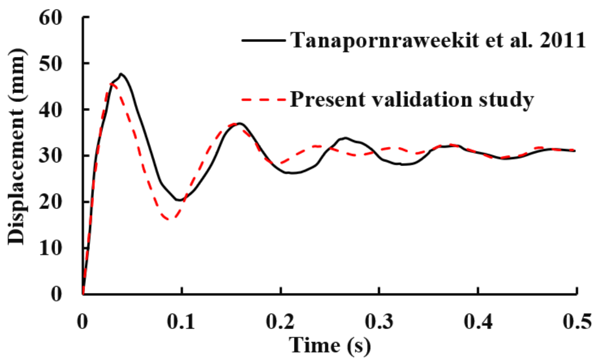

(a)

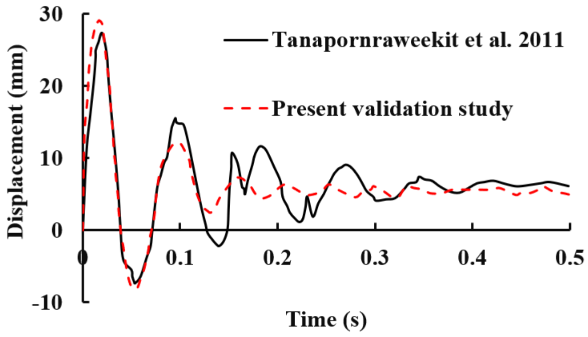

(b)

Figure 5.5 Displacement time histories for (a) RC slab (b) GFRP sandwiched RC slab

(a)

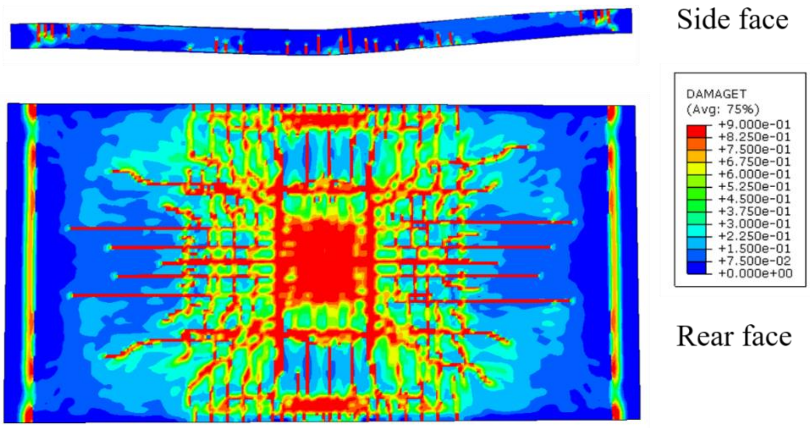

(b)

Figure 5.6 Damage pattern of RC slab (a) Tanapornraweekit et al. [192] (b) Present validation study

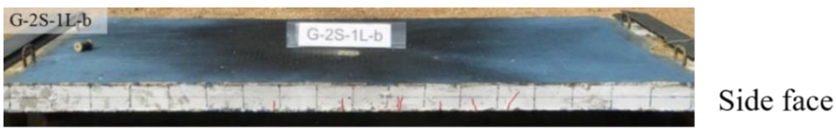

(a)

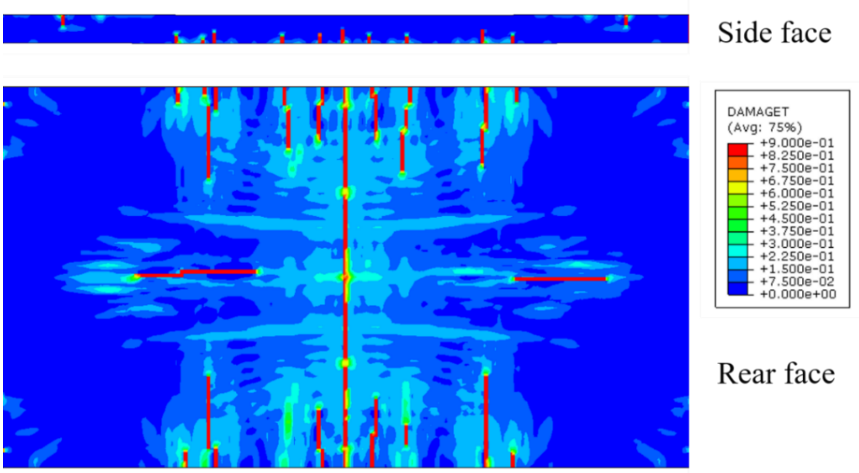

(b)

Figure 5.7 Damage pattern of GFRP sandwiched RC slab (a) Tanapornraweekit et al. [192] (b) Present validation study

Table 5.3 Comparison of peak displacement values with the results of Tanapornraweekit et al. [192]

Slab type	**Peak displacement (mm)**		**Residual displacement (mm)**	
	Tanapornraweekit et al. [192]	**Present validation study**	**Tanapornraweekit et al. [192]**	**Present validation study**
RC slab	47.6	45.4	31.5	31.3
GFRP sandwiched RC slab	27.3	29.1	6.1	5.4

5.2.3.2 Validation of current FE methodology for modeling blast response of underground RC tunnels using numerical simulation results of Goel et al. [5]

Further, the validity of FE model for solving complex problems related to internal explosion inside an RC tunnel is verified by comparing the results from present modeling approach with the numerical simulation results of Goel et al. [5]. Herein, a 20 m long circular RC tunnel with an internal diameter 5.4 m is considered to be embedded at a depth of 10 m inside soil domain measuring 20 × 26 × 26 m. The RC tunnel is 300 mm thick and surrounded by two different types of soil medium (saturated and unsaturated) and subjected to internal explosion of 100 kg at the center of tunnel. The RC tunnel comprises of M50 grade concrete and Fe-415 steel. For saturated soil, the elastic modulus, poisson's ratio, and cohesion values are 40 MPa, 0.49, and 50 kPa respectively, while the friction and dilation angle are 0º. For the unsaturated soil, the values are 50 MPa, 0.3, 90 kPa, 20º, and 0º respectively. The response of concrete, steel and soil is simulated using CDP model, J-C model, and Mohr Coulomb model, respectively. The blast loading is modeled using CONWEP tool. In the present study, similar geometric and material properties of soil domain and RC tunnel as well as the FE methodology are considered. The response is quantified in terms of displacement, velocity and stress values at concerned points. The displacement, stress, and velocity time histories at the crown of RC tunnel as well as the top middle node of soil surface obtained from present validation study and results of Goel et al. [5] are compared and the same is shown in Figure *5.8* and Figure *5.9*. Also, the comparison of peak displacement and stress values obtained at crown of RC tunnel and soil top surface are shown in Table 5.4. The time histories of displacement, velocity, and stress obtained in the present study for two different soil conditions comply well with the numerical simulation results. Also, it is observed that the peak values of displacement and stresses are predicted with a mean absolute error of 6.95 % and 14.2 %, respectively. Thus, the numerical simulation approach utilized in this work is considered to be validated.

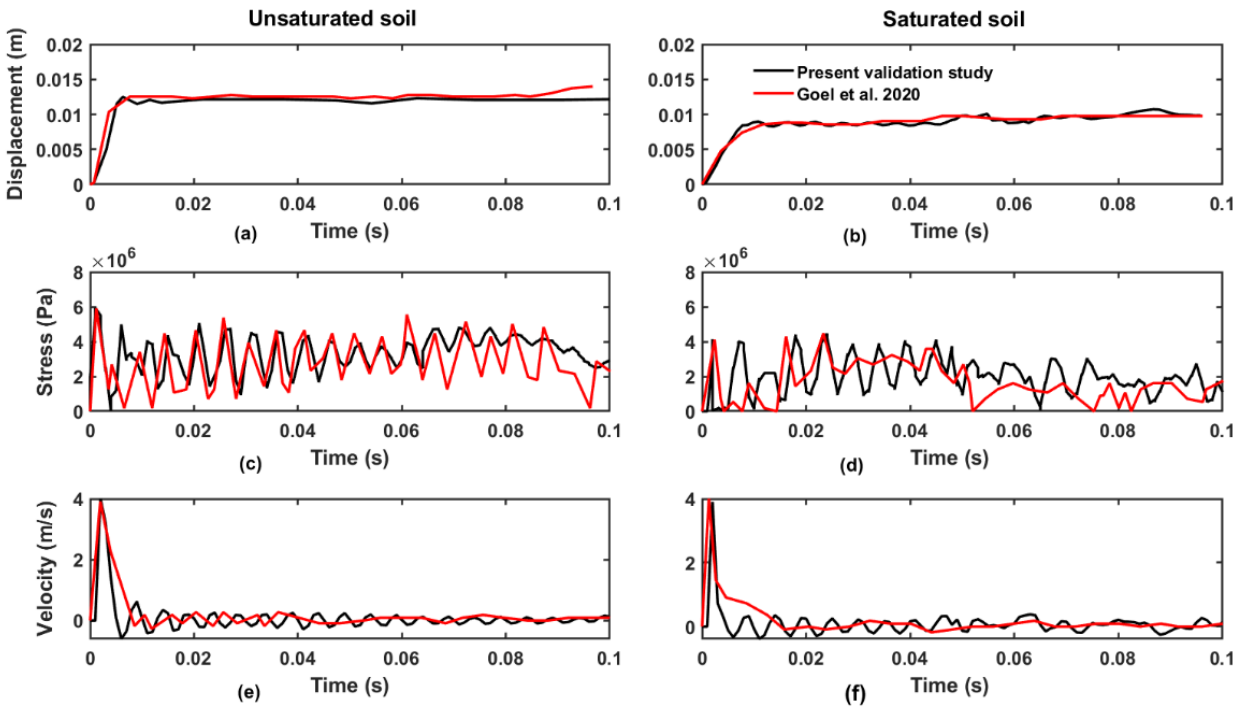

Figure 5.8 Comparison of displacement [(a), (b)], stress [(c), (d)], and velocity time histories [(e), (f)] at crown of RC tunnel with the results of Goel et al. [5]

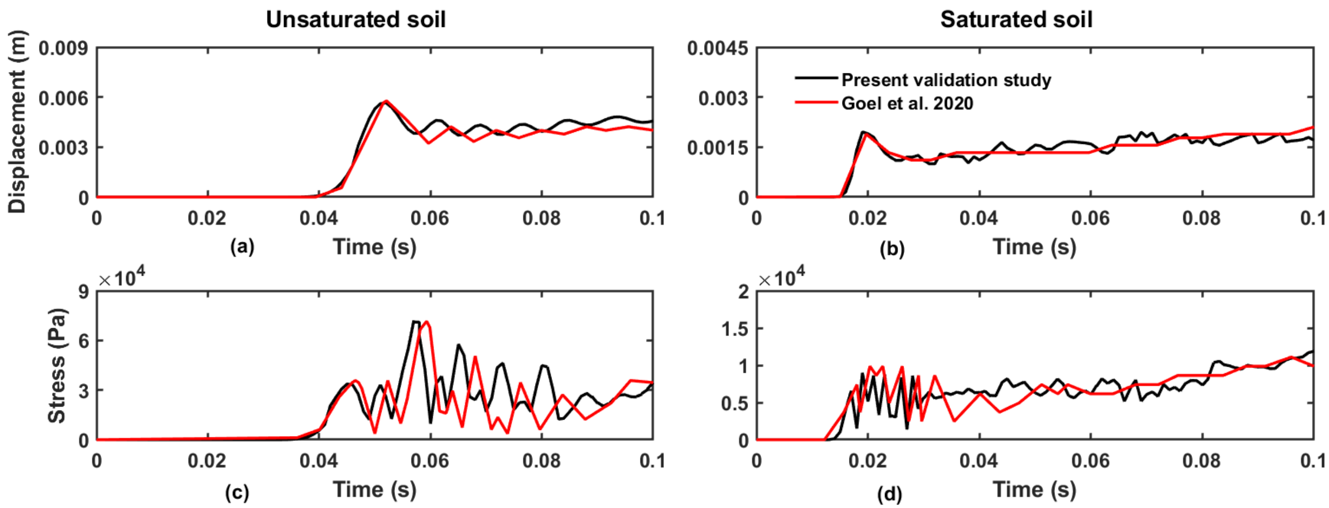

Figure 5.9 Comparison of displacement [(a), (b)], and stress time histories [(c), (d)] at top middle node of soil surface with the results of Goel et al. [5]

Table 5.4 Comparison of peak displacement and stress values with the results of Goel et al. [5]

Soil type	**Peak displacement (mm)**				**Peak Mises stress (Pa)**			
	Tunnel crown		**Soil top surface**		**Tunnel crown**		**Soil top surface**	
	Goel et al. [5]	**Present study**	**Goel et al. [5]**	**Present study**	**Goel et al. [5]**	**Present study**	**Goel et al. [5]**	**Present study**
Unsaturated	13.9	12.49	5.83	5.67	5971449	5910370	71820	72114
Saturated	9.93	10.65	2.11	1.955	4719404	4522040	10080	8920

5.2.3.3 Validation of current FE methodology for modeling blast response of CFRP strengthened RC tunnels using results of Phulari and Goel [29]

The FE methodology used for solving complex problems related to internal explosion inside a shielded RC tunnel is further verified by comparing the results from present modeling approach with the numerical simulation results of Phulari and Goel [29]. In this work, a 100 mm thick and 4 m long box shaped tunnel is considered to be embedded in soil bed at a depth of 1.5 m. The walls of tunnel are 800 mm apart. The RC tunnel comprises of a Fe-300 steel mesh having 8 mm diameter at 10 mm c/c spacing embedded in M20 grade concrete. The TNT explosive of 1.63 kg is used at a depth of 2 m below ground surface and at a horizontal spacing of 4 m from the tunnel wall. A 100 mm thick CFRP layer is used as a shielding over the tunnel wall. They have modeled the explosive charge using Jones-Wilkins-Lee (JWL) method, while the concrete and soil is modeled using CDP and Mohr-Coulomb model respectively. The CFRP material is modeled using strain cutoff failure criteria. The geometrical properties of the components are taken to be the same in the present validation study. Similar, to the work of Phulari and Goel [29], the response of concrete, and soil is modeled using CDP and Mohr-Coulomb model. However, for a better accuracy the response of CFRP material is simulated using Hashin damage model and its properties have been taken from Patnaik et al. [115]. Also, the blast loading is modeled using CONWEP tool considering a spherical type of explosive. The remaining properties have been used similar to those of Phulari and Goel [29]. The acceleration time histories obtained at the center of unshielded tunnel wall and the displacement profile of unshielded and shielded tunnel walls is shown in Figure 5.10. It can be observed that the acceleration values as well as the displacement profile obtained from the present validation study is in accordance with the numerical simulation results of Phulari and Goel [29]. Also, the peak values of acceleration and displacement at the center of tunnel are reproduced with an error of 11.63 % and 16 %, respectively. Thus, the current FE methodology used for simulating the response of FRP shielded underground RC tunnels under explosive loading is considered to be validated.

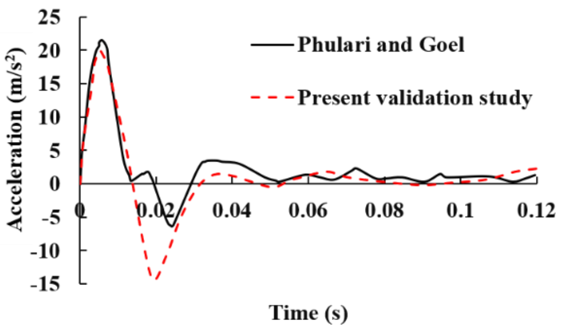

(a)

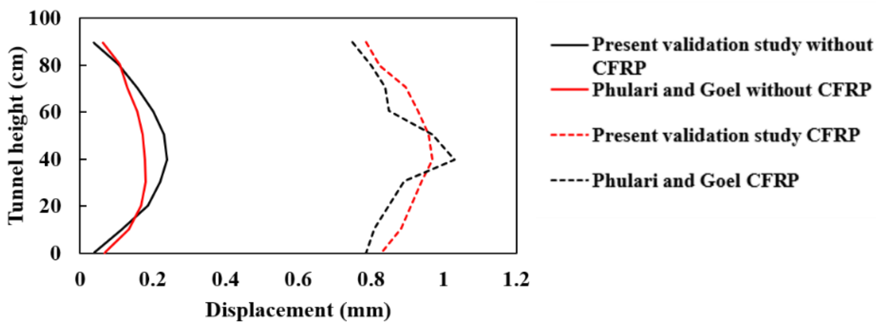

(b)

Figure 5.10 Comparison of (a) acceleration time histories and (b) tunnel displacement

5.3 Results of Finite Element Analysis

In this work, the blast investigation of subsurface RC tunnels is carried out by considering different cases which include: RC tunnel lining with and without GFRP protective layer, two different soil conditions (saturated and unsaturated), and three different explosive charge weights (10, 50, 100 kg). In order to study the response as well as to check the stability of tunnel in the surrounding soil medium, the analysis is done for an explicit time of 100 ms.

The displacement, stress, and velocity time histories at point 1 (crown tunnel, refer Figure 5.3(c) for TNT weights of 100 kg, 50 kg, and 10 kg are shown in Figure 5.11, Figure 5.12, and Figure 5.13, respectively. With the detonation of explosive charge, the velocity of tunnel increases suddenly and attains a peak value at about 1 millisecond, followed by tunnel displacement, development of stresses, and vibrations. The vibration of tunnel lining is not clearly observable from the plotted displacement time histories due to the consideration of large analysis duration and lower amplitude of tunnel vibrations. However, the tunnel vibrations are detectable by analyzing the noticeable fluctuations in stress values at the crown of tunnel. It can be clearly noted that the provision of GFRP layer curbs the fluctuation of stress values for different explosive charges which consequently results in reduced vibrations and damage of tunnel lining. The values of displacement, stress, and velocity at tunnel crown for saturated soil are lower with respect to unsaturated soil for all the considered explosive weights. This is due to the lower density, and higher angle of internal friction and cohesion of unsaturated soil. Also, the fluctuation of stress values in tunnel lining are lower for saturated soil. The peak displacement values of RC tunnel in saturated soil are approximately 15%, 30%, and 46% lesser with respect to that in unsaturated soil for 100 kg, 50 kg, and 10 kg explosive charges respectively. As a result, in the event of an internal blast, the RC tunnel surrounded by saturated soil will sustain lesser damage as compared to that in unsaturated soil. It is also observed that the provision of GFRP as protective layer curbs the displacement, stress, velocity values and the vibrations of tunnel due to dissipation of blast energy.

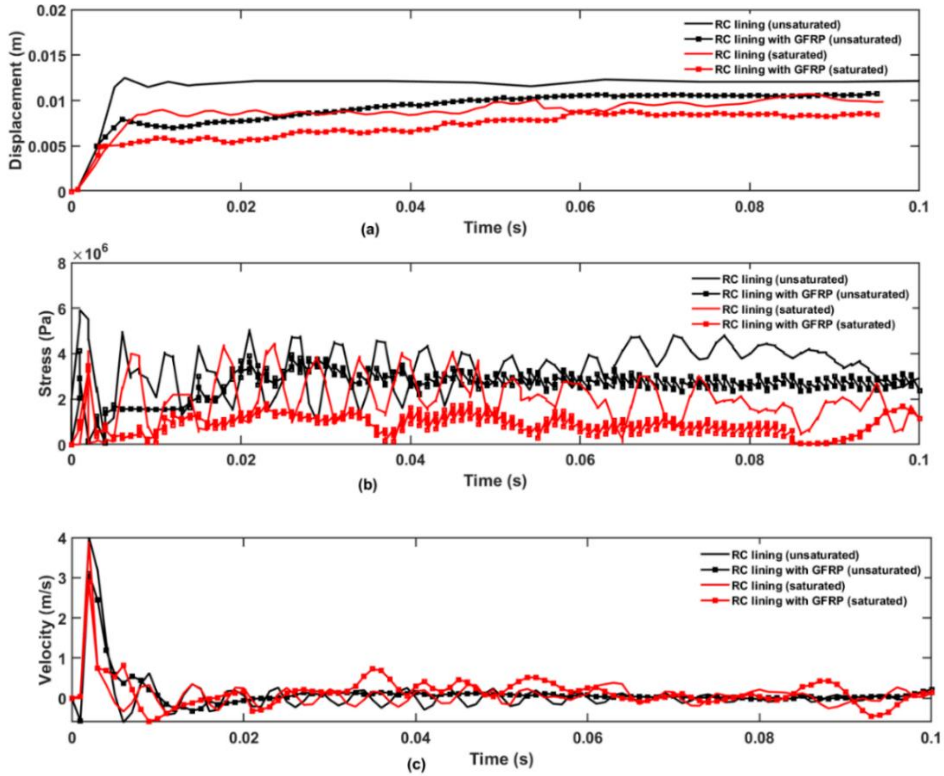

Figure 5.11 (a) Displacement (b) stress and (c) velocity time histories for RC tunnel against 100 kg explosive charge

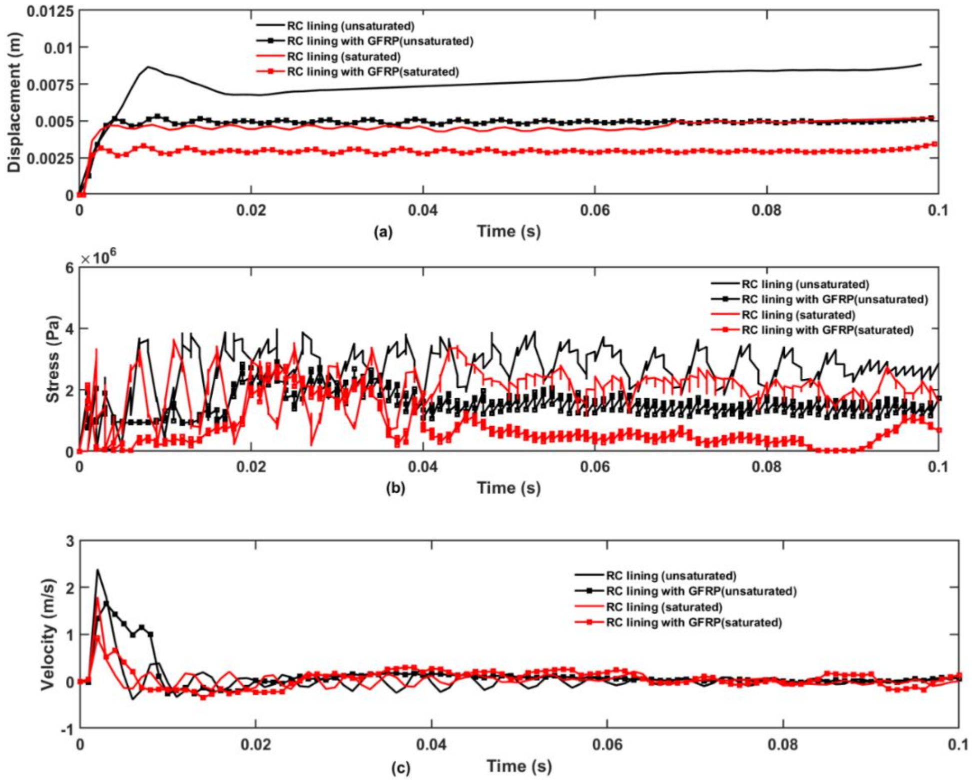

Figure 5.12 (a) Displacement (b) stress and (c) velocity time histories for RC tunnel against 50 kg explosive

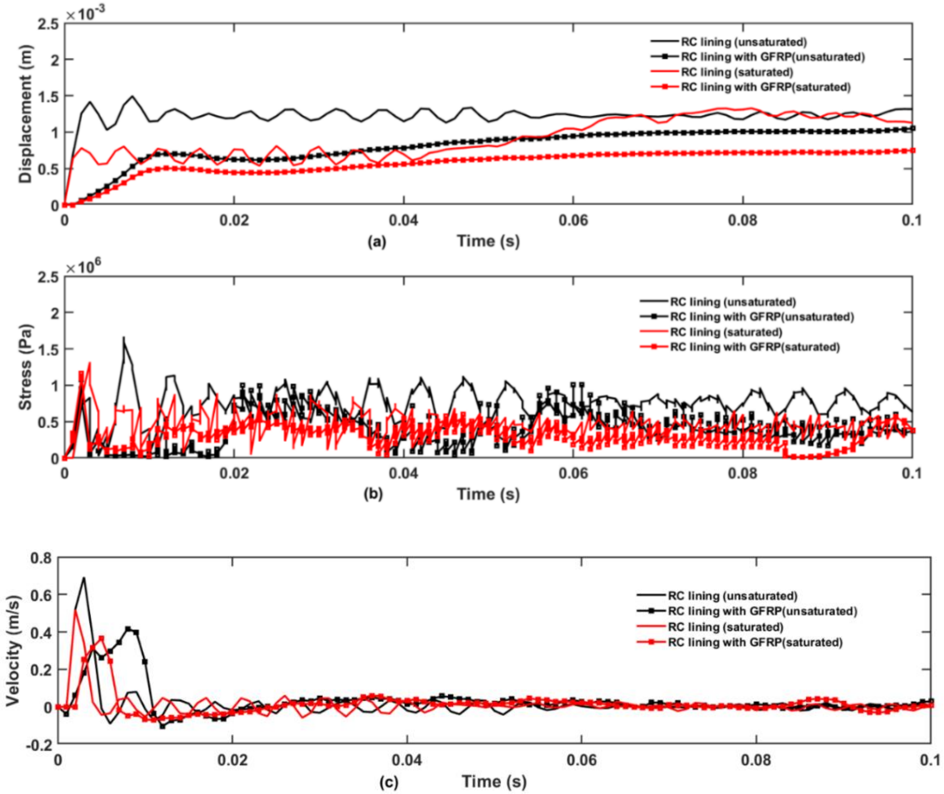

Figure 5.13 (a) Displacement (b) stress and (c) velocity time histories for RC tunnel against 10 kg explosive

The time histories of displacement and mises-stress at point 2 (ground surface, refer Figure 5.3(c) for 100 kg, 50 kg, and 10 kg TNT charges are shown in Figure *5.14*, Figure *5.15*, and Figure *5.16*, respectively. The propagation of stress waves in soil mass due to explosion inside tunnel results in long-term geotechnical effects such as liquefaction, and reduced soil shear strength around the foundation of a superstructure. This may eventually cause excessive settlement and damage of superstructure. Also, it may lead to complete failure due to footing rotation and bearing capacity failure. However, the GFRP layer effectively dissipates a high fraction of blast energy as a result of which the magnitude of pressure waves propagating in soil medium are reduced and hence lower values of stresses and displacements are observed at the ground surface. Also, the provision of GFRP protection effectively reduces amplitude of vibrations at the ground surface. Thus, the current methodology of utilization of GFRP as a protective covering over RC tunnel helps in improving the integrity of soil mass near ground surface in case of an underground explosion. Also, it reduces the risk of severe damage of the superstructure lying directly above the point of explosion at ground surface.

In addition to this, it can be noted that for the saturated soil, pressure wave reaches soil top surface earlier as compared to that in unsaturated soil. This is due to higher density of saturated soil. The peak displacement is also achieved earlier in saturated soil, however, the magnitude of displacement and stress is lower. The peak displacement, and peak stress values in saturated soil are approximately 60 % and 85 % lesser compared to that in unsaturated soil. A timelag is observed between the peak displacement values at crown of RC tunnel and the soil top surface. This timelag represents the time taken by pressure waves to traverse the soil medium.

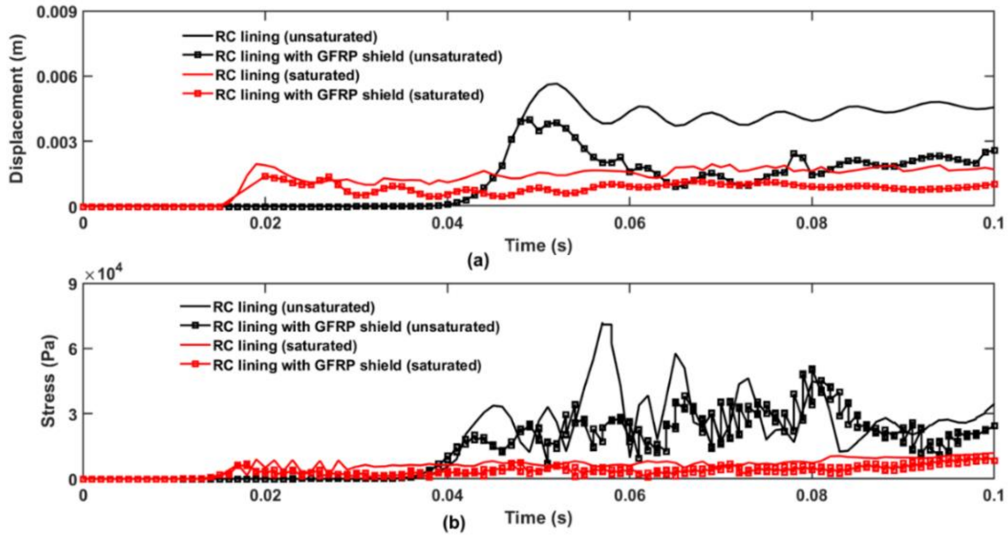

Figure 5.14 Time histories of (a) displacement and (b) stress at top middle node of soil surface due to 100 kg TNT explosion

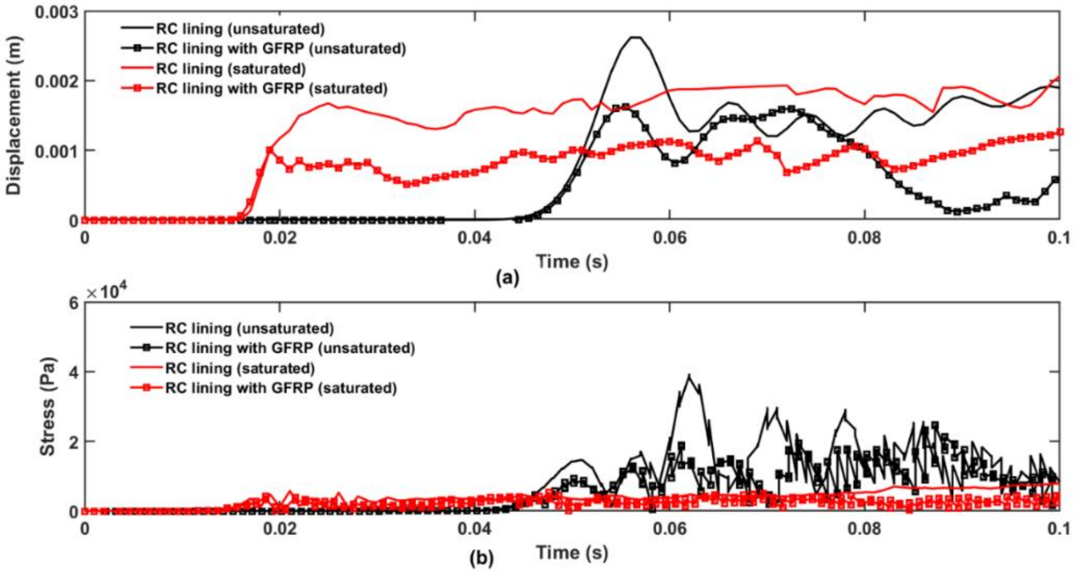

Figure 5.15 Time histories of (a) displacement and (b) stress at top middle node of soil surface due to 50 kg TNT explosion

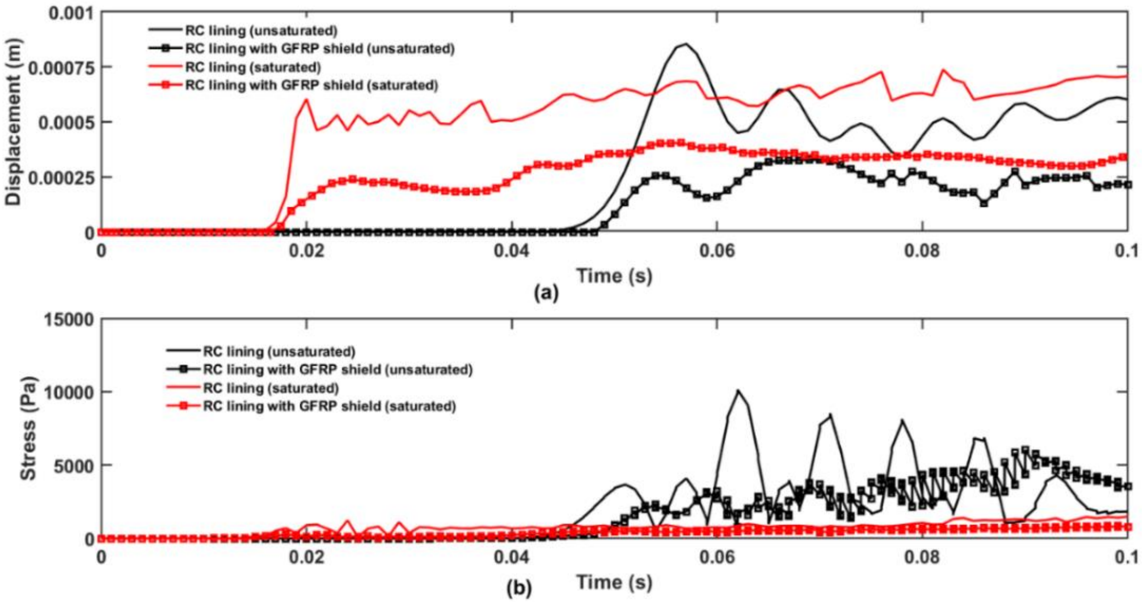

Figure 5.16 Time histories of (a) displacement and (b) stress at top middle node of soil surface due to 10 kg TNT explosion

5.4 Effect of GFRP layer on the response of RC tunnel under blast loading

5.4.1 Performance of RC tunnel under different explosive charges

5.4.1.1 100 kg explosive

The blast response of RC tunnel is quantified in terms of peak values of displacement, and Mises-stress at the crown of RC lining. The peak displacement contours, peak values of displacement and Mises stress for RC tunnels due to 100 kg explosive charge are shown in Figure 5.17. The Mises stress criteria has been used with equivalent stress in the element to check whether the concrete is fulfilling the resistance requirement on the application of load as suggested in previous literatures [115, 152, 193, 194]. It is observed that the higher tensile strength of GFRP layer results in absorption of blast energy consequently leading to reduced damage of RC tunnel. The use of GFRP layer reduces the peak displacement by 18 % and 20 % respectively for saturated and unsaturated soil, while the peak Mises stress value is reduced by 23.15 % and 30 % respectively for 100 kg TNT explosive.

The damage assessment of shielded and unshielded RC tunnels subjected to internal explosion is done using Equivalent plastic strain in tension (PEEQT) parameter. PEEQT is a scalar measurement which represents the plastic deformation of material in tension. Value of PEEQT greater than zero represents that the tensile yielding of material has already occurred. The PEEQT contours can be used to analyze which regions of concrete have failed/cracked in tension [195], as this parameter represents the initiation of plastic flow of the material. Figure 5.18 shows the PEEQT contours of RC tunnel without GFRP and with GFRP layer near the cross-section at the point of explosion at 1, 2, 5, and 10 ms. With the detonation of explosive charge, irregular peak displacements are observed and the propagation of stress wave starts in tunnel near the point of explosion which results in development of tensile stresses in tunnel lining consequently resulting in damage. These stress waves propagate longitudinally and simultaneously the damage propagation of RC tunnel also occurs. In addition to this, a portion of stress waves also push the soil in upward direction. Due to this the waves propagate through soil mass towards the ground surface, thus resulting in irregular peak displacement of ground surface. The sacrificial cladding layer of GFRP has a high tensile strength and energy dissipation capacity due to which it absorbs a major portion of blast energy before getting completely damaged and thus lower values of peak displacement are observed in the shielded tunnel linings. It can also be observed that strain values in RC tunnel decreases when GFRP layer of thickness 20 mm is used as shield over RC tunnel. The use of GFRP efficiently reduces the damage of RC tunnel and improves its performance under internal explosion.

The performance of RC tunnel with and without GFRP layer is further quantified by comparing the response of surrounding soil. The peak values of displacement and Mises stress at ground surface (point 2, refer Figure 5.3(c)) for 100 kg explosive is shown in Figure 5.19. The use of GFRP layer over RC tunnel lining dissipates a higher amount of blast energy as a result of which the magnitude of stress waves propagating in soil medium is reduced and lower values of stresses and displacements are observed at the ground surface. With the inclusion of GFRP protection, the peak displacement value at soil top surface is reduced by 29% and 31% respectively for saturated and unsaturated soil whereas, the peak Mises stress value is reduced by 16% and 30% respectively for the two types of soil.

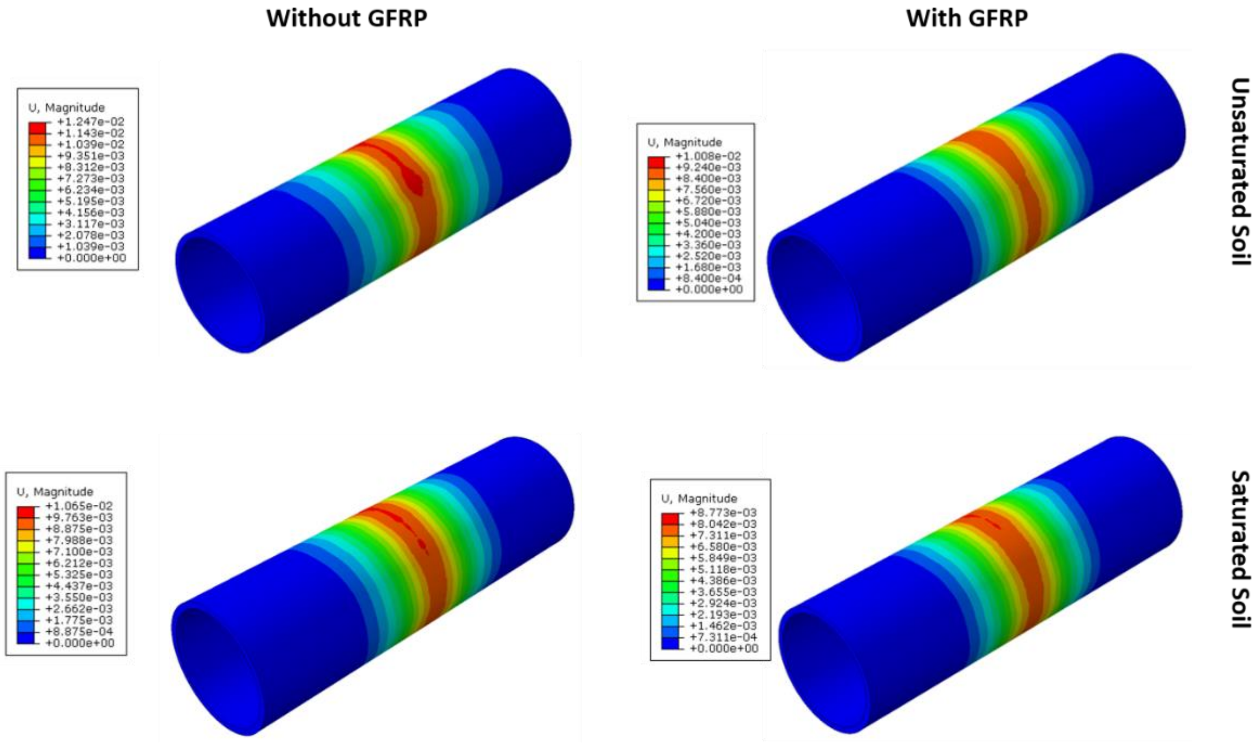

Without GFRP
With GFRP
Unsaturated Soil
Saturated Soil
U, Magnitude
+1.247e-02
+1.143e-02
+1.039e-02
+9.351e-03
+8.312e-03
+7.273e-03
+6.234e-03
+5.195e-03
+4.156e-03
+3.117e-03
+2.078e-03
+1.039e-03
+0.000e+00
U, Magnitude
+1.008e-02
+9.240e-03
+8.400e-03
+7.560e-03
+6.720e-03
+5.880e-03
+5.040e-03
+4.200e-03
+3.360e-03
+2.520e-03
+1.680e-03
+8.400e-04
+0.000e+00
U, Magnitude
+1.065e-02
+9.763e-03
+8.875e-03
+7.988e-03
+7.100e-03
+6.212e-03
+5.325e-03
+4.437e-03
+3.550e-03
+2.662e-03
+1.775e-03
+8.875e-04
+0.000e+00
U, Magnitude
+8.773e-03
+8.042e-03
+7.311e-03
+6.580e-03
+5.849e-03
+5.118e-03
+4.386e-03
+3.655e-03
+2.924e-03
+2.193e-03
+1.462e-03
+7.311e-04
+0.000e+00

(a)

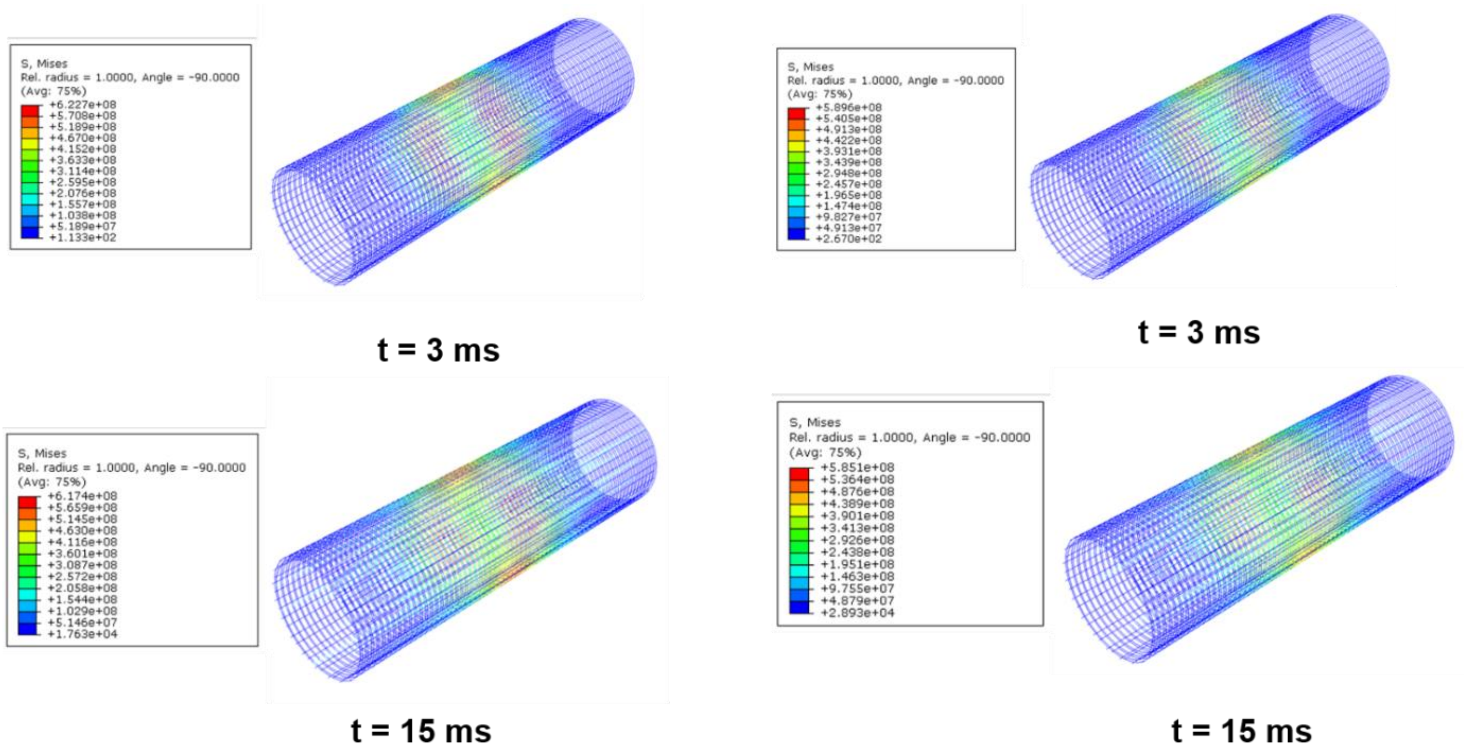
S, Mises
Rel. radius = 1.0000, Angle = -90.0000
(Avg: 75%)
+6.227e+08
+5.708e+08
+5.189e+08
+4.670e+08
+4.152e+08
+3.633e+08
+3.114e+08
+2.595e+08
+2.076e+08
+1.557e+08
+1.038e+08
+5.189e+07
+1.133e+02
t = 3 ms
S, Mises
Rel. radius = 1.0000, Angle = -90.0000
(Avg: 75%)
+5.896e+08
+5.405e+08
+4.913e+08
+4.422e+08
+3.931e+08
+3.439e+08
+2.948e+08
+2.457e+08
+1.965e+08
+1.474e+08
+9.827e+07
+4.913e+07
+2.670e+02
t = 3 ms
S, Mises
Rel. radius = 1.0000, Angle = -90.0000
(Avg: 75%)
+6.174e+08
+5.659e+08
+5.145e+08
+4.630e+08
+4.116e+08
+3.601e+08
+3.087e+08
+2.572e+08
+2.058e+08
+1.544e+08
+1.029e+08
+5.146e+07
+1.763e+04
t = 15 ms
S, Mises
Rel. radius = 1.0000, Angle = -90.0000
(Avg: 75%)
+5.851e+08
+5.364e+08
+4.876e+08
+4.389e+08
+3.901e+08
+3.413e+08
+2.926e+08
+2.438e+08
+1.951e+08
+1.463e+08
+9.755e+07
+4.879e+07
+2.893e+04
t = 15 ms

(b)

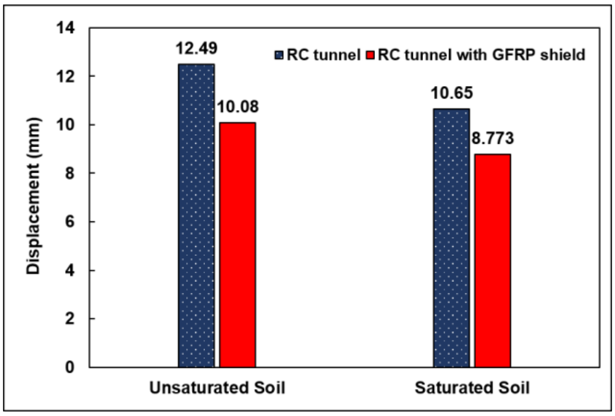

(c)

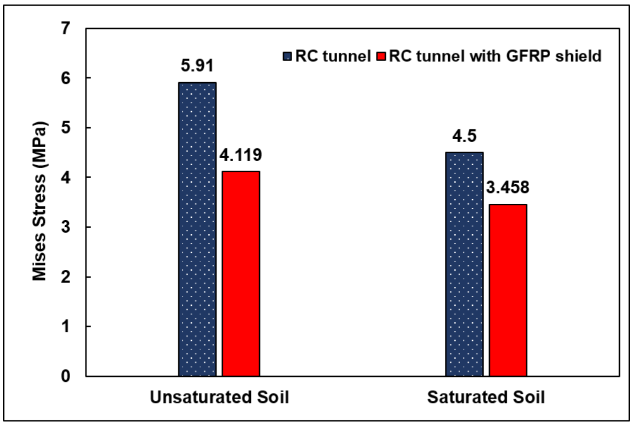

(d)

Figure 5.17 Peak (a) Displacement contours of tunnel, (b) Mises stress contours of reinforcement (c) Displacement and (d) Mises stress at RC tunnel crown for 100 kg explosion

RC tunnel **RC tunnel with GFRP shield**

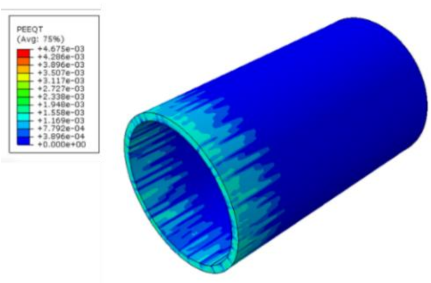

t = 1 ms

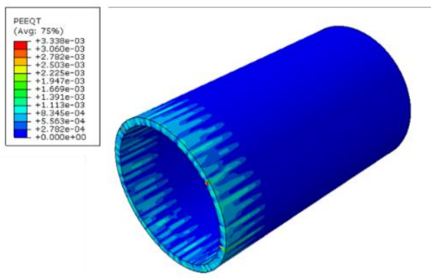

t = 1 ms

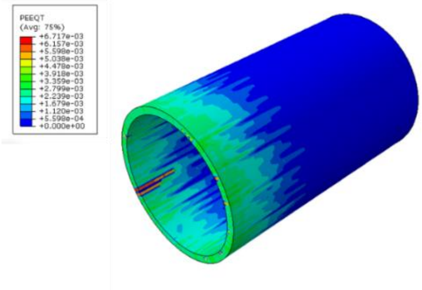

t = 2 ms

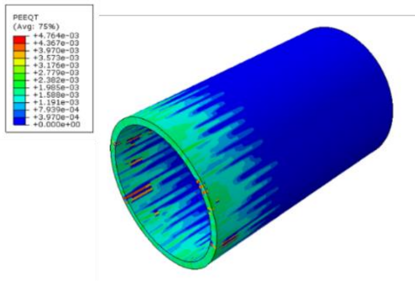

t = 2 ms

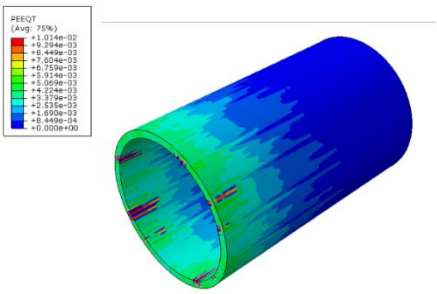

t = 5 ms

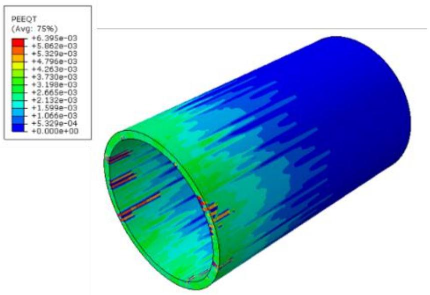

t = 5 ms

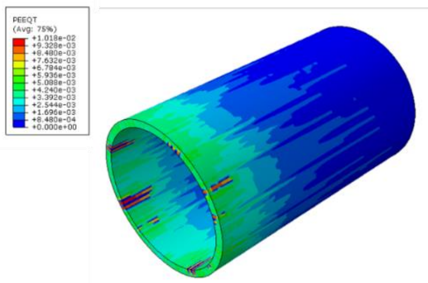

t = 10 ms

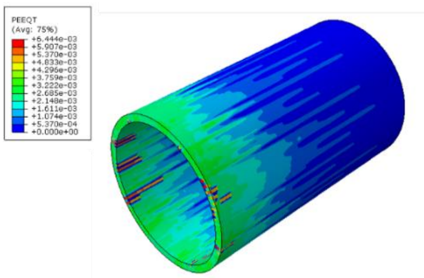

t = 10 ms

Figure 5.18 PEEQT contours of RC tunnel against 100 kg explosive

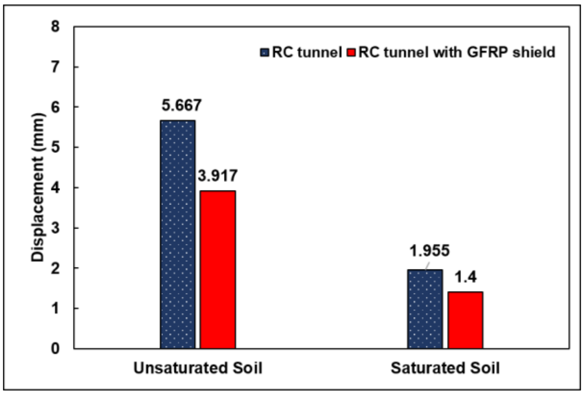

(a)

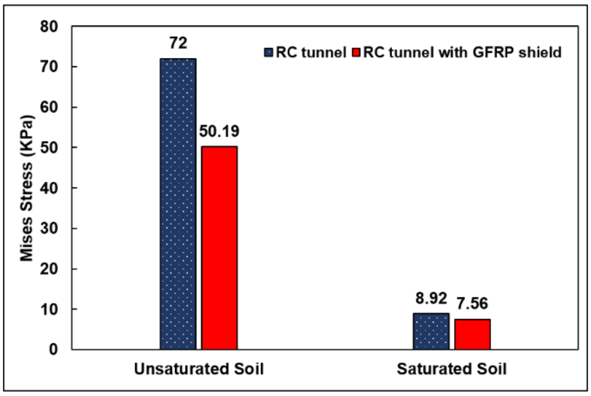

(b)

Figure 5.19 Peak values of (a) Displacement, (b) Mises stress at soil top surface for 100 kg explosion

5.4.1.2 50 kg explosive

The peak displacement contours, and the values of maximum displacement and Mises stress at the tunnel crown subjected to explosion of 50 kg are displayed in Figure 5.20. The use of GFRP layer reduces the peak displacement values by 34 % and 39 % respectively for saturated and unsaturated soil while the values of peak Mises stresses are reduced by 22 % and 28 % respectively for the two types of soils. The PEEQT contours of RC tunnel without GFRP and with GFRP protective layer at different time steps are shown in Figure 5.21.

The peak displacement and Mises stress values at ground surface (point 2, refer Figure 5.3(c)) due to 50 kg explosive are shown in Figure 5.22. The dissipation of a portion of blast energy by GFRP layer, reduces the peak displacement values at ground surface by 41% and 38% respectively for saturated and unsaturated soil, while the peak Mises stress values are reduced by 30% and 40 % respectively for the two types of soil considered.

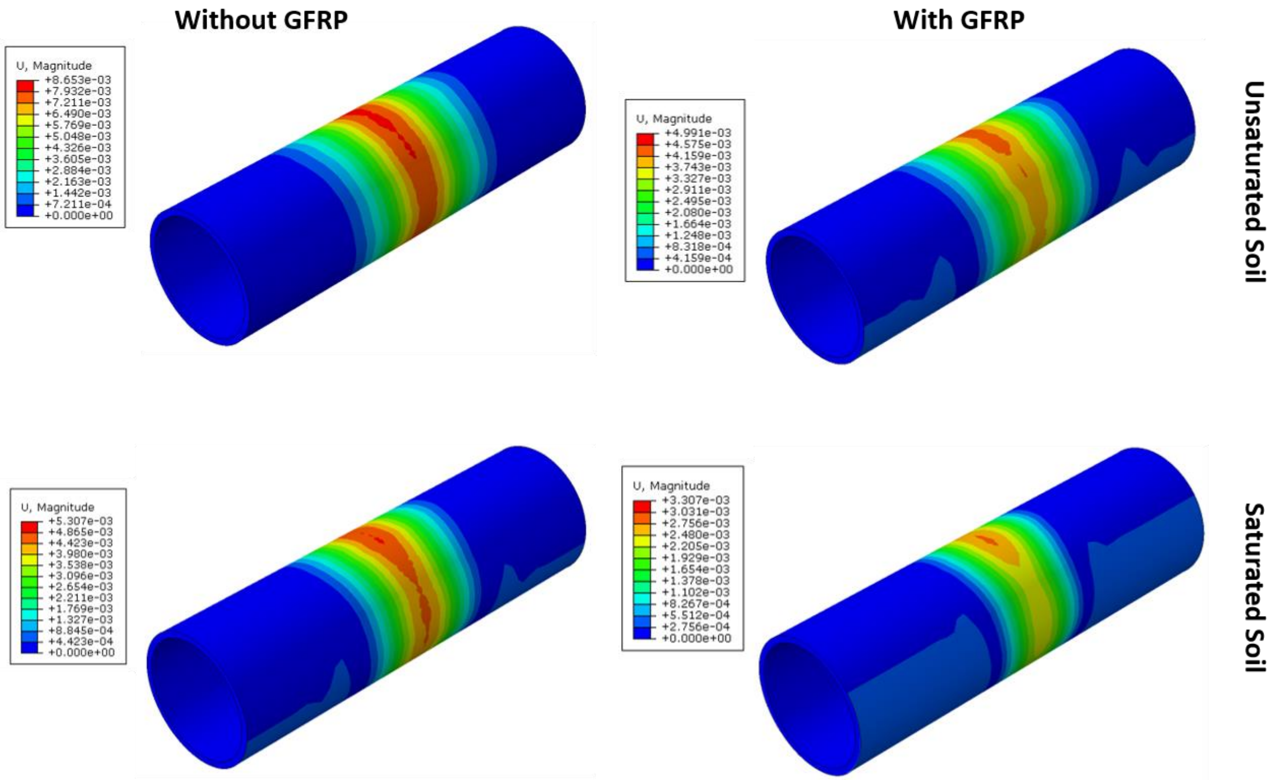
Without GFRP
With GFRP
Unsaturated Soil
Saturated Soil
U, Magnitude
+8.653e-03
+7.932e-03
+7.211e-03
+6.490e-03
+5.769e-03
+5.048e-03
+4.326e-03
+3.605e-03
+2.884e-03
+2.163e-03
+1.442e-03
+7.211e-04
+0.000e+00
U, Magnitude
+4.991e-03
+4.575e-03
+4.159e-03
+3.743e-03
+3.327e-03
+2.911e-03
+2.495e-03
+2.080e-03
+1.664e-03
+1.248e-03
+8.318e-04
+4.159e-04
+0.000e+00
U, Magnitude
+5.307e-03
+4.865e-03
+4.423e-03
+3.980e-03
+3.538e-03
+3.096e-03
+2.654e-03
+2.211e-03
+1.769e-03
+1.327e-03
+8.845e-04
+4.423e-04
+0.000e+00
U, Magnitude
+3.307e-03
+3.031e-03
+2.756e-03
+2.480e-03
+2.205e-03
+1.929e-03
+1.654e-03
+1.378e-03
+1.102e-03
+8.267e-04
+5.512e-04
+2.756e-04
+0.000e+00

(a)

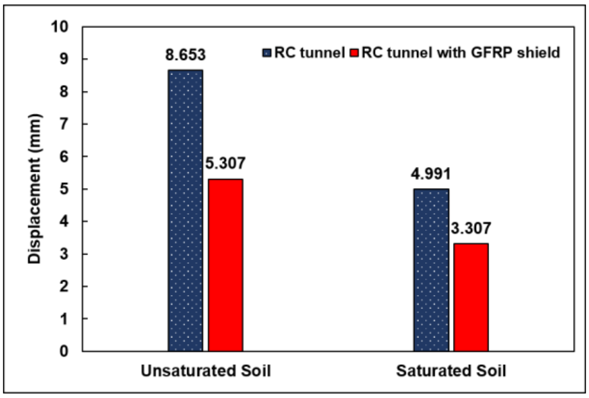

(b)

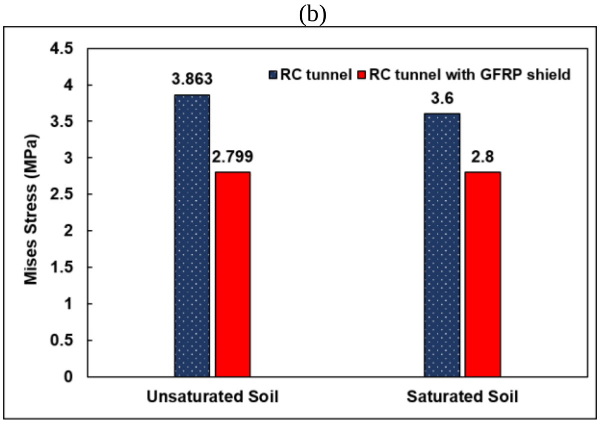

(c)

Figure 5.20 Peak (a) Displacement contours, (b) Displacement, and (c) Mises stress at RC tunnel crown for 50 kg explosion

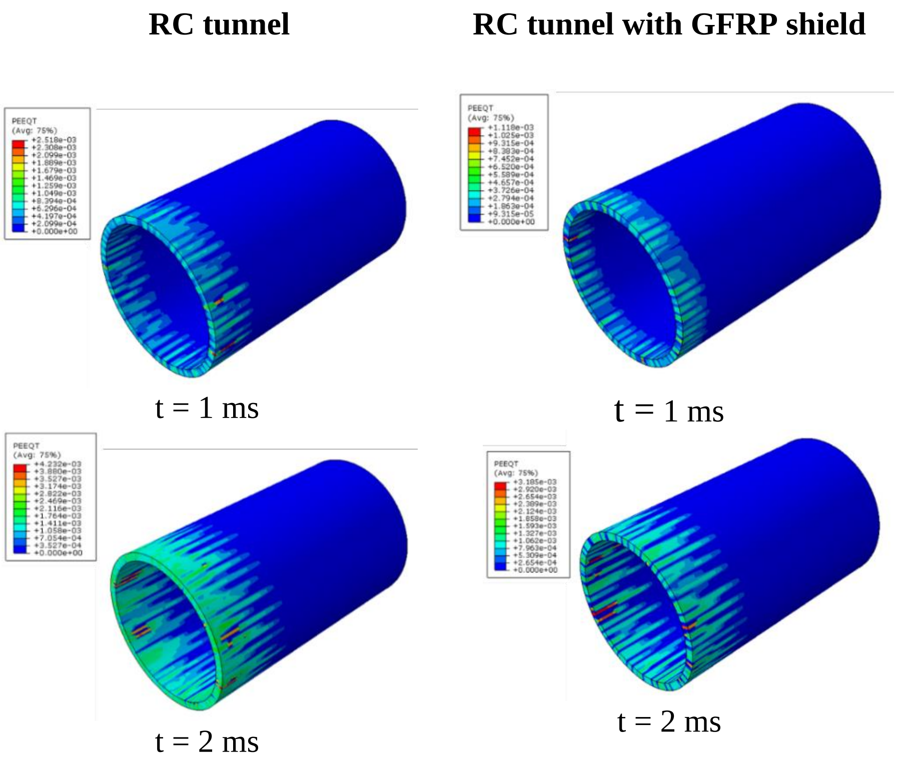

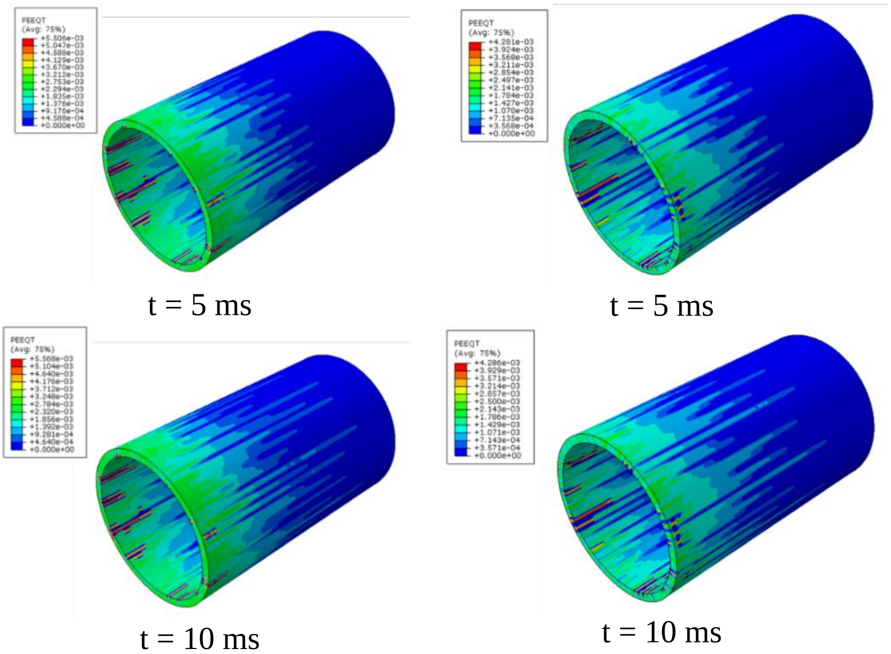

Figure 5.21 PEEQT contours for RC tunnel against 50 kg explosive

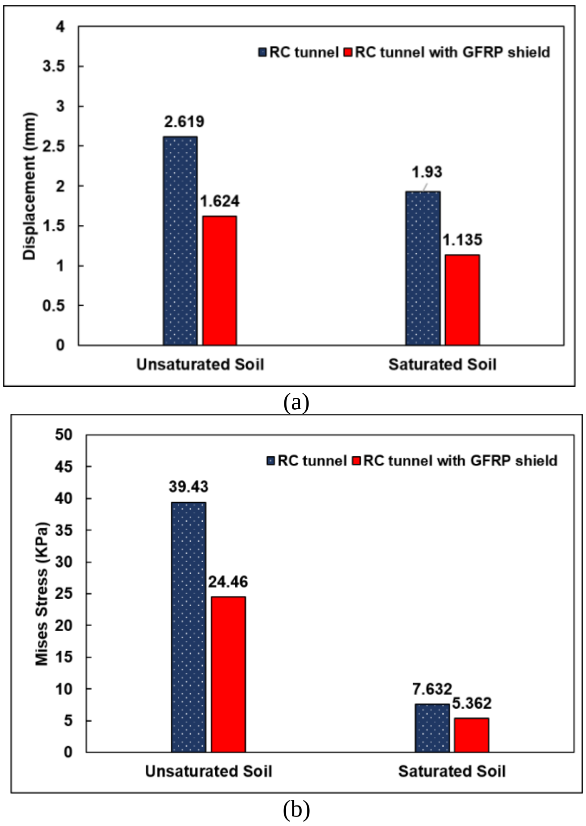

Figure 5.22 Peak values of (a) Displacement, (b) Mises stress at soil top surface for 50 kg explosion

5.4.1.3 10 kg explosive

The peak displacement contours as well as the values of maximum displacement and Mises stress at tunnel crown subjected to 10 kg explosion is shown in Figure 5.23. The utilization of GFRP protection curbs the peak displacement values by 46 % and 34 % respectively for saturated and unsaturated soil while the peak Mises stress values are reduced by 15% and 36% respectively for the two types of soils. The PEEQT contours of RC tunnel close to the point of explosion at different time instances for explosive charge of 10 kg are shown in Figure 5.24. The use of GFRP layer enhances the performance of RC tunnels subjected to 10 kg internal blast which is justified by the reduced values of plastic strains obtained near the point of explosion in shielded RC tunnels.

The peak values of displacement and stresses at point 2 (refer Figure 5.3(c)) of soil surface are shown in Figure 5.25. For 10 kg explosion, the peak values of displacement at soil top surface are reduced by 46% and 62% respectively for saturated and unsaturated soil while the peak values of Mises stress at soil top surface are reduced by 41% and 39% respectively for the two types of soil due to the presence of GFRP protective layer.

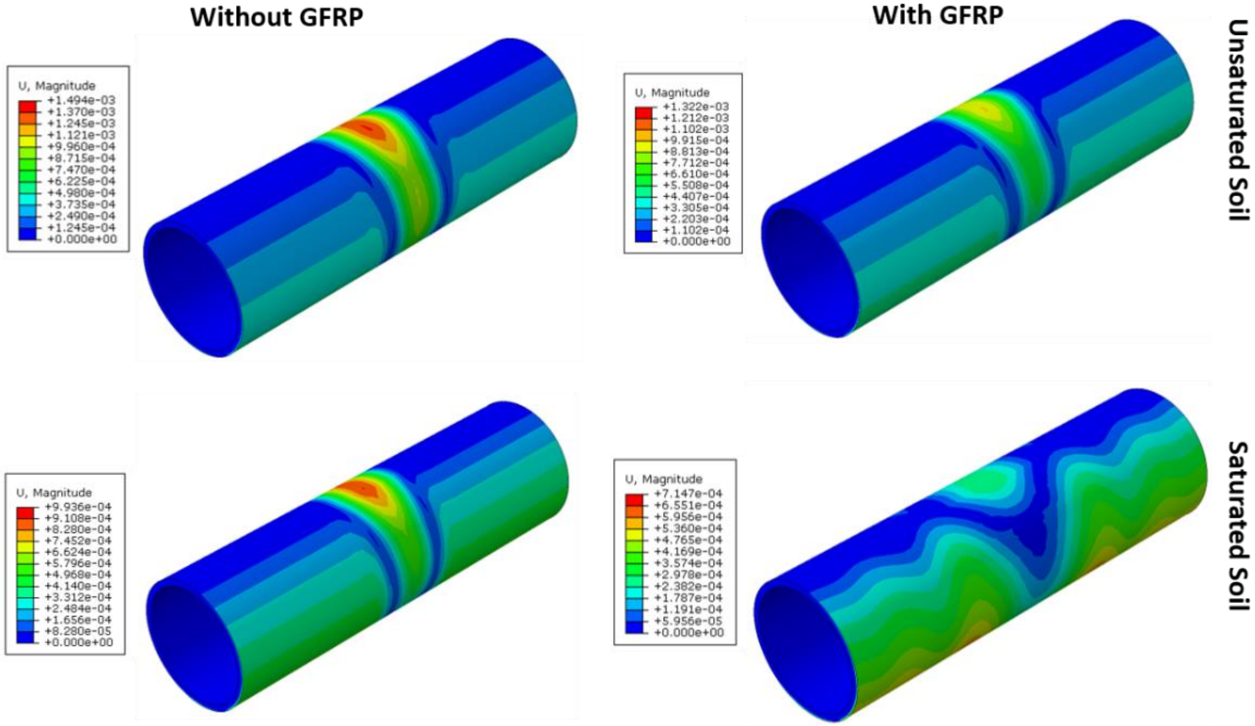
Without GFRP
With GFRP
Unsaturated Soil
Saturated Soil
U, Magnitude
+1.494e-03
+1.370e-03
+1.245e-03
+1.121e-03
+9.960e-04
+8.715e-04
+7.470e-04
+6.225e-04
+4.980e-04
+3.735e-04
+2.490e-04
+1.245e-04
+0.000e+00
U, Magnitude
+1.322e-03
+1.212e-03
+1.102e-03
+9.915e-04
+8.813e-04
+7.712e-04
+6.610e-04
+5.508e-04
+4.407e-04
+3.305e-04
+2.203e-04
+1.102e-04
+0.000e+00
U, Magnitude
+9.936e-04
+9.108e-04
+8.280e-04
+7.452e-04
+6.624e-04
+5.796e-04
+4.968e-04
+4.140e-04
+3.312e-04
+2.484e-04
+1.656e-04
+8.280e-05
+0.000e+00
U, Magnitude
+7.147e-04
+6.551e-04
+5.956e-04
+5.360e-04
+4.765e-04
+4.169e-04
+3.574e-04
+2.978e-04
+2.382e-04
+1.787e-04
+1.191e-04
+5.956e-05
+0.000e+00

(a)

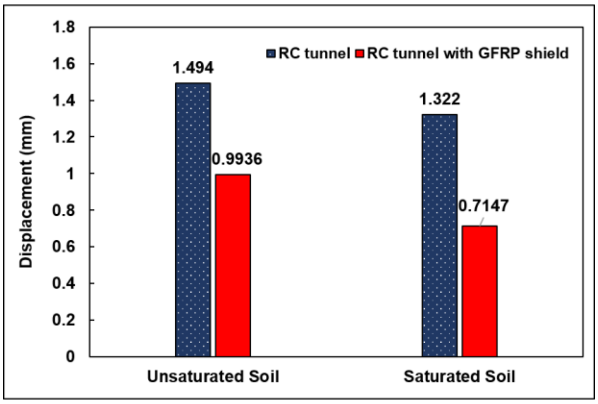

(b)

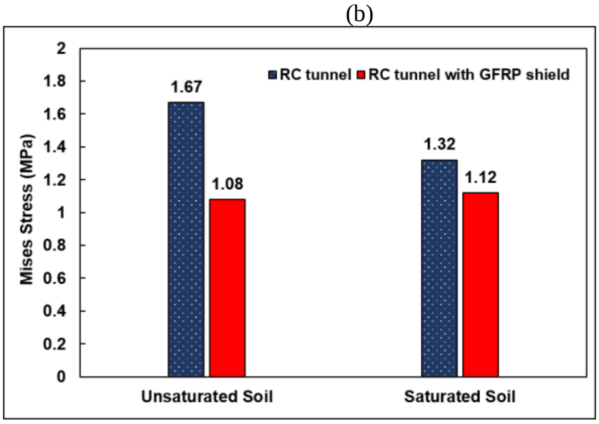

(c)

Figure 5.23 Peak (a) Displacement contours (b) Displacement and (c) Mises stress at RC tunnel crown for 10 kg explosion

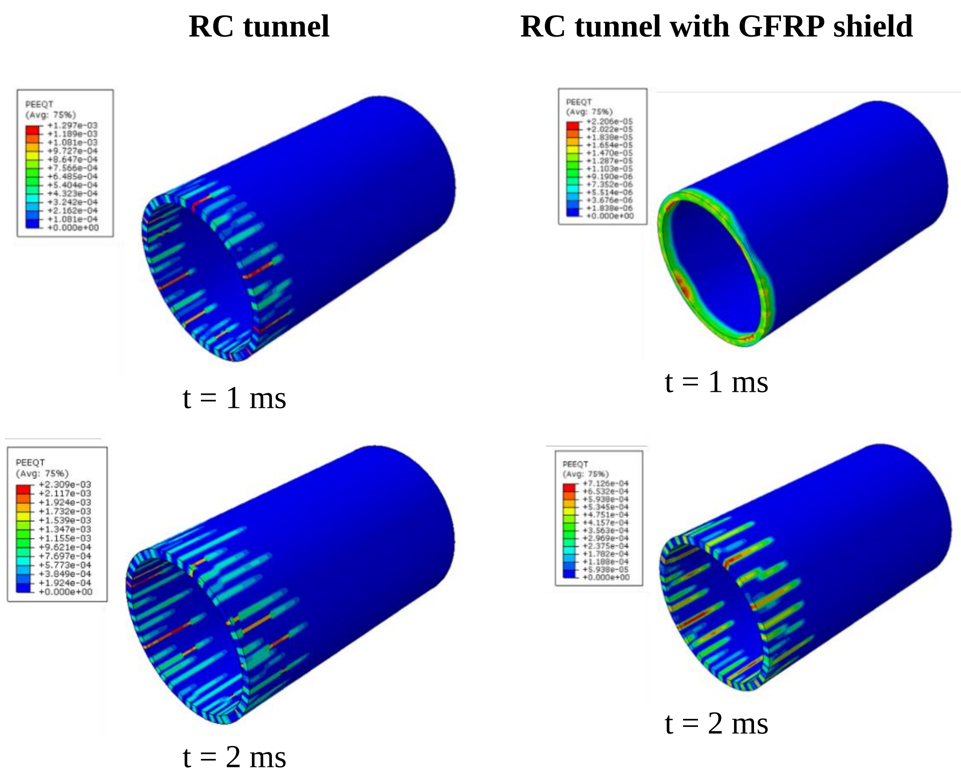

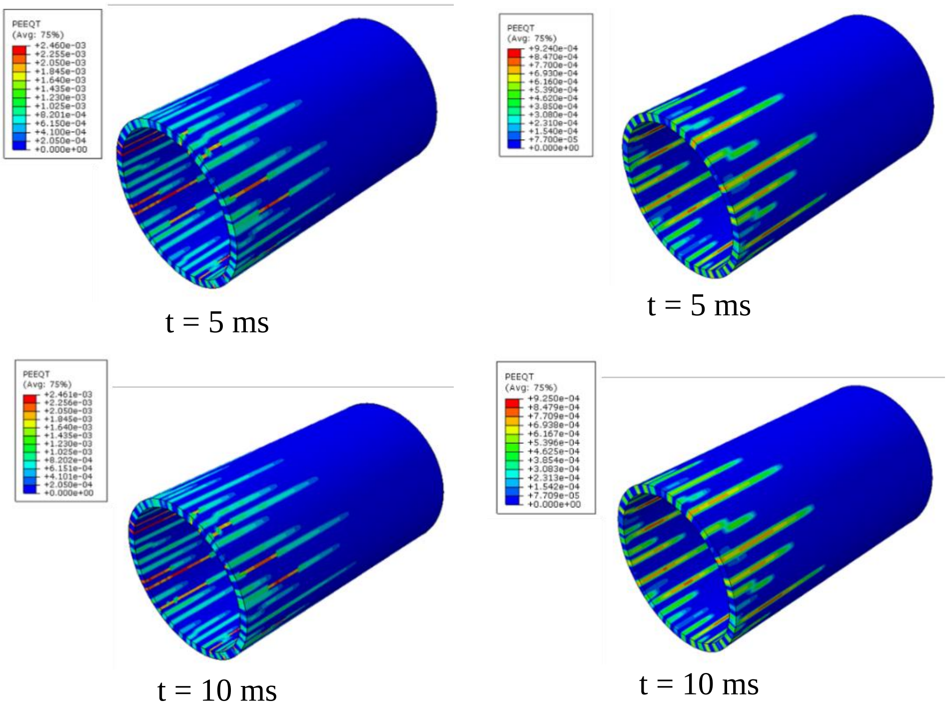

Figure 5.24 PEEQT contours for RC tunnel against 10 kg explosive

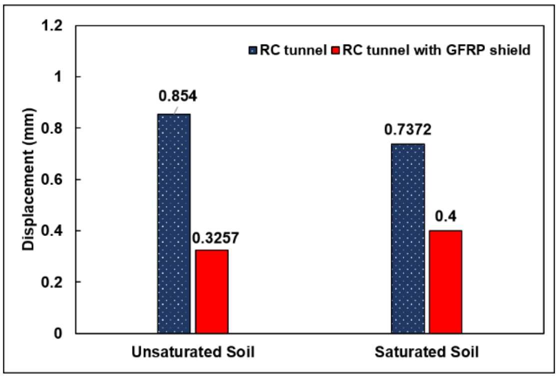

(a)

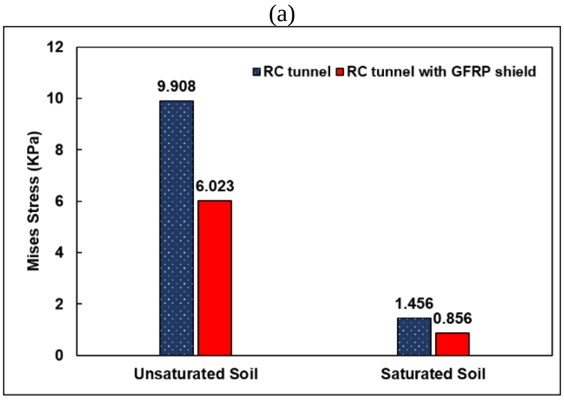

(b)

Figure 5.25 Peak values of (a) Displacement, (b) Mises stress at soil top surface for 10 kg explosion

5.4.2 Peak displacement at crown of RC tunnel for different explosive charges

The variation of peak displacement values obtained at the crown of RC tunnel are shown in Figure 5.26, which evidently illustrates the importance of charge weight on displacement of tunnel lining. The peak displacement value increases by approximately 800% as the explosive charge is increased from 10 kg to 100 kg. Considering, the damage which could be imparted by TNT explosive on the RC tunnel, the provision of GFRP shield is incorporated in the present study. The GFRP shielding reduces the peak displacement value by approximately 14% for 100 kg explosive, 35 % for 50 kg explosive, and 40% for 10 kg explosive.

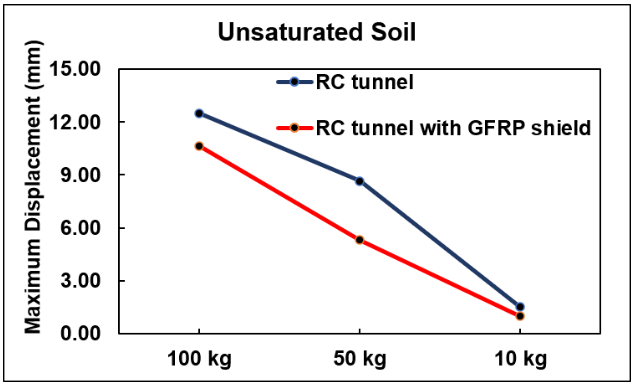

(a)

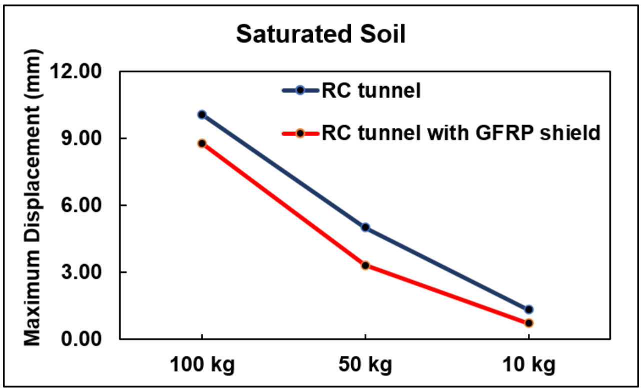

(b)

Figure 5.26 Variation of peak displacement in RC tunnel for different explosive weights (a) unsaturated soil (b) saturated soil

5.5 Summary

In this work, a novel concept has been proposed involving the use of GFRP layer as a protective shield for strengthening the RC tunnel lining against the impact of internal blast explosion. To this end, 3D nonlinear FE analysis of RC tunnels have been performed in two different types of surrounding soil medium, and subjected to three different TNT explosive charges of 10 kg, 50 kg, and 100 kg. The soil medium as well as RC tunnel is modeled using Lagrangian elements, while the internal blast is simulated using CONWEP method in ABAQUS/EXPLICIT.

The use GFRP layer as protective shield reduces the peak displacement, and stress values in RC tunnel. The peak values of displacement are reduced by approximately 14% for 100 kg explosive, 35% for 50 kg explosive, and 40% for 10 kg explosive. Also, the peak stress values are reduced by approximately 25% for 100 kg and 50 kg explosive, and 35% for 10 kg explosive. It curbs the fluctuations of stresses as well as the vibrations of tunnel due to propagation of stress waves produced by internal TNT explosion. Also, the use of GFRP shield curbs the damage and plastic strains induced in tunnel due to TNT explosion. Thus, it may be concluded that the provision of GFRP layer enhances the blast resistance of RC tunnel lining. The shielding effect of GFRP layer of 20 mm thickness is more significant for lower explosive charges. Considering the context of metro underground tunnels, they are more likely to be subjected to internal explosion of low explosive charges such as 10 kg which may be easily carried by terrorists inside the subway system. Thus, the present methodology can be easily utilized in metro underground tunnels for substantially improving safety and reducing the damage in case of an internal explosion.

Compared to conventional RC tunnel lining, GFRP shielded RC lining dissipates a higher proportion of blast energy due to which the magnitude of pressure waves traversing in soil medium are reduced and hence lower values of stresses and displacements are observed at the top surface of soil. Consequently, it also reduces the risk of long-term geotechnical effects such as liquefaction, and reduced soil shear strength around the foundation of a superstructure which may be responsible for excessive settlement, damage, and complete failure of superstructure.

The values of peak displacement and stresses in RC tunnel surrounded by saturated soil media are lower with respect to that in unsaturated medium. Thus, the surrounding soil medium considerably affects the blast response of RC tunnel. Also, the peak values of displacement and stresses at top surface of soil are obtained earlier in saturated soil compared to that in unsaturated soil. However, the magnitude of peak displacement and stresses is higher for unsaturated soil.

Chapter-6

Artificial Intelligence (AI) in the prediction of blast induced damage in subsurface Reinforced Concrete tunnels

6.1 Introduction

Underground structures such as tunnels, pipelines, basements, bunkers, etc play a key infrastructural role in the present era. Among the different types of underground structures, tunnels are widely utilized as public transport subway system. However, due to huge population in a limited space, these are highly prone targets to terrorist attacks. The recent explosive events in underground subways of different cities have brought attention towards the damage forecasting and remedial measures necessary for reducing the consequence of such events. Till date, several studies have carried out damage assessment and dynamic analysis of underground structures and soil against blast loading [5, 88, 95–97, 102, 103, 107]. Additionally, some of the studies also focused on exploration of methods through which safety of tunnels could be improved. In general, the use of a sacrificial layer has been found to reduce the stresses and velocity of tunnel linings in case of blast loading [25, 108].

With the recent advancement in computational techniques and evolution of new material constitutive models, numerical methods such as finite element (FE) have been widely used to perform dynamic analysis of complex problems. Although, the blast analysis of subsurface tunnels can be performed well using numerical techniques, they offer several challenges such as the consideration of effects of post peak dynamic behavior, mesh dependency, contact interaction between two surfaces, immense modeling work, and computational expenses. In short, the numerical blast analysis of RC tunnels is a complicated task with high computational expenses. Also, it is not possible to conduct sensitivity analysis, and parametric studies if wide range of input variables are present. Thus, there is a need to establish a predictive methodology with the accuracy of numerical methods and low computational expenses of semi-empirical methods which could be utilized for detailed blast analysis of subsurface RC tunnels.

Artificial Intelligence (AI) is suitable for accomplishing the objective discussed above. Fully trained AI models are very useful for rendering and establishing highly complex problems with numerous parameters and have the capability to give new predictions and perform a detailed analysis. Nowadays, AI is being widely utilized in civil and infrastructural engineering [31–33, 118, 119] as it demands lesser effort, easier implementation and low computational expenses from the user. It has been used for optimization of parameters in infrastructural applications [120], as well as for detection of clogging in pipejacking operations [121]. Additionally, it has been utilized for forecasting different parameters in civil engineering applications [122–127]. Recently, AI techniques have also been investigated for predicting the performance of RC structural members against blast loading [128–131]. Thus, the use of AI has been widely explored in the literatures.

Despite a lucid application of AI, its use for predicting the response of subsurface RC tunnels under internal explosion remains unexplored. In this work, Artificial Intelligence (AI) models have been explored for predicting the maximum displacement at the crown of RC tunnels under internal explosion. In order to achieve this objective, a 3D-FE model is developed using ABAQUS/EXPLICIT [35]. GFRP is used as a protective layer over RC tunnel in order to minimize the blast induced damage. The results of FE simulations obtained by varying the parameters are used to build datasets which are consequently used for establishment of prediction models. Since, the input and output correlations are highly non-linear and the dataset related to these problems may be scattered. Hence, in the current study, artificial neural networks (ANN), support vector machines (SVM), and random forests (RF) prediction models are utilized. These models have the capability to solve highly sophisticated non-linear problems with scattered datasets

[126, 129, 146]. The performance of these models is evaluated using statistical parameters such as Root Mean Square Error (RMSE), Coefficient of Determination (R^2), Mean Absolute Error (MAE), Mean Absolute Percentage Error (MAPE), and Variance accounted for (VAF). Finally, an efficient machine learning model is selected which can be used for damage assessment as well blast resistant design of RC tunnels.

6.2 Proposed methodology

The present work has been divided into two phases: in the first phase, a 3D-FE model of underground RC tunnel is developed in ABAQUS/EXPLICIT [35]. GFRP material is considered as a protective layer in order to improve the blast resistance of underground RC tunnels. The response of different components is simulated utilizing separate material models while the blast loading is simulated using CONWEP tool. Several input parameters such as GFRP thickness, characteristic compressive strength of concrete, yield tensile strength of steel, TNT charge, RC tunnel thickness and surrounding soil parameters such as modulus of elasticity, cohesion, and friction angle are considered. These parameters are varied discretely for each sample and a total number of 192 samples of RC tunnel with and without GFRP layer are generated. The output (peak displacement at tunnel crown) for each sample is determined using FE analysis. The flowchart of the proposed approach is shown in Figure 6.1.

In the second phase, the generated database is used to develop three AI models (ANN, SVM, and RF) for predicting the peak displacement values at the tunnel crown. The performance of these models is evaluated using five assessment metrics: root mean square error (RMSE), coefficient of determination (R^2), mean absolute error (MAE), mean absolute percentage error (MAPE), and variability account for (VAF) which are calculated using Eqs. (2.46) to (2.50). Finally, the model exhibiting best performance is selected which could be effectively utilized for quick damage assessment as well as blast resistant design of underground RC tunnels.

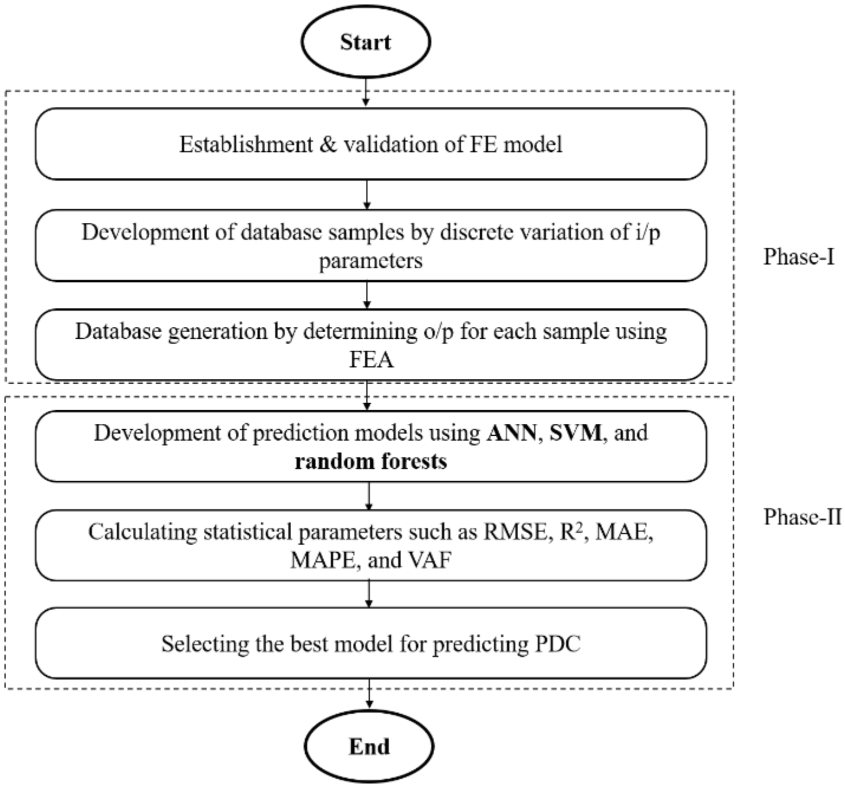

Figure 6.1 Flowchart of the proposed approach for development of AI prediction models

6.3 Case study

In this work, the blast analysis has been performed for underground RC tunnels utilized in Delhi Metro, India. The specifications of RC tunnel along with the typical reinforcement detailing are the same as discussed in the previous chapter.

6.3.1 Development of Finite Element Model

The 3D-FE model utilized for the blast analysis of unshielded and GFRP shielded subsurface RC tunnels in the previous chapter is used here. The details for the same along with the mesh convergence and validation studies can be referred in Section 5.2 of this thesis.

6.3.2 Development of AI prediction models

6.3.2.1 Simulated data for RC tunnels

In order to establish accurate and reliable prediction models, it is important to develop a sufficiently large database which reflects the possible range of variations of the considered parameters. Based on the previous literatures, it is discovered that the parameters such as geometry of tunnel lining [107], material properties of tunnel lining [95], TNT charge [100, 196], and surrounding soil properties [5, 107] dominantly govern the peak displacement values of RC tunnel in case of an internal explosion. Hence, in the present study, the following parameters are considered: concrete characteristic compressive strength, steel yield tensile strength, thickness of RC tunnel, TNT charge, and surrounding soil. Additionally, from the numerical analysis in the previous chapter, it is observed that the application of GFRP as a shielding material over RC tunnel effectively reduces the peak displacement values. Hence, GFRP thickness is also considered a major parameter influencing the output. The complete details of input parameters and their range of variations is shown in Table 6.1. The selected values of parameters for concrete and steel are the values generally utilized for underground RC tunnels. It should be noted that the range of input parameters for RC tunnel, soil, and TNT explosive are selected based on previous studies [5, 88, 95, 102, 105, 107]. Three different GFRP thicknesses which could be effectively utilized for blast resistant design have also been considered. The values of input parameters are varied discretely in each sample. A total number of 192 non- and GFRP strengthened RC tunnel samples are generated (Please see Table 6.2) and the output (peak displacement) for each sample is determined using FE analysis. The database is then used for developing AI models for predicting the peak displacement at the crown of RC tunnel under internal explosion.

Table 6.1 Input parameters and their range

Input parameter	Unit	Symbol	Selected values
GFRP thickness	mm	t	0, 10, 20, 30
Explosive charge	kg	T	10, 50, 100
Characteristic compressive strength of concrete	MPa	f_{ck}	50, 80

Thickness of RC tunnel	mm	t_t	300, 500
Yield tensile strength of steel	MPa	f_y	415, 600
Type of soil	-	-	Saturated, Unsaturated

Table 6.2 Possible dataset combinations for development of AI models

Dataset No.	GFRP thickness	Explosive charge	f_{ck}	Thickness of RC tunnel	f_y	Type of soil
1	0	10	50	300	415	Saturated
2	10	10	50	300	415	Saturated
3	20	10	50	300	415	Saturated
4	30	10	50	300	415	Saturated
..	..	..	..	..	..	..
..	..	..	..	..	..	..
..	..	..	..	..	..	..
189	0	100	80	500	600	Unsaturated
190	10	100	80	500	600	Unsaturated
191	20	100	80	500	600	Unsaturated
192	30	100	80	500	600	Unsaturated

*fck = Concrete characteristic compressive strength,

f_y = yield strength of steel

6.3.2.2 Artificial Intelligence models

In order to develop the AI models for predicting peak displacement at the crown of tunnel, the database is first pre-processed by randomly splitting it into two or three parts. This ensures arbitrary sampling of the dataset. The first part is used as a training dataset for training the prediction models. The remaining parts are used for validation or testing purposes. For the ANN model, the database is split randomly in order to reduce the bias in selection as well as to ensure equal consideration to each variable during training phase. The database is split into three parts:

training, validation, testing. In the present study, 70 % of the total database (~136 samples) is considered as the training dataset, 15 % of the total database (~28 samples) is considered as validating dataset, and the remaining 15 % of the total database (~28 samples) is considered as testing dataset. The ANN model is developed in Matlab version R2015a using a sigmoid function. The sigmoid function is a mathematical function which is monotonous, continuous, and differentiable in nature. It is an activation function which is necessary for training NN's utilizing gradient descent optimization algorithm [197]. Herein, a non-linear optimization Levenberg–Marquardt algorithm is used for training the model [198]. A general ANN model consists of three layers: input layer, hidden layer, and output layer. Each hidden layer has neurons which have different jobs. It is important to select an adequate number of neurons as too large number of neurons may lead to overfitting of the data, while insufficient number of neurons may not consider the relationship between variables adequately [199]. Similarly, an increased number of hidden layers will result in increased computational time and cause underfitting or overfitting of data [119]. In this work, three hidden layers have been selected. In order to select the number of neurons in hidden layer, a trial-and-error analysis is performed in which the number of neurons is varied from 1 to 20. The test R score and MAE score values are selected as the performance measures for this analysis. The results of this analysis are shown in Figure 6.2. On this basis, 5 number of neurons are finalized for the model.

For the SVM model, the radius basis function (RBF) has been used for training the model in RStudio software and the model is developed using linear regression function. The database is divided into two parts: 70 % (136 samples) of the total database are utilized as training database, while the remaining 30 % (56 samples) are utilized as testing database. A total number of 10,000 models are developed using this algorithm for the training dataset. The performance of these models is evaluated by using the testing database. The model which displays best performance in terms of maximum NSE (Nash-Sutcliffe Efficiency) value is selected. In the present study, model_1042 is selected as the best performing model giving NSE values of 0.99 and 0.98 for training and testing database respectively.

The random forests algorithm is utilized for developing a prediction model in RStudio software using linear regression function. A filter in the package "randomForest" is used for performing the regressions. Similar to the SVM model, the total database is divided into two parts (70:30) for training and testing purposes (136 and 56 samples respectively) and a total number of 10,000 models are generated. The performance of these models is evaluated based on NSE (Nash-Sutcliffe Efficiency) value. In the present study, model_286 is selected as the best performing model giving NSE values of 0.98 and 0.98 for training and testing database respectively. In order to finalize the number of trees, a trial-and-error analysis is carried out in which the number of trees is varied from 1 to 20. The R and MAE values obtained for different number of trees are shown in Figure 6.3. Based on the hyperparameter tuning, a total number of 5 decision trees are selected.

There are some significant differences in the working of ANN, SVM, and RF models. ANN has numerous parameters in the form of number of layers, while SVM has two parameters i.e., w, and M, while the depth of forest and number of trees are the two parameters in RF model. In ANN and SVM model, input data is mapped to a higher dimensional space in order to assign a decision boundary. The ANN model has a non-linear decision boundary, while SVM model consists of a linear decision boundary. In RF model, the decision trees are a group of non-linear datasets. The optimization algorithm used in SVM and ANN are minimum sequential algorithm and gradient descent algorithm respectively, while no optimization algorithm is utilized in RF model. However, ANN requires larger number of dataset for achieving a desired precision, while SVM and RF could work with fewer data.

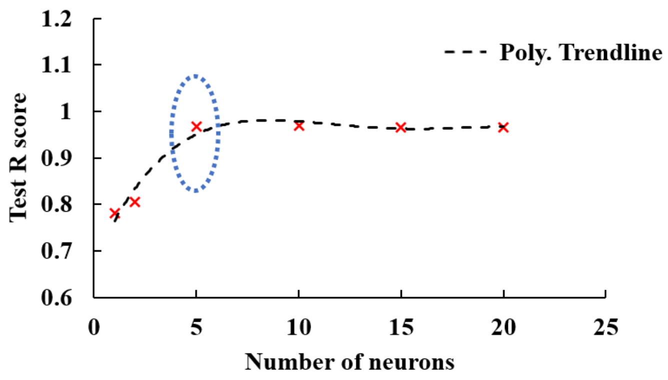

(a)

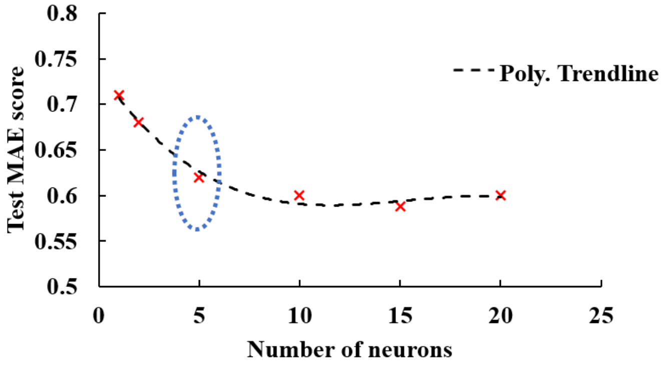

(b)

Figure 6.2 Hyperparameter tuning for ANN (a) Test R score (b) Test MAE score

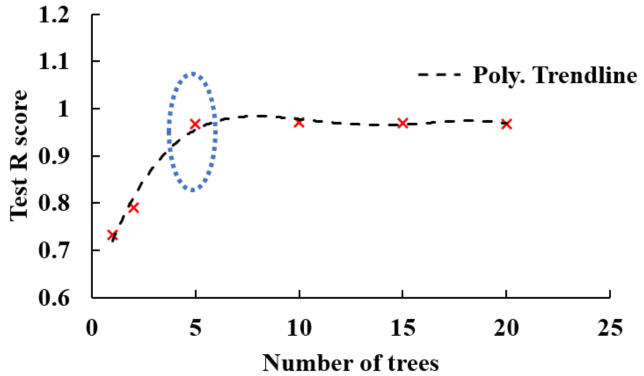

(a)

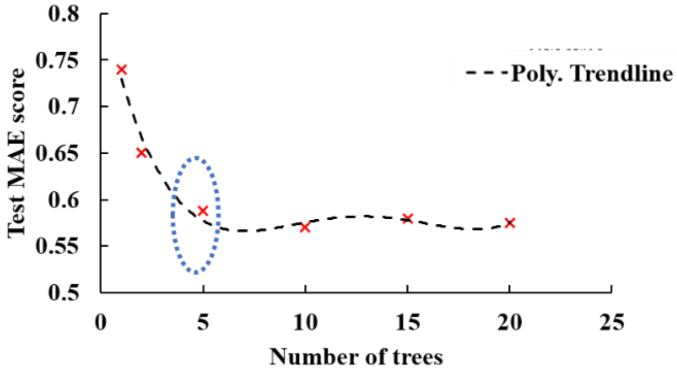

(b)

Figure 6.3 Hyperparameter tuning for RF (a) Test R score (b) Test MAE score

6.4 Results and discussions

The proposed approach discussed in previous sections is applied and a total number of three AI models are developed for predicting the peak displacement of subsurface RC tunnel against internal explosion. In this section, the results of prediction models are discussed and the performance of each model is compared based on several performance metrics.

6.4.1 Artificial Neural Networks

The values of peak tunnel displacement predicted by ANN model are compared with the actual peak displacement values obtained from FE simulations as shown in Figure 6.4(a). The square error for each ANN model prediction is shown in Figure 6.4(b). A maximum square error of 27 is obtained for the ANN model. These figures are divided in three parts: training, validation, and testing. In the training phase, the model is trained to predict the peak displacement values which is then validated and tested using separate databases. The detailed results of training, validation, and testing data for the ANN model are shown in the scatter plots of actual and predicted peak displacement values in Figure 6.5, while the R^2 values for different datasets are shown in Table *6.3*. It can be observed that most of the points are scattered very close to the ideal line. Hence, a good fitness of data for the ANN model is obtained. Also, the R^2 values for testing and validation datasets are lesser compared to that of training dataset, which shows that the overfitting of data has been avoided. Although it is desirable to carry out a detailed k-fold cross-validation along with overfitting calculations, the main aim of this work is to testify the use of different AI models for predicting the response of underground RC tunnels against blast loading similar to the work of Dennis et al. [200] for blast load prediction. Hence, the overfitting analysis has been performed using R^2 values for testing and validation datasets.

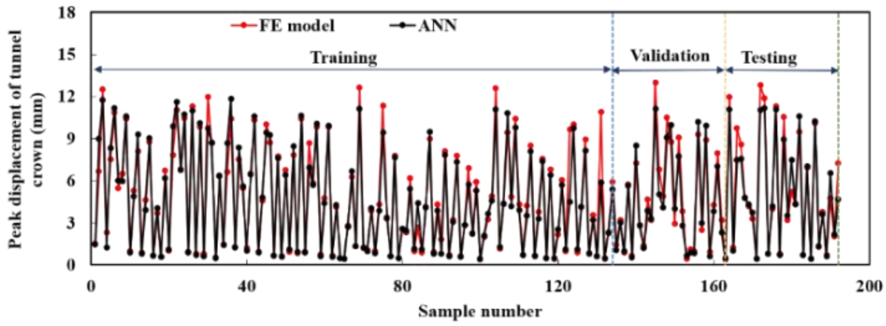

(a)

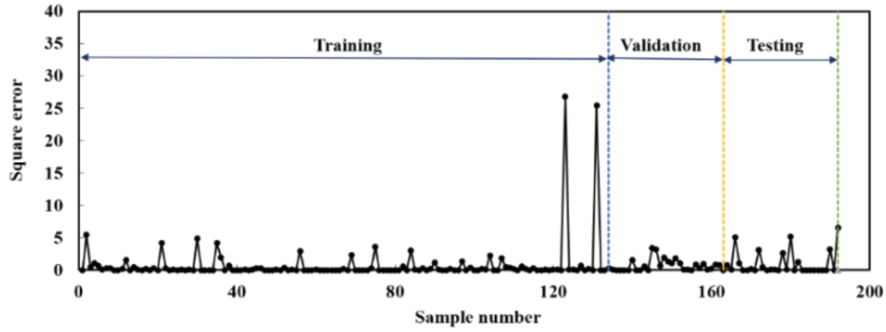

(b)

Figure 6.4 (a) Comparison of peak displacement value obtained by FE model and ANN model (b) square error for ANN model predictions

Table 6.3 R square values for different prediction models

Prediction model	R^2 values			
	Training	Testing	Validation	Average of testing and validation
ANN	0.942	0.939	0.9364	0.9377
SVM	0.9371	0.936	-	0.936
RF	0.955	0.937	-	0.937

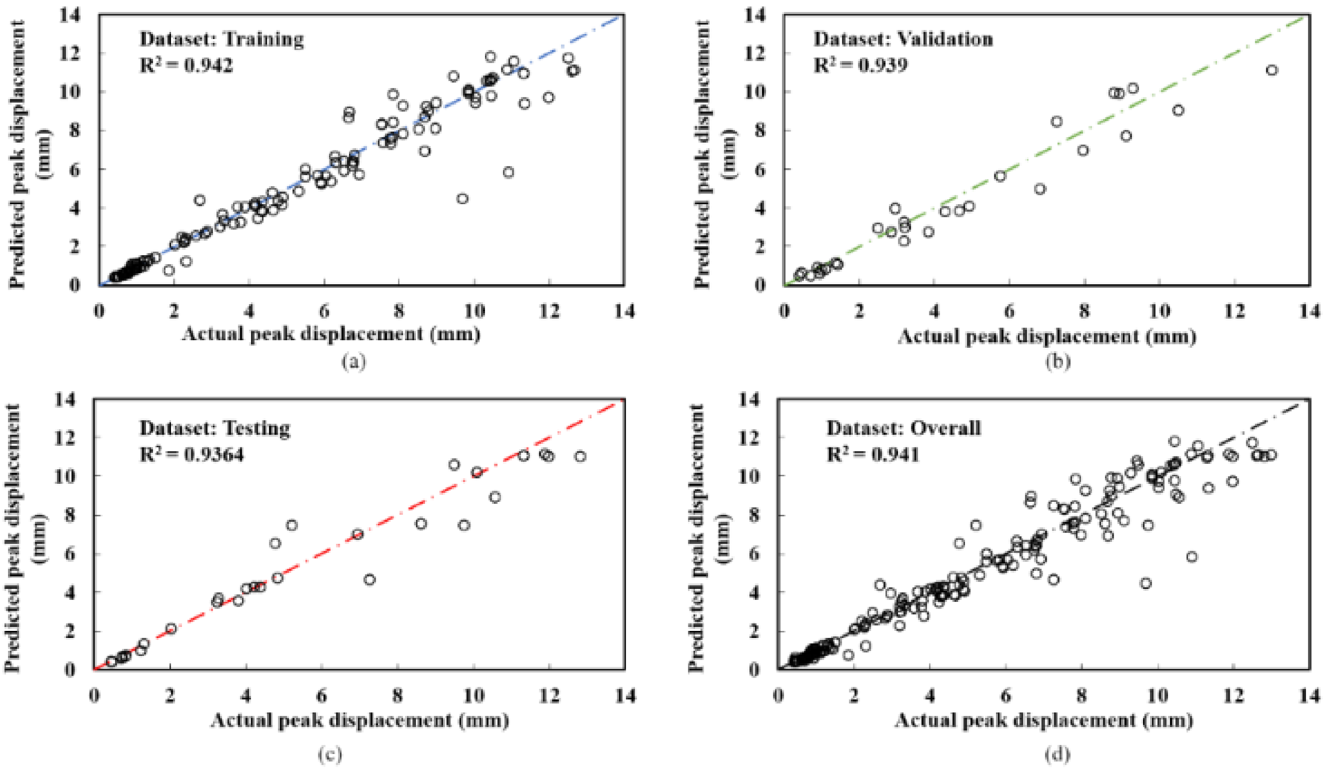

Figure 6.5 Scatter plots for the ANN prediction model for various phases (a) training (b) validation (c) testing (d) complete database

6.4.2 Support Vector Machines

The comparison of SVM model predictions and actual peak displacement values obtained from FE simulations is shown in Figure 6.6(a). The square error for each SVM model prediction is shown in Figure 6.6(b). A maximum square error of 24 is obtained for the SVM model. These figures are divided in two parts: training, and testing. The training dataset is used to train the SVM model for the prediction of peak displacement value. The trained model is then tested utilizing the testing database. The scatter plots of actual and predicted peak displacement values for training, and testing phases for the SVM model are shown in Figure 6.7. It can be observed that most of the points are scattered very close to the ideal line with R^2 values more than 0.936 for all the phases.

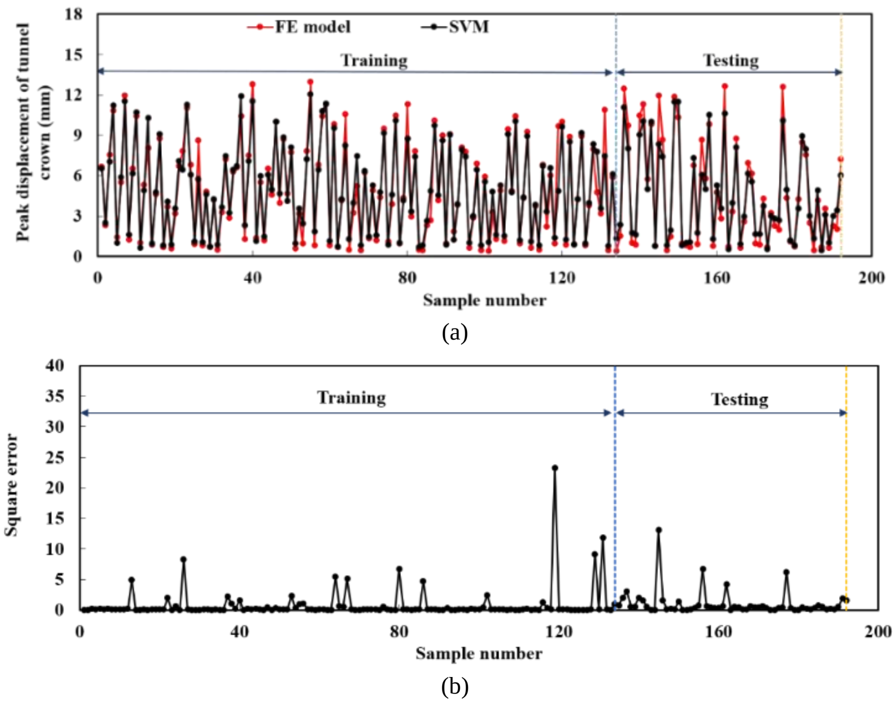

Figure 6.6 (a) Comparison of peak displacement value obtained by FE model and SVM model (b) square error for SVM model predictions

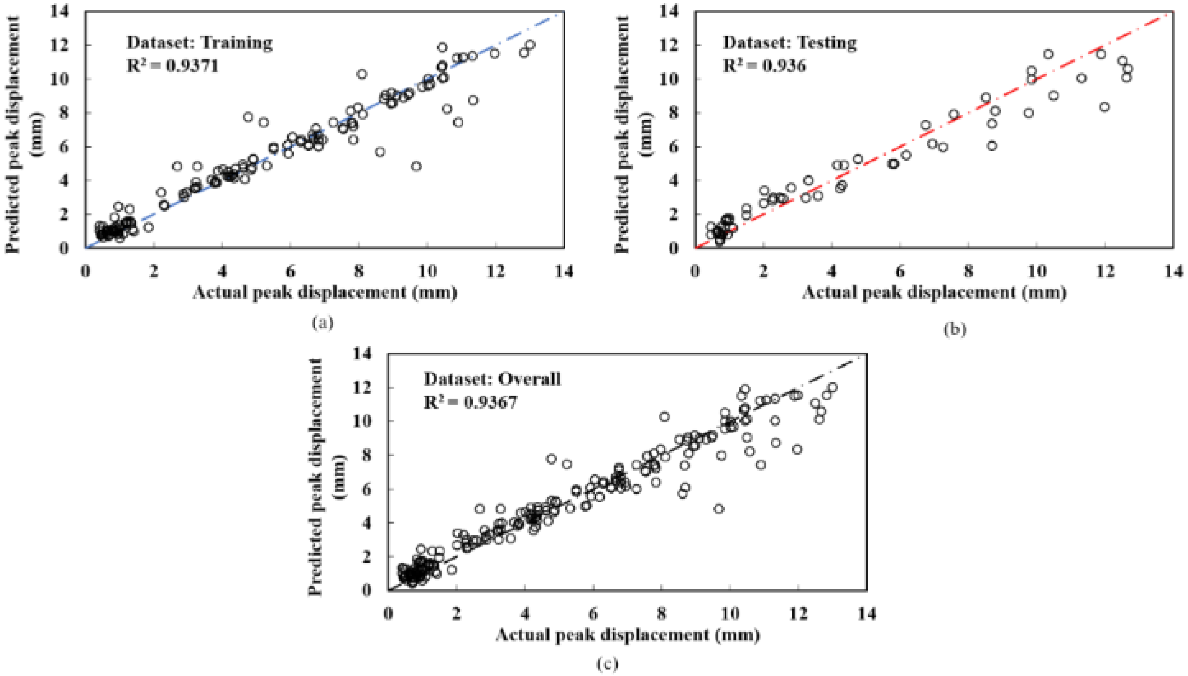

Figure 6.7 Scatter plots for the SVM prediction model for various phases (a) training (b) validation (c) testing (d) complete database

6.4.3 Random Forest

The peak tunnel displacement predictions made by RF model are compared with the actual peak displacement values obtained from FE simulations as shown in Figure 6.8(a). The square error for each prediction is shown in Figure 6.8(b). A maximum square error of 21 is obtained for this model. The scatter plots of different phases for the RF model are displayed in Figure 6.9. It can be observed that a good agreement between the actual and predicted values is obtained. The R^2 values are more than 0.937 for all the phases.

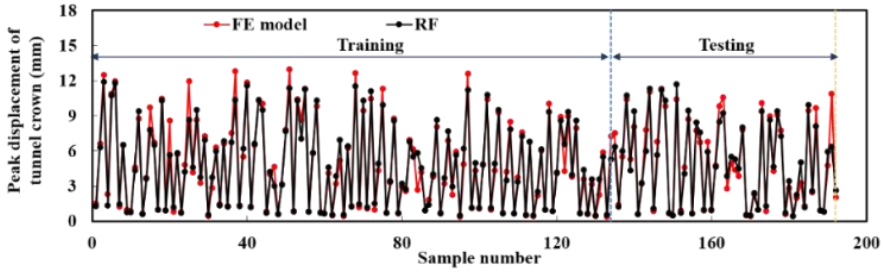

(a)

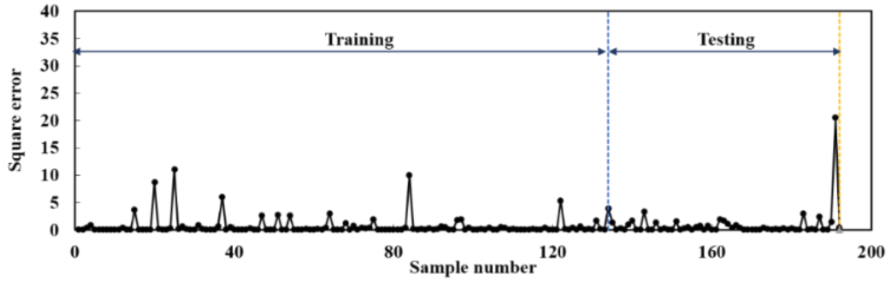

(b)

Figure 6.8 (a) Comparison of peak displacement value obtained by FE model and RF model (b) square error for RF model predictions

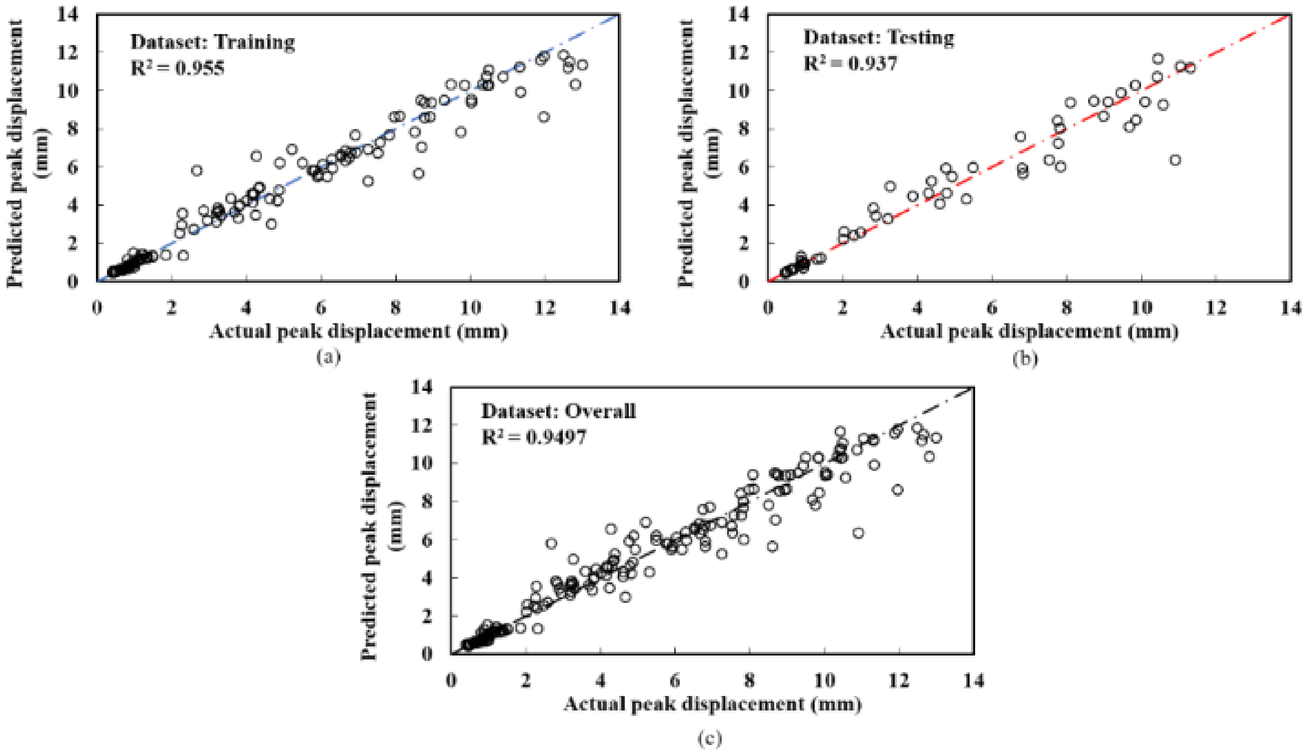

Figure 6.9 Scatter plots for the RF prediction model for various phases (a) training (b) validation (c) testing (d) complete database

6.4.4 Performance of prediction models

The performance of trained AI models is evaluated using the testing databases. The values of performance metrics such as RMSE, R^2, MAE, MAPE, and VAF are determined using Eqs. (2.46) to (2.50). The results are summarized in Table 6.4. It can be observed that the R^2 values range from 0.936 to 0.9368 and the RMSE and MAE values range from 0.925 to 1.041 and 0.588 to 0.775 respectively. The developed models perform well and could be utilized for prediction of peak displacement values of underground RC tunnels subjected to explosive loading conditions. Also, the MAE values suggest that the models are very stable. However, it is notable that the performance of RF for predicting the peak tunnel displacement is superior compared to the other two prediction models. Thus, it can be considered the best model for peak displacement prediction of RC tunnels under blast loading.

Table 6.4 Performance of AI models for predicting the peak tunnel displacement

Prediction model	RMSE	R^2	MAE	MAPE	VAF
ANN	1.023	0.9364	0.63	10.751	93.31
SVM	1.041	0.936	0.775	30.46	93.644
RF	0.925	0.9368	0.588	12.339	93.682

6.5 Summary

In this work, artificial intelligence (AI) models are explored for predicting the peak displacement of underground RC tunnels against internal explosion. The database of 192 points used for development of prediction models is generated using FE simulations in which the values of governing parameters are varied. For the database development, a combination of six governing parameters is considered as the input, which include: concrete characteristic compressive strength, steel yield tensile strength, TNT charge, surrounding soil, thickness of RC tunnel, and GFRP thickness. Among the several governing parameters, the use of GFRP as a protective layer is found to profoundly reduce the damage as well as vibrations of tunnel lining and improve the performance of RC tunnels against internal explosion. Thus, it is concluded that the GFRP layer could be effectively utilized as protective covering over underground RC tunnels in order to improve their safety in case of an internal explosion.

Further, three AI models are explored which include: ANN, SVM, and random forests. The performance of these models is evaluated based on several performance metrics. Results show that the developed prediction models are stable and have high R^2 values and low RMSE and MAE values. Among the three models, RF exhibited the best performance for peak displacement prediction with the performance MAE value of 0.588, R^2 value of 0.9368, and RMSE value of 0.925. The prediction models could be utilized for quick damage assessment as well as blast resistant design of underground RC tunnels. However, the AI models have some limitations, the models are completely data driven processes. Also, the output values may be critically affected by the significance of input data points, and the models do not provide simplified empirical equations for predicting the response of tunnels. In order to carry out any further analysis, models would have to be developed again by the user. Also, the optimal accuracy in prediction may not be obtained due to overfitting assessments. Overall, it is concluded that the AI models could be effectively used for peak displacement prediction of RC tunnel under internal blast loading and prove to be a good competitor to the existing numerical methods.

Chapter-7

Conclusion and scope for future work

7.1 Summary and conclusions

Concrete is one of the most widely used materials in the construction sector. It is used in the construction of protective structures as well as numerous structural elements that might be exposed to extreme loading events during their lifespan. However, due to its low tensile and flexural strength, brittle nature, and heterogeneous structure, concrete exhibits poor performance under such loading conditions. Thus, in the present work, a comprehensive study has been carried out to explore several methodologies in order to improve the response of concrete under extreme loading events. Further, to reduce the dependency of the parametric investigations and analysis proceedings on the experimental and numerical techniques, AI models are developed for predicting the response of concrete structural elements under extreme loading scenarios. Based on the presented work, the following conclusions were made.

A set of CDP parameters were recommended which could be utilized to enhance the response of concrete under low velocity impact. These values were determined as: dilation angle (ψ)= 45°, fracture energy (G_f)= 325 N/m, and Model M3 for uniaxial compressive stress-strain response. Further, the dilation angle (ψ), fracture energy (G_f), and uniaxial compressive stress-strain response inputs in CDP model may be considered as predominant parameters governing the low velocity impact response of concrete, where the tensile mode of failure is expected. Shape parameter (K_c), ratio of biaxial to uniaxial yield strength (σ_{bo}/σ_{co}), and flow potential eccentricity (ε) can be considered insignificant in the 3D nonlinear FE analysis of concrete beams against low velocity impact loading. The efficacy of recommended parameters was verified by performing a 3D-FE analysis which showed an enhancement in the energy absorption capacity by 112%, and reduced damage and cracking of concrete beam.

Later, the effectiveness of utilization of crumb rubber in concrete was investigated. To this end, detailed experimental investigations were conducted to analyse the influence of crumb rubber as partial sand replacement on the low velocity impact response of concrete beams. Various proportions of crumb rubber as partial replacement of sand (0 – 30%) were considered. The use of crumb rubber in concrete was found to enhance the peak impact force, ductility, and energy absorption capacity of concrete beams, which is observed due to higher plastic energy absorption capacity of rubber. This is a desirable trait for concrete safety and protection barriers. At 30% replacement, the peak impact force was increased by approximately 23%, while the peak displacement and energy absorption capacity of concrete was increased by approximately 71%, and 98% respectively. The presence of elastic crumb rubber as well as the gaps/microcracks in rubberized concrete promote toughening mechanism leading to improved impact resistance. Also, the presence of crumb rubber imparts bridging action which eventually arrests the crack development. However, these gaps/microcracks between crumb rubber and cement matrix result in a weak interfacial zone, which is mainly responsible for the reduction in the quasi-static mechanical properties of concrete. The 3D-FE model as well as the proposed analytical method reproduce the peak displacement values with a maximum deviation of 11.3% and 11.5%, respectively. While, the energy absorption capacity of concrete beams is predicted with a maximum deviation of 25% and 13%, respectively. Also, the 3D-FE model predicted the peak impact force values with a maximum deviation of 4.6%. Finally, this study proposed simple design guidelines for M50 grade concrete which could be utilized for selecting optimum rubber content such that the desired minimum compressive strength is achieved with improved impact resistance properties.

In the past few decades, significant attention has been given towards issues related to dynamic loading. The impact and earthquake loading related issues are relatively old. However, due to the recent accidental and intentional episodes across the globe, the dilemmas related to blast loading are relatively new for the structural engineers and researchers. Among the different types of structures, the subsurface RC tunnels have become the easiest and most preferred targets for terrorist attacks. Thus, in the present work, a novel concept involving the use of GFRP layer as a protective shield for strengthening the RC tunnel lining against the impact of internal blast explosion has been introduced. The use GFRP layer as protective shield reduced the peak displacement, and stress values in RC tunnel by approximately 14% and 25% for 100 kg explosive, 35% and 25% for 50 kg explosive, and 40% and 35 %, respectively for 10 kg explosive. Also, the use of GFRP layer curbed the damage and plastic strains induced in tunnel as well as the stresses and displacements at the top surface of soil. Consequently, it reduced the risk of long-term geotechnical effects such as liquefaction, and reduced soil shear strength. Thus, it may be concluded that the provision of GFRP layer enhanced the blast resistance of RC tunnel lining. The shielding effect of GFRP layer was found to be more significant for lower explosive charges. Since, the metro underground tunnels are more likely to be subjected to internal explosion of low explosive charges such as 10 kg, which may be easily carried by terrorists inside the subway system. Thus, the present methodology can be easily utilized in metro underground tunnels for substantially improving the safety in case of an internal explosion.

Further, in order to reduce the dependency of researchers for performing the blast analysis of subsurface RC tunnels on the sophisticated numerical techniques, AI models were explored. The database of 192 points used for development of prediction models was generated using FE simulations. A total of three AI models were developed which include: ANN, SVM, and RF. The performance of these models was evaluated based on several performance metrics. Results showed that the prediction models were stable and had high R^2 values and low RMSE and MAE values. Among the three models, RF exhibited the best performance for peak displacement prediction with the performance MAE value of 0.588, R^2 value of 0.9368, and RMSE value of 0.925. Thus, it was concluded that the prediction models could be utilized for quick damage assessment as well as blast resistant design of subsurface RC tunnels.

7.2 Future scope of work

As discussed previously, the present research is dedicated to identify and check potential methods which could be utilized for enhancing the response of concrete under extreme loading conditions. However, there are still many challenges that exist in this field. Hence, the following would be future research work.

- The desired material configuration with recommended CDP parameters (ψ= 45º, Gf= 325 N/m, and uniaxial compressive stress-strain Model M3) obtained from the parametric studies can be achieved by modifying the mix design. In order to achieve the complete material configuration, the utilization of rubber fibers, silica fume, and superplasticizers may be incorporated. However, further experimental trials are needed for achieving the desired objectives.

- Although, rubberized concrete displayed better performance as compared to plain concrete in case of impact loading. The weak bond between crumb rubber and cement matrix was found to be responsible for the reduction in the quasi-static properties of concrete, thus restricting the use of crumb rubber at locations where high compressive strength is a necessity. The surface treatment of crumb rubber using chemical or thermal treatment methods could be utilized. This can be helpful in improving the bond between cement matrix and rubber, such that crumb rubber could be effectively utilized in concrete without compromising the compressive strength.

- Optimization of GFRP thickness could be carried out in order to maximize the performance of RC tunnel in case of internal explosion.
- Advanced AI and hybrid models could also be useful for predicting the damage of subsurface RC tunnels against internal explosion.

REFERENCES

1. Session, C. euro-international du beton. P. (1988). *Concrete structures under impact and impulsive loading: Synthesis report*. Comite euro-international du beton.

2. Othman, H., & Marzouk, H. (2017). Finite-element analysis of reinforced concrete plates subjected to repeated impact loads. *Journal of Structural Engineering*, *143*(9), 04017120.

3. Rajput, A., & Iqbal, M. A. (2017). Ballistic performance of plain, reinforced and pre-stressed concrete slabs under normal impact by an ogival-nosed projectile. *International journal of impact engineering*, *110*, 57–71.

4. Tiwari, R., Chakraborty, T., & Matsagar, V. (2017). Dynamic analysis of tunnel in soil subjected to internal blast loading. *Geotechnical and Geological Engineering*, *35*, 1491–1512.

5. Goel, M. D., Verma, S., & Panchal, S. (2021). Effect of internal blast on tunnel lining and surrounding soil. *Indian Geotechnical Journal*, *51*, 359–368.

6. Baera, C., Szilagyi, H., Mircea, C., Criel, P., & De Belie, N. (2016). CONCRETE STRUCTURES UNDER IMPACT LOADING: GENERAL ASPECTS. *Urbanism. Architecture. Constructions/Urbanism. Arhitectura. Constructii*, *7*(3).

7. Buth, C. E., Brackin, M. S., Williams, W. F., & Fry, G. T. (2011). *Collision loads on bridge piers: phase 2, report of guidelines for designing bridge piers and abutments for vehicle collisions*. Texas Transportation Institute.

8. Gallegos, D., & McPhee, M. (2007). Two truckers die in fiery I-70 crash. The Denver Post.

9. Yao, H.-Y., Kong, X.-J., Shi, Y.-J., Xiao, X.-B., & Le, N.-N. (2018). Aircraft test of engineered material arresting system. *Aircraft Engineering and Aerospace Technology*.

10. Kondrasuk, J. N. (2004). The effects of 9/11 and terrorism on human resource management: Recovery, reconsideration, and renewal. *Employee Responsibilities and Rights Journal*, *16*, 25–35.

11. Kurihashi, Y., & Masuya, H. (2020). Simplified Estimation Method for Maximum Deflection in Bending-Failure-Type Reinforced Concrete Beams Subjected to Collision Action and Its Application Range. *Applied Sciences*, *10*(19), 6941.

12. Aliabdo, A. A., Abd_Elmoaty, A. M., & Hamdy, M. (2013). Effect of internal short fibers, steel reinforcement, and surface layer on impact and penetration resistance of concrete. *Alexandria Engineering Journal*, *52*(3), 407–417.

13. Ulzurrun, G. S. D., & Zanuy, C. (2017). Enhancement of impact performance of reinforced concrete beams without stirrups by adding steel fibers. *Construction and building materials*, *145*, 166–182.

14. Mohammadhosseini, H., Awal, A. S. M. A., & Yatim, J. B. M. (2017). The impact resistance and mechanical properties of concrete reinforced with waste polypropylene carpet fibres. *Construction and Building Materials*, *100*(143), 147–157.

15. Naraganti, S. R., Pannem, R. M. R., & Putta, J. (2019). Impact resistance of hybrid fibre reinforced concrete containing sisal fibres. *Ain Shams Engineering Journal*, *10*(2), 297–305.

16. Mastali, M., Dalvand, A., & Sattarifard, A. (2017). The impact resistance and mechanical properties of the reinforced self-compacting concrete incorporating recycled CFRP fiber with different lengths and dosages. *Composites Part B: Engineering*, *112*, 74–92.

17. Al-Tayeb, M. M., Abu Bakar, B. H., Ismail, H., & Md Akil, H. (2013). Effect of partial replacement of sand by fine crumb rubber on impact load behavior of concrete beam: experiment and nonlinear dynamic analysis. *Materials and structures*, *46*, 1299–1307.

18. Gupta, T., Sharma, R. K., & Chaudhary, S. (2015). Impact resistance of concrete containing waste rubber fiber and silica fume. *International Journal of Impact Engineering*, *83*, 76–87.

19. Ghani Razaqpur, A., Tolba, A., & Contestabile, E. (2007). Blast loading response of reinforced concrete panels reinforced with externally bonded GFRP laminates. *Composites Part B: Engineering*, *38*(5), 535–546. https://doi.org/https://doi.org/10.1016/j.compositesb.2006.06.016

20. Lu, J., Wang, Y., & Zhai, X. (2021). Response of flat steel-concrete-corrugated steel sandwich panel under drop-weight impact load by a hemi-spherical head. *Journal of Building Engineering*, *44*, 102890. https://doi.org/https://doi.org/10.1016/j.jobe.2021.102890

21. Wu, M., Zhang, C., & Chen, Z. (2016). Drop-weight tests of concrete beams prestressed with unbonded tendons and meso-

scale simulation. *International Journal of Impact Engineering*, *93*, 166–183.

22. Iqbal, M. A., Kumar, V., & Mittal, A. K. (2019). Experimental and numerical studies on the drop impact resistance of prestressed concrete plates. *International Journal of Impact Engineering*, *123*, 98–117.

23. Rajput, A., & Iqbal, M. A. (2017). Impact behavior of plain, reinforced and prestressed concrete targets. *Materials & Design*, *114*, 459–474.

24. Khaloo, A. R., Dehestani, M., & Rahmatabadi, P. (2008). Mechanical properties of concrete containing a high volume of tire–rubber particles. *Waste management*, *28*(12), 2472–2482.

25. Guruprasad, S., & Mukherjee, A. (2000). Layered sacrificial claddings under blast loading Part I — analytical studies. *International Journal of Impact Engineering*, *24*(9), 957–973. https://doi.org/https://doi.org/10.1016/S0734-743X(00)00004-X

26. Hanssen, A. G., Enstock, L., & Langseth, M. (2002). Close-range blast loading of aluminium foam panels. *International Journal of Impact Engineering*, *27*(6), 593–618. https://doi.org/https://doi.org/10.1016/S0734-743X(01)00155-5

27. Mandal, J., Goel, M. D., & Agarwal, A. K. (2022). Study of Different Materials to Mitigate Blast Energy for the Tunnel Subjected to Buried Explosion. In S. Krishnapillai, V. R., & S. K. Ha (Eds.), *Composite Materials for Extreme Loading* (pp. 505–518). Singapore: Springer Singapore.

28. Pham, T. M., & Hao, H. (2016). Behavior of fiber-reinforced polymer-strengthened reinforced concrete beams under static and impact loads. *International Journal of Protective Structures*, *8*(1), 3–24. https://doi.org/10.1177/2041419616658730

29. Phulari, V. S., & Goel, M. D. (2021). Dynamic Response of Tunnel Under Blast Loading and Its Blast Mitigation Using CFRP as Protective Barrier. In S. K. Saha & M. Mukherjee (Eds.), *Recent Advances in Computational Mechanics and Simulations* (pp. 555–562). Singapore: Springer Singapore.

30. Caliskan, U., Ekici, R., Yildiz, E., & Apalak, M. K. (2020). A study on low-velocity impact performance of notched GFRP composites repaired by different composite patches: Experiment and modeling. *Polymer Composites*, *41*(4), 1323–1340. https://doi.org/https://doi.org/10.1002/pc.25457

31. Armaghani, D. J., Hatzigeorgiou, G. D., Karamani, C., Skentou, A., Zoumpoulaki, I., & Asteris, P. G. (2019). Soft computing-based techniques for concrete beams shear strength. *Procedia Structural Integrity*, *17*, 924–933. https://doi.org/https://doi.org/10.1016/j.prostr.2019.08.123

32. Patnaik, G., Kaushik, A., Singh, M. J., Rajput, A., Prakash, G., & Borana, L. (2022). Damage Prediction of Underground Pipelines Subjected to Blast Loading. *Arabian Journal for Science and Engineering*, *47*(10), 13559–13578. https://doi.org/10.1007/s13369-022-06920-4

33. Zhang, X., Nguyen, H., Bui, X.-N., Anh Le, H., Nguyen-Thoi, T., Moayedi, H., & Mahesh, V. (2020). Evaluating and Predicting the Stability of Roadways in Tunnelling and Underground Space Using Artificial Neural Network-Based Particle Swarm Optimization. *Tunnelling and Underground Space Technology*, *103*, 103517. https://doi.org/https://doi.org/10.1016/j.tust.2020.103517

34. Micallef, K., Sagaseta, J., Fernández Ruiz, M., & Muttoni, A. (2014). Assessing punching shear failure in reinforced concrete flat slabs subjected to localised impact loading. *International Journal of Impact Engineering*, *71*, 17–33. https://doi.org/https://doi.org/10.1016/j.ijimpeng.2014.04.003

35. Manual, A. U. (2020). Abaqus user manual. *Abacus*.

36. Siddique, S., Shrivastava, S., & Chaudhary, S. (2018). Durability properties of bone china ceramic fine aggregate concrete. *Construction and Building Materials*, *173*, 323–331.

37. Al-Tayeb, M. M., Bakar, B. H. A., Ismail, H., & Akil, H. M. (2012). Impact resistance of concrete with partial replacements of sand and cement by waste rubber. *Polymer-Plastics Technology and Engineering*, *51*(12), 1230–1236.

38. Al-Tayeb, M. M., Abu Bakar, B. H., Ismail, H., & Md Akil, H. (2013). Effect of partial replacement of sand by fine crumb rubber on impact load behavior of concrete beam: experiment and nonlinear dynamic analysis. *Materials and Structures*, *46*(8), 1299–1307. https://doi.org/10.1617/s11527-012-9974-3

39. Pham, T. M., Chen, W., Khan, A. M., Hao, H., Elchalakani, M., & Tran, T. M. (2020). Dynamic compressive properties of lightweight rubberized concrete. *Construction and Building Materials*, *238*, 117705.

40. Saxena, R., Siddique, S., Gupta, T., Sharma, R. K., & Chaudhary, S. (2018). Impact resistance and energy absorption capacity of

concrete containing plastic waste. *Construction and Building Materials*, *176*, 415–421. https://doi.org/10.1016/j.conbuildmat.2018.05.019

41. Foti, D., & Paparella, F. (2014). Impact behavior of structural elements in concrete reinforced with PET grids. *Mechanics Research Communications*, *57*, 57–66. https://doi.org/10.1016/j.mechrescom.2014.02.007

42. Mustafa, M. A., Hana, I., Mahmoud, R., & Tayeh, B. A. (2019). E ff ect of partial replacement of sand by plastic waste on impact resistance of concrete : experiment and simulation, *20*(April), 519–526. https://doi.org/10.1016/j.istruc.2019.06.008

43. Mohammadhosseini, H., Awal, A. S. M. A., & Mohd, J. B. (2017). The impact resistance and mechanical properties of concrete reinforced with waste polypropylene carpet fibres. *Construction and Building Materials*, *143*, 147–157. https://doi.org/10.1016/j.conbuildmat.2017.03.109

44. Mohammadhosseini, H., Tahir, M., Rahman, A., & Sam, M. (2018). The feasibility of improving impact resistance and strength properties of sustainable concrete composites by adding waste metalized plastic fibres. *Construction and Building Materials*, *169*, 223–236. https://doi.org/10.1016/j.conbuildmat.2018.02.210

45. Lee, J., Yuan, T., Shin, H., & Yoon, Y. (2020). Strategic use of steel fibers and stirrups on enhancing impact resistance of ultra-high-performance fiber-reinforced concrete beams. *Cement and Concrete Composites*, *107*(December 2019), 103499. https://doi.org/10.1016/j.cemconcomp.2019.103499

46. Nili, M., & Afroughsabet, V. (2010). International Journal of Impact Engineering Combined effect of silica fume and steel fi bers on the impact resistance and mechanical properties of concrete. *International Journal of Impact Engineering*, *37*(8), 879–886. https://doi.org/10.1016/j.ijimpeng.2010.03.004

47. Othman, H., & Marzouk, H. (2018). Applicability of damage plasticity constitutive model for ultra-high performance fibre-reinforced concrete under impact loads. *International Journal of Impact Engineering*, *114*, 20–31. https://doi.org/https://doi.org/10.1016/j.ijimpeng.2017.12.013

48. Ulzurrun, G. S. D., & Zanuy, C. (2017). Enhancement of impact performance of reinforced concrete beams without stirrups by adding steel fibers. *Construction and Building Materials*, *145*, 166–182. https://doi.org/10.1016/j.conbuildmat.2017.04.005

49. Mo, K. H., Yap, S. P., Alengaram, U. J., Jumaat, M. Z., & Bu, C. H. (2014). Impact resistance of hybrid fibre-reinforced oil palm shell concrete. *Construction and Building Materials*, *50*, 499–507. https://doi.org/10.1016/j.conbuildmat.2013.10.016

50. Yoo, D., Gohil, U., Gries, T., & Yoon, Y. (2015). Comparative low-velocity impact response of textile-reinforced concrete and steel-fiber-reinforced concrete beams. https://doi.org/10.1177/0021998315604039

51. Lee, D., & Shin, A. H.-C. (2016). Finite element study on the impact responses of concrete masonry unit walls strengthened with fiber-reinforced polymer composite materials. *Composite Structures*, *154*, 256–268. https://doi.org/https://doi.org/10.1016/j.compstruct.2016.07.063

52. Anas, S. M., Alam, M., & Tahzeeb, R. (2022). Impact response prediction of square RC slab of normal strength concrete strengthened with (1) laminates of (i) mild-steel and (ii) C-FRP, and (2) strips of C-FRP under falling-weight load. *Materials Today: Proceedings*. https://doi.org/https://doi.org/10.1016/j.matpr.2022.07.324

53. Wang, B., Zhu, H., Wu, X., Zhang, N., & Yan, B. (2020). Numerical investigation on low-velocity impact response of CFRP wraps in presence of concrete substrate. *Composite Structures*, *231*, 111541. https://doi.org/https://doi.org/10.1016/j.compstruct.2019.111541

54. Dey, V., Zani, G., Colombo, M., Di Prisco, M., & Mobasher, B. (2015). Flexural impact response of textile-reinforced aerated concrete sandwich panels. *Materials & Design*, *86*, 187–197. https://doi.org/https://doi.org/10.1016/j.matdes.2015.07.004

55. Kaushik, A., Prakash, G., & Rajput, A. (2022). Influence of crumb rubber on the response of concrete beams against low velocity impact. *Construction and Building Materials*, *347*, 128614. https://doi.org/https://doi.org/10.1016/j.conbuildmat.2022.128614

56. Sukontasukkul, P., & Chaikaew, C. (2006). Properties of concrete pedestrian block mixed with crumb rubber. *Construction and Building Materials*, *20*(7), 450–457. https://doi.org/https://doi.org/10.1016/j.conbuildmat.2005.01.040

57. M, R. T. M., El-Dieb, A. S., A, A. E.-W. M., & Abdel-Hameed, M. E. (2008). Mechanical, Fracture, and Microstructural

Investigations of Rubber Concrete. *Journal of Materials in Civil Engineering*, *20*(10), 640–649. https://doi.org/10.1061/(ASCE)0899-1561(2008)20:10(640)

58. Najim, K. B., & Hall, M. R. (2010). A review of the fresh/hardened properties and applications for plain- (PRC) and self-compacting rubberised concrete (SCRC). *Construction and Building Materials*, *24*(11), 2043–2051. https://doi.org/https://doi.org/10.1016/j.conbuildmat.2010.04.056

59. Mohammed, B. S., Anwar Hossain, K. M., Eng Swee, J. T., Wong, G., & Abdullahi, M. (2012). Properties of crumb rubber hollow concrete block. *Journal of Cleaner Production*, *23*(1), 57–67. https://doi.org/https://doi.org/10.1016/j.jclepro.2011.10.035

60. Atahan, A. O., & Yücel, A. Ö. (2012). Crumb rubber in concrete: Static and dynamic evaluation. *Construction and Building Materials*, *36*, 617–622. https://doi.org/https://doi.org/10.1016/j.conbuildmat.2012.04.068

61. Xue, J., & Shinozuka, M. (2013). Rubberized concrete: A green structural material with enhanced energy-dissipation capability. *Construction and Building Materials*, *42*, 196–204. https://doi.org/https://doi.org/10.1016/j.conbuildmat.2013.01.005

62. Li, D., Zhuge, Y., Gravina, R., & Mills, J. E. (2018). Compressive stress strain behavior of crumb rubber concrete (CRC) and application in reinforced CRC slab. *Construction and Building Materials*, *166*, 745–759. https://doi.org/https://doi.org/10.1016/j.conbuildmat.2018.01.142

63. Li, D., Xiao, J., Zhuge, Y., Mills, J. E., Senko, H., & Ma, X. (2020). Experimental study on crumb rubberised concrete (CRC) and reinforced CRC slabs under static and impact loads. *Australian Journal of Structural Engineering*, *21*(4), 294–306. https://doi.org/10.1080/13287982.2020.1809811

64. Eisa, A. S., Elshazli, M. T., & Nawar, M. T. (2020). Experimental investigation on the effect of using crumb rubber and steel fibers on the structural behavior of reinforced concrete beams. *Construction and Building Materials*, *252*, 119078. https://doi.org/https://doi.org/10.1016/j.conbuildmat.2020.119078

65. Anand, R., Praveen, N., & Shashikala, A. P. (2020). Application of Fiber-Reinforced Rubcrete for Crash Barriers. *Journal of Materials in Civil Engineering*, *32*(12), 04020358. https://doi.org/10.1061/(ASCE)MT.1943-5533.0003454

66. Hameed, A. S., & Shashikala, A. P. (2016). Suitability of rubber concrete for railway sleepers. *Perspectives in Science*, *8*, 32–35. https://doi.org/https://doi.org/10.1016/j.pisc.2016.01.011

67. Abdelmonem, A., El-Feky, M. S., Nasr, E.-S. A. R., & Kohail, M. (2019). Performance of high strength concrete containing recycled rubber. *Construction and Building Materials*, *227*, 116660. https://doi.org/https://doi.org/10.1016/j.conbuildmat.2019.08.041

68. Chan, Y.-W., & Chu, S.-H. (2004). Effect of silica fume on steel fiber bond characteristics in reactive powder concrete. *Cement and Concrete Research*, *34*(7), 1167–1172. https://doi.org/https://doi.org/10.1016/j.cemconres.2003.12.023

69. Uygunoğlu, T. (2008). Investigation of microstructure and flexural behavior of steel-fiber reinforced concrete. *Materials and Structures*, *41*(8), 1441–1449. https://doi.org/10.1617/s11527-007-9341-y

70. Jiang, C., Fan, K., Wu, F., & Chen, D. (2014). Experimental study on the mechanical properties and microstructure of chopped basalt fibre reinforced concrete. *Materials & Design*, *58*, 187–193. https://doi.org/https://doi.org/10.1016/j.matdes.2014.01.056

71. Mastali, M., Dalvand, A., & Sattarifard, A. R. (2016). The impact resistance and mechanical properties of reinforced self-compacting concrete with recycled glass fibre reinforced polymers. *Journal of Cleaner Production*, *124*, 312–324. https://doi.org/https://doi.org/10.1016/j.jclepro.2016.02.148

72. Hannawi, K., Bian, H., Prince-Agbodjan, W., & Raghavan, B. (2016). Effect of different types of fibers on the microstructure and the mechanical behavior of Ultra-High Performance Fiber-Reinforced Concretes. *Composites Part B: Engineering*, *86*, 214–220. https://doi.org/https://doi.org/10.1016/j.compositesb.2015.09.059

73. Gupta, T., Chaudhary, S., & Sharma, R. K. (2014). Assessment of mechanical and durability properties of concrete containing waste rubber tire as fine aggregate. *Construction and Building Materials*, *73*, 562–574.

https://doi.org/https://doi.org/10.1016/j.conbuildmat.2014.09.102

74. Trilok, G., Anshuman, T., Salman, S., K, S. R., & Sandeep, C. (2017). Response Assessment under Dynamic Loading and Microstructural Investigations of Rubberized Concrete. *Journal of Materials in Civil Engineering*, *29*(8), 04017062. https://doi.org/10.1061/(ASCE)MT.1943-5533.0001905

75. Akinyele, J. O., Salim, R. W., & Kupolati, W. K. (2016). Effect of rubber crumb on the microstructural properties of concrete. *African Journal of Science, Technology, Innovation and Development*, *8*(5–6), 467–474.

76. Guo, J., Huang, M., Huang, S., & Wang, S. (2019). An experimental study on mechanical and thermal insulation properties of rubberized concrete including its microstructure. *Applied Sciences*, *9*(14), 2943.

77. Guner, S., & Vecchio, F. (2012). Simplified Method for Nonlinear Dynamic Analysis of Shear-Critical Frames. *Aci Structural Journal*, *109*, 727–737.

78. Timsah, Y., Jahami, A., Khatib, J., & Sonebi, M. (2018). Numerical analysis of a reinforced concrete beam under blast loading. *MATEC Web of Conferences*, *149*, 02063. https://doi.org/10.1051/matecconf/201814902063

79. Ožbolt, J., Bošnjak, J., & Sola, E. (2013). Dynamic fracture of concrete compact tension specimen: Experimental and numerical study. *International Journal of Solids and Structures*, *50*(25), 4270–4278. https://doi.org/https://doi.org/10.1016/j.ijsolstr.2013.08.030

80. Dan, P., & J, V. F. (2007). Simulation of Cyclically Loaded Concrete Structures Based on the Finite-Element Method. *Journal of Structural Engineering*, *133*(5), 728–738. https://doi.org/10.1061/(ASCE)0733-9445(2007)133:5(728)

81. Centre, J. R., Transport, I. for E. and, & Martin, O. (2012). *Comparison of different constitutive models for concrete in ABAQUS/explicit for missile impact analyses*. Publications Office. https://doi.org/doi/10.2790/19763

82. Iqbal, M. A., Rajput, A., & Gupta, N. K. (2017). Performance of prestressed concrete targets against projectile impact. *International Journal of Impact Engineering*, *110*, 15–25. https://doi.org/https://doi.org/10.1016/j.ijimpeng.2016.11.015

83. Oucif, C., Kalyana Rama, J. S., Shankar Ram, K., & Abed, F. (2021). Damage modeling of ballistic penetration and impact behavior of concrete panel under low and high velocities. *Defence Technology, 17*(1), 202–211. https://doi.org/https://doi.org/10.1016/j.dt.2020.03.013

84. Wriggers, P., & Laursen, T. A. (2006). *Computational contact mechanics* (Vol. 2). Springer.

85. Hafezolghorani Esfahani, M., Hejazi, F., Vaghei, R., Jaafar, M., & Karimzadeh, K. (2017). Simplified Damage Plasticity Model for Concrete. *Structural Engineering International*, *27*, 68–78. https://doi.org/10.2749/101686616X1081

86. Michał, S., & Andrzej, W. (2015). Calibration of the CDP model parameters in Abaqus. *World Congr Adv Struct Eng Mech (ASEM 15), Incheon Korea*.

87. Demir, A., Ozturk, H., Edip, K., Stojmanovska, M., Bogdanovic, A., & Seismology, E. (2018). Effect of viscosity parameter on the numerical simulation of reinforced concrete deep beam behavior. *The Online Journal of Science and Technology*, *8*(3), 50–56.

88. Chakraborty, T., Larcher, M., & Gebbeken, N. (2014). Performance of tunnel lining materials under internal blast loading. *International Journal of Protective Structures, 5*(1), 83–96.

89. Khan, S., Chakraborty, T., & Matsagar, V. (2016). Parametric sensitivity analysis and uncertainty quantification for cast iron–lined tunnels embedded in soil and rock under internal blast loading. *Journal of Performance of Constructed Facilities, 30*(6), 04016062.

90. Wang, W., Zhang, D., Lu, F., Wang, S.-C., & Tang, F. (2012). Experimental study on scaling the explosion resistance of a one-way square reinforced concrete slab under a close-in blast loading. *International Journal of Impact Engineering*, *49*, 158–164.

91. Park, J. Y., Kim, M. S., & Lee, Y. H. (2017). Dynamic behavior of reinforced concrete panels subjected to blast loading. *Journal of Vibroengineering, 19*(7), 5261–5267.

92. Del Linz, P., Fung, T. C., Lee, C. K., & Riedel, W. (2021). Response mechanisms of reinforced concrete panels to the combined effect of close-in blast and fragments: An integrated experimental and numerical analysis. *International Journal of Protective Structures*, *12*(1), 49–72.

93. Zhao, Y., Chu, C., & Yi, Y. (2016). Study on an engineering measure to improve internal explosion resistance capacity of segmental tunnel lining structures. *Journal of Vibroengineering*, *18*(5), 2997–3009.

94. Rigas, F., & Sklavounos, S. (2005). Experimentally validated 3-D simulation of shock waves generated by dense explosives in confined complex geometries. *Journal of Hazardous Materials*, *121*(1), 23–30. https://doi.org/https://doi.org/10.1016/j.jhazmat.2005.01.031

95. Chaudhary, R. K., Mishra, S., Chakraborty, T., & Matsagar, V. (2018). Vulnerability analysis of tunnel linings under blast loading. *International Journal of Protective Structures*, *10*(1), 73–94. https://doi.org/10.1177/2041419618789438

96. Gui, M. W., & Chien, M. C. (2006). Blast-resistant Analysis for a Tunnel Passing Beneath Taipei Shongsan Airport–a Parametric Study. *Geotechnical & Geological Engineering*, *24*(2), 227–248. https://doi.org/10.1007/s10706-004-5723-x

97. Choi, S., Wang, J., Munfakh, G., & Dwyre, E. (2006). 3D nonlinear blast model analysis for underground structures. In *GeoCongress 2006: Geotechnical Engineering in the Information Technology Age* (pp. 1–6).

98. Feldgun, V. R., Kochetkov, A. V, Karinski, Y. S., & Yankelevsky, D. Z. (2008). Internal blast loading in a buried lined tunnel. *International Journal of Impact Engineering*, *35*(3), 172–183.

99. Yu, H., Wang, Z., Yuan, Y., & Li, W. (2016). Numerical analysis of internal blast effects on underground tunnel in soils. *Structure and Infrastructure Engineering*, *12*(9), 1090–1105.

100. Tiwari, R., Chakraborty, T., & Matsagar, V. (2017). Dynamic analysis of tunnel in soil subjected to internal blast loading. *Geotechnical and Geological Engineering*, *35*, 1491–1512.

101. Vannucci, P., Masi, F., & Stefanou, I. (2017). *A comparative study on the effects of blast actions on a monumental structure*.

102. Liu, H. (2009). Dynamic Analysis of Subway Structures Under Blast Loading. *Geotechnical and Geological Engineering*, *27*(6), 699–711. https://doi.org/10.1007/s10706-009-9269-9

103. Liu, H. (2012). Soil-structure interaction and failure of cast-iron subway tunnels subjected to medium internal blast loading. *Journal of performance of constructed facilities*, *26*(5), 691–701.

104. Ning, P. F., & Tang, D. G. (2011). Analysis of the dynamic response of underground structures under internal explosion. In *Advanced Materials Research* (Vol. 255, pp. 1681–1686). Trans Tech Publ.

105. Buonsanti, M., & Leonardi, G. (2013). 3-D simulation of tunnel structures under blast loading. *Archives of civil and mechanical engineering*, *13*(1), 128–134.

106. Verma, A. K., Jha, M. K., Mantrala, S., & Sitharam, T. G. (2017). Numerical simulation of explosion in twin tunnel system. *Geotechnical and Geological Engineering*, *35*, 1953–1966.

107. Prasanna, R., & Boominathan, A. (2020). Finite-element studies on factors influencing the response of underground tunnels subjected to internal explosion. *International Journal of Geomechanics*, *20*(7), 04020089.

108. Guruprasad, S., & Mukherjee, A. (2000). Layered sacrificial claddings under blast loading Part II—experimental studies. *International Journal of Impact Engineering*, *24*(9), 975–984.

109. Hanssen, A. G., Enstock, L., & Langseth, M. (2002). Close-range blast loading of aluminium foam panels. *International journal of impact engineering*, *27*(6), 593–618.

110. Mandal, J., Goel, M. D., & Agarwal, A. K. (2022). Study of Different Materials to Mitigate Blast Energy for the Tunnel Subjected to Buried Explosion. In *Composite Materials for Extreme Loading: Proceedings of the Indo-Korean workshop on Multi Functional Materials for Extreme Loading 2021* (pp. 505–518). Springer.

111. Ma, G. W., & Ye, Z. Q. (2007). Energy absorption of double-layer foam cladding for blast alleviation. *International Journal of Impact Engineering*, *34*(2), 329–347.

112. Theobald, M. D., & Nurick, G. N. (2010). Experimental and numerical analysis of tube-core claddings under blast loads. *International Journal of Impact Engineering*, *37*(3), 333–348.

113. Zhao, H., Yu, H., Yuan, Y., & Zhu, H. (2015). Blast mitigation effect of the foamed cement-base sacrificial cladding for tunnel structures. *Construction and Building Materials*, *94*, 710–718.

114. Tarlochan, F., Ramesh, S., & Harpreet, S. (2012). Advanced composite sandwich structure design for energy absorption applications: Blast protection and crashworthiness. *Composites Part B: Engineering*, *43*(5), 2198–2208.

115. Patnaik, G., Kaushik, A., Rajput, A., Prakash, G., & Velmurugan, R. (2021). Ballistic performance of quasi-isotropic CFRP laminates under low velocity impact. *Journal of Composite Materials*, *55*(24), 3511–3527.

116. Pham, T. M., & Hao, H. (2016). Review of concrete structures strengthened with FRP against impact loading. In *Structures* (Vol. 7, pp. 59–70). Elsevier.

117. Lin, X., & Zhang, Y. X. (2016). Nonlinear finite element analysis of FRP-strengthened reinforced concrete panels under blast loads. *International Journal of Computational Methods*, *13*(04), 1641002.

118. Asteris, P., Ashrafian, A., & Rezaie-Balf, M. (2019). Prediction of the Compressive Strength of Self-Compacting Concrete using Surrogate Models. *Computers and Concrete*, *24*, 137–150. https://doi.org/10.12989/cac.2019.24.2.137

119. Nguyen, H., & Bui, X.-N. (2019). Predicting blast-induced air overpressure: a robust artificial intelligence system based on artificial neural networks and random forest. *Natural Resources Research*, *28*(3), 893–907.

120. Tantele, E., Votsis, R., & Onoufriou, T. (2015). Integration of probabilistic effectiveness with a two-stage genetic algorithm methodology to develop optimum maintenance strategies for bridges. *The Open Construction & Building Technology Journal*.

121. Bai, X.-D., Cheng, W.-C., Sheil, B. B., & Li, G. (2021). Pipejacking clogging detection in soft alluvial deposits using machine learning algorithms. *Tunnelling and Underground Space Technology*, *113*, 103908.

122. Öztaş, A., Pala, M., Özbay, E., Kanca, E., Çagˇlar, N., & Bhatti, M. A. (2006). Predicting the compressive strength and slump of high strength concrete using neural network. *Construction and building materials*, *20*(9), 769–775.

123. Mansour, M. Y., Dicleli, M., Lee, J.-Y., & Zhang, J. (2004). Predicting the shear strength of reinforced concrete beams using artificial neural networks. *Engineering Structures*, *26*(6), 781–799.

124. Slater, E., Moni, M., & Alam, M. S. (2012). Predicting the shear strength of steel fiber reinforced concrete beams. *Construction and Building Materials*, *26*(1), 423–436.

125. Mishra, M., Agarwal, A., & Maity, D. (2019). Neural-network-based approach to predict the deflection of plain, steel-reinforced,

and bamboo-reinforced concrete beams from experimental data. *SN Applied Sciences*, *1*, 1–11.

126. Pham, T. M., & Hao, H. (2016). Prediction of the impact force on reinforced concrete beams from a drop weight. *Advances in Structural Engineering*, *19*(11), 1710–1722.

127. Dung, C. V. (2019). Autonomous concrete crack detection using deep fully convolutional neural network. *Automation in Construction*, *99*, 52–58.

128. Shishegaran, A., Khalili, M. R., Karami, B., Rabczuk, T., & Shishegaran, A. (2020). Computational predictions for estimating the maximum deflection of reinforced concrete panels subjected to the blast load. *International Journal of Impact Engineering*, *139*, 103527.

129. Almustafa, M. K., & Nehdi, M. L. (2020). Machine learning model for predicting structural response of RC slabs exposed to blast loading. *Engineering structures*, *221*, 111109.

130. Anitescu, C., Atroshchenko, E., Alajlan, N., & Rabczuk, T. (2019). Artificial neural network methods for the solution of second order boundary value problems. *Computers, Materials and Continua*, *59*(1), 345–359.

131. Samaniego, E., Anitescu, C., Goswami, S., Nguyen-Thanh, V. M., Guo, H., Hamdia, K., … Rabczuk, T. (2020). An energy approach to the solution of partial differential equations in computational mechanics via machine learning: Concepts, implementation and applications. *Computer Methods in Applied Mechanics and Engineering*, *362*, 112790.

132. Belytschko, T., Liu, W. K., Moran, B., & Elkhodary, K. (2014). *Nonlinear finite elements for continua and structures*. John wiley & sons.

133. Li, X.-X. L. (2020). Parametric study on numerical simulation of missile punching test using concrete damaged plasticity (CDP) model. *International Journal of Impact Engineering*, *144*, 103652.

134. Lubliner, J., Oliver, J., Oller, S., & Oñate, E. (1989). A plastic-damage model for concrete. *International Journal of solids and structures*, *25*(3), 299–326.

135. Lee, J., & Fenves, G. L. (1998). Plastic-damage model for cyclic loading of concrete structures. *Journal of engineering mechanics*, *124*(8), 892–900.

136. Taerwe, L., & Matthys, S. (2013). Fib model code for concrete structures 2010. Ernst & Sohn, Wiley.

137. Wei, J., Quintero, R., Galati, N., & Nanni, A. (2007). Failure modeling of bridge components subjected to blast loading part I: strain rate-dependent damage model for concrete. *International Journal of Concrete Structures and Materials*, *1*(1), 19–28.

138. Peng, Y., Wang, Q., Ying, L., Kamel, M. M. A., & Peng, H. (2019). Numerical simulation of dynamic mechanical properties of concrete under uniaxial compression. *Materials*, *12*(4), 643.

139. Hashin, Z., & Rotem, A. (1973). A fatigue failure criterion for fiber reinforced materials. *Journal of composite materials*, *7*(4), 448–464.

140. Hashin, Z. (1981). Fatigue failure criteria for unidirectional fiber composites.

141. TM5-855-1. (1998). Design and analysis of hardened structures to conventional weapons effects.

142. Karlos, V., & Solomos, G. (2013). Calculation of blast loads for application to structural components. *Luxembourg: Publications Office of the European Union*, 5.

143. Jasmine, P. H., & Arun, S. (2021). Machine learning applications in structural engineering-a review. In *IOP Conference Series: Materials Science and Engineering* (Vol. 1114, p. 012012). IOP Publishing.

144. Allam, Z. (2019). Achieving neuroplasticity in artificial neural networks through smart cities. *Smart Cities*, *2*(2), 118–134.

145. Svetnik, V., Liaw, A., Tong, C., Culberson, J. C., Sheridan, R. P., & Feuston, B. P. (2003). Random forest: a classification and regression tool for compound classification and QSAR modeling. *Journal of chemical information and computer sciences*, *43*(6), 1947–1958.

146. Bai, C., Nguyen, H., Asteris, P. G., Nguyen-Thoi, T., & Zhou, J. (2020). A refreshing view of soft computing models for predicting the deflection of reinforced concrete beams. *Applied Soft Computing*, *97*, 106831.

147. Chai, T., & Draxler, R. R. (2014). Root mean square error (RMSE) or mean absolute error (MAE)?–Arguments against avoiding RMSE in the literature. *Geoscientific model development*, *7*(3), 1247–1250.

148. Yu, X., Xiao, Y., & Li, B. (2020). Evaluation of failure probability for RC slabs subjected to low-velocity impacts. *Magazine of Concrete Research*, *72*(1), 27–42.

149. Iqbal, M. A., Rajput, A., & Gupta, N. K. (2017). Performance of prestressed concrete targets against projectile impact. *International Journal of Impact Engineering*, *110*, 15–25. https://doi.org/https://doi.org/10.1016/j.ijimpeng.2016.11.015

150. Batayneh, M. K., Marie, I., & Asi, I. (2008). Promoting the use of crumb rubber concrete in developing countries. *Waste management*, *28*(11), 2171–2176.

151. Gündüz, Y., Taşkan, E., & Şahin, Y. (2016). Using hooked-end fibres on high performance steel fibre reinforced concrete. *High Perform. Optim. Des. Struct. Mater. II*, *1*, 265–276.

152. Oucif, C., Kalyana Rama, J. S., Shankar Ram, K., & Abed, F. (2021). Damage modeling of ballistic penetration and impact behavior of concrete panel under low and high velocities. *Defence Technology*, *17*(1), 202–211. https://doi.org/https://doi.org/10.1016/j.dt.2020.03.013

153. Kota, S. K., Rama, J. S. K., & Murthy, A. R. (2019). Strengthening RC frames subjected to lateral load with Ultra High-Performance fiber reinforced concrete using damage plasticity model. *Earthquakes and Structures*, *17*(2), 221.

154. Memon, D., Matthys, S., & Lecompte, D. (2020). Numerical analysis of small-scale concrete beams strengthened with cfrp under impact loading. In *Fib Symposium 2020* (Vol. 51, pp. 915–921). fib.

155. Yılmaz, M. C., Anıl, Ö., Alyavuz, B., & Kantar, E. (2014). Load displacement behavior of concrete beam under monotonic static and low velocity impact load. *International Journal of Civil Engineering*, *12*(4), 488–503.

156. Bäker, M. (2018). How to get meaningful and correct results from your finite element model. *arXiv preprint arXiv:1811.05753*.

157. Wriggers, P., & Laursen, T. A. (2006). *Computational contact mechanics* (Vol. 2). Springer.

158. Jankowiak, T., & Lodygowski, T. (2005). Identification of parameters of concrete damage plasticity constitutive model. *Foundations of civil and environmental engineering*, *6*(1), 53–69.

159. Ulfkjaer, J. P. (1995). Fracture Energy of Normal Strength Concrete, High Strength Concrete and Ultra High Strength Ultra

Ductile Fibre Reinforced Concrete. *Proceedings FRAMCOS-2*, 31–44.

160. Hillerborg, A. (1985). The theoretical basis of a method to determine the fracture energy GF of concrete. *Materials and structures*, *18*, 291–296.

161. Session, C. euro-international du beton. P. (1988). *CEB-FIP Model Code 1990: Supplementary Documents for the First Predraft 1988*. Comite euro-international du beton.

162. Rey-de-Pedraza, V., Gálvez, F., & Franco, D. C. (2018). Measurement of fracture energy of concrete at high strain rates. In *EPJ web of conferences* (Vol. 183, p. 02065). EDP Sciences.

163. Othman, H. (2016). Performance of ultra-high performance fibre reinforced concrete plates under impact loads. *Ryerson University, Toronto*.

164. 10262-2009, I. (1990). Concrete Mix Proportioning–Guidelines (First revision). Bureau of Indian Standards New Delhi.

165. NADIRSHAH, S. E. A. (1959). METHODS OF SAMPLING AND ANALYSIS OF CONCRETE.

166. Ahmad, S. H., Arockiasamy, M., Balaguru, P. N., Ball, C. G., Ball Jr, H. P., Batson, G. B., … Freedman, S. (1988). Measurement of properties of fiber reinforced concrete. *American Concrete Institute: Farmington Hills, MI, USA*.

167. Genikomsou, A. (2016). Nonlinear finite element analysis of punching shear of reinforced concrete slab-column connections.

168. Topcu, I. B. (1995). The properties of rubberized concretes. *Cement and concrete research*, *25*(2), 304–310.

169. 8112, I. S. (1989). Specification for 43 grade ordinary Portland cement. Bureau of Indian Standard New Delhi, India.

170. 1), I. S. 516 (Part 1/Sec. (2021). Methods of tests for strength of concrete. Bureau of Indian Standards New Delhi, India.

171. RAJ, A., Usman, A. P. J., Nagarajan, P., & Shashikala, A. P. (2019). Fracture behaviour of fibre reinforced rubcrete. In *Materials Science Forum* (Vol. 969, pp. 80–85). Trans Tech Publ.

172. Raj, A., Usman Arshad, P. J., Nagarajan, P., & Shashikala, A. P. (2020). Experimental investigation on the fracture behaviour of polypropylene fibre-reinforced rubcrete. In *Structural Integrity Assessment: Proceedings of ICONS 2018* (pp. 335–345). Springer.

173. Kaushik, A., Patnaik, G., Rajput, A., & Prakash, G. (2022). Nonlinear behaviour of concrete under low-velocity impact by using a damaged plasticity model. *Iranian Journal of Science and Technology, Transactions of Civil Engineering*, *46*(5), 3655–3677.

174. Hu, S., Tang, H., & Han, S. (2021). Energy absorption characteristics of PVC coarse aggregate concrete under impact load. *International Journal of Concrete Structures and Materials*, *15*(1), 1–16.

175. Rajput, A., & Pavlovic, A. (2017). Response of Initially Stressed Concrete Targets Under High Rate of Loading, 517–523. https://doi.org/10.5937/fmet1704517R

176. Rajput, A., & Iqbal, M. A. (2018). Prestressed concrete targets under high rate of loading. https://doi.org/10.1177/2041419618763933

177. Rajput, A., & Iqbal, M. A. (2017). Experimental and numerical study of concrete targets under high rate of loading. *Procedia Engineering*, *173*, 130–137. https://doi.org/10.1016/j.proeng.2016.12.049

178. Mourão, R. F. F. (2020). Blast loading effects on externally strengthened concrete structures.

179. Malvar, L. J., & Crawford, J. E. (1998). *Dynamic increase factors for concrete*. Naval Facilities Engineering Service Center Port hueneme CA.

180. Zhao, C. F., & Chen, J. Y. (2013). Damage mechanism and mode of square reinforced concrete slab subjected to blast loading. *Theoretical and Applied Fracture Mechanics*, *63*, 54–62.

181. Li, J., & Hao, H. (2014). Numerical study of concrete spall damage to blast loads. *International journal of impact engineering*, *68*, 41–55.

182. Bischoff, P. H., & Perry, S. H. (1991). Compressive behaviour of concrete at high strain rates. *Materials and structures*, *24*, 425–450.

183. Army, U. States. D. of the. (1991). *Structures to resist the effects of accidental explosions* (Vol. 88). Departments of the Army, Navy, and Air Force.

184. Goel, M. D., Matsagar, V. A., Gupta, A. K., & Marburg, S. (2012). An abridged review of blast wave parameters. *Defence Science Journal*, *62*(5), 300–306.

185. Amli, A., Sabah, A., Al-Ansari, N., & Laue, J. (2019). Study numerical simulation of stress-strain behavior of reinforced concrete bar in soil using theoretical models. *Civil Engineering Journal*, *11*(5), 2349–2358.

186. Bhatnagar, N., Nayak, D., Singh, I., Chouhan, H., & Mahajan, P. (2004). Determination of machining-induced damage characteristics of fiber reinforced plastic composite laminates. *Materials and Manufacturing Processes*, *19*(6), 1009–1023.

187. Gargano, A., Das, R., & Mouritz, A. P. (2019). Finite element modelling of the explosive blast response of carbon fibre-polymer laminates. *Composites Part B: Engineering*, *177*, 107412.

188. Rotem, A., & Lifshitz, J. M. (1971). Longitudinal strength of unidirectional fibrous composite under high rate of loading. In *Proc. 26th Annual Tech. Conf. Soc. Plastics Industry Reinforced Plastics, Composites Division, Washington, DC, Section* (Vol. 10, pp. 1–10).

189. Harding, J., & Welsh, L. M. (1983). A tensile testing technique for fibre-reinforced composites at impact rates of strain. *Journal of materials science*, *18*, 1810–1826.

190. Tsai, J. L., & Kuo, J. C. (2006). Investigating strain rate effect on transverse compressive strength of fiber composites. In *Key Engineering Materials* (Vol. 306, pp. 733–738). Trans Tech Publ.

191. Shokrieh, M. M., & Omidi, M. J. (2009). Investigation of strain rate effects on in-plane shear properties of glass/epoxy composites. *Composite Structures*, *91*(1), 95–102.

192. Tanapornraweekit, G., Haritos, N., & Mendis, P. (2011). Behavior of FRP-RC slabs under multiple independent air blasts. *Journal of Performance of Constructed Facilities*, *25*(5), 433–440.

193. Harzallah, S., Chabaat, M., Saidani, M., & Moussaoui, M. (2022). Numerical investigation of the seismic vulnerability of bridge piers strengthened with steel fibre reinforced concrete (SFRC) and carbon fibre composites (CFC). *Case Studies in Construction Materials*, *17*, e01235.

194. Bjälke, V. (2018). Structural mechanics and resistance of concrete structures in the event of a hydrogen explosion in nuclear powerplants.

195. Dudziak, S., Jackiewicz-Rek, W., & Kozyra, Z. (2021). On the calibration of a numerical model for concrete-to-concrete interface. *Materials*, *14*(23), 7204.

196. Zaid, M., & Sadique, M. R. (2021). The response of rock tunnel when subjected to blast loading: Finite element analysis. *Engineering Reports*, *3*(2), e12293.

197. Priddy, K. L., & Keller, P. E. (2005). *Artificial neural networks: an introduction* (Vol. 68). SPIE press.

198. Levenberg, K. (1944). A method for the solution of certain non-linear problems in least squares. *Quarterly of applied mathematics*, *2*(2), 164–168.

199. Nguyen, H., & Bui, X.-N. (2020). Soft computing models for predicting blast-induced air over-pressure: A novel artificial intelligence approach. *Applied Soft Computing*, *92*, 106292.

200. Dennis, A. A., Pannell, J. J., Smyl, D. J., & Rigby, S. E. (2021). Prediction of blast loading in an internal environment using artificial neural networks. *International Journal of Protective Structures*, *12*(3), 287–314.

APPENDIX

1. The DIF formulations for concrete at higher strain rates are shown in this Appendix. In Table A.1, f_{cd} and E_{cd} are the compressive strength and compressive modulus of elasticity at

strain rate $\dot{\varepsilon_c}$, f_c and E_c are the compressive strength and compressive modulus of elasticity at reference strain rate $(30 \times 10^{-6}\ s^{-1})$, f_{td} and E_{td} are the tensile strength and tensile modulus of elasticity at strain rate $\dot{\varepsilon_t}$, f_t and E_t are the tensile strength and tensile modulus of elasticity at reference strain rate $(1 \times 10^{-6}\ s^{-1})$.

Table A.1 DIF formulations for concrete [123]

Parameter	Formula	Strain rate range	Eqn.
Compressive strength	$\mathrm{DIF}_{fc} = \dfrac{f_{cd}}{f_c} = \begin{cases} \left(\dfrac{\dot{\varepsilon}_c}{30 \times 10^{-6}}\right)^{0.014} \\ 0.012\left(\dfrac{\dot{\varepsilon}_c}{30 \times 10^{-6}}\right)^{1/3} \end{cases}$	$\dot{\varepsilon}_c \leq 30\ s^{-1}$ $30 < \dot{\varepsilon}_c \leq 300\ s^{-1}$	(2.17)
Modulus of elasticity in compression	$\mathrm{DIF}_{Ec} = \dfrac{E_{cd}}{E_c} = \left(\dfrac{\dot{\varepsilon}_c}{30 \times 10^{-6}}\right)^{0.026}$	$30 \times 10^{-6} \leq \dot{\varepsilon}_c \leq 300\ s^{-1}$	(2.18)
Strain at peak compressive strength	$\mathrm{DIF}_{\varepsilon c} = \left(\dfrac{\dot{\varepsilon}_c}{30 \times 10^{-6}}\right)^{0.02}$	$30 \times 10^{-6} \leq \dot{\varepsilon}_c \leq 300\ s^{-1}$	(2.19)

Tensile strength	$\mathrm{DIF}_{ft} = \frac{f_{td}}{f_t} = \begin{cases} \left(\frac{\dot{\varepsilon}_t}{1 \times 10^{-6}}\right)^{0.018} \\ 0.062\left(\frac{\dot{\varepsilon}_c}{1 \times 10^{-6}}\right)^{1/3} \end{cases}$	$\dot{\varepsilon}_t \leq 10\ s^{-1}$ $10 < \dot{\varepsilon}_t \leq 300\ s^{-1}$	(2.20)
Modulus of elasticity in tension	$\mathrm{DIF}_{Et} = \frac{E_{td}}{E_t} = \left(\frac{\dot{\varepsilon}_t}{1 \times 10^{-6}}\right)^{0.026}$	$1 \times 10^{-6} \leq \dot{\varepsilon}_t \leq 300\ s^{-1}$	(2.21)
Strain at peak tensile strength	$\mathrm{DIF}_{\varepsilon t} = \left(\frac{\dot{\varepsilon}_t}{1 \times 10^{-6}}\right)^{0.02}$	$1 \times 10^{-6} \leq \dot{\varepsilon}_t \leq 300\ s^{-1}$	(2.22)